

Synthesis and Application of Crystalline Calcium Silicate Hydrate Phases

A Dissertation

Presented to

the faculty of the School of Engineering and Applied Science

University of Virginia

in partial fulfillment
of the requirements for the degree

Doctor of Philosophy

by

Dan A Plattenberger

August 2019

APPROVAL SHEET

This Dissertation
is submitted in partial fulfillment of the requirements
for the degree of
Doctor of Philosophy

Author Signature: *Dan Plattenberger*

This Dissertation has been read and approved by the examining committee:

Advisor: Andres Clarens

Committee Member: Lisa Colosi Peterson

Committee Member: Jose Gomez

Committee Member: Elizabeth Opila

Committee Member: Catherine Peters

Committee Member: _____

Accepted for the School of Engineering and Applied Science:



Craig H. Benson, School of Engineering and Applied Science

August 2019

to mom and dad

Abstract

Silicate weathering is important in many natural and engineered contexts including in the performance of cement. Cement is the most common man-made material in the world and is responsible for over 5% of annual CO₂ emissions. Here, the reaction of a model calcium silicate, pseudowollastonite (CaSiO₃) with aqueous solutions containing CO₂ was evaluated in depth to understand how this class of reactions might be deployed in two contexts. The first application is subsurface engineering activity where permeability control is desirable for sustainable deployment of geologic carbon storage, geothermal energy, or energy storage. The second application is in the synthesis of pre-cast concrete that is low carbon and high performance.

The reaction of CaSiO₃ with CO_{2(aq)} nominally produces calcium carbonate (CaCO₃) and amorphous silica (SiO₂) but here, experiments suggest that the crystal structure of the parent silicate and the solution pH determine the way in which the silicate reacts with CO₂ and the resulting structures of the reaction products. Batch experiments were carried out using two polymorphs of CaSiO₃, wollastonite (chain-structured) and pseudowollastonite (ring-structured), at elevated temperatures and CO_{2(aq)} concentrations. Reaction of CO_{2(aq)} with wollastonite produced CaCO₃ and SiO₂, whereas reaction of CO_{2(aq)} with pseudowollastonite produced numerous plate-like crystalline calcium silicate hydrate (CCSH) phases, along with CaCO₃ and SiO₂. Analyses of the resulting CCSH phases suggest that they are similar to those responsible for providing the strength and durability of Roman cements in terms of morphology and composition.

The first application of CCSH-based cement is presented in the context of controlling fluid transport in the subsurface, which is relevant to geologic carbon sequestration, oil and gas well closure, and enhanced geothermal energy production. The CCSH phases, in porous media, were compared to calcium carbonate precipitates, which are typically thought to form in the naturally

carbon-rich environments in the subsurface. A suite of analytical methods including electron microscopy, synchrotron-based X-ray diffraction and fluorescence, and permeability measurements, among others, show that the CCSH phases, which formed in the presence of dissolved $\text{CO}_{2(\text{aq})}$ and NaOH at pH 6.65, decreased permeability in sand columns by 2.83 orders of magnitude in 495 hours of reaction. Under the same conditions with no NaOH (pH 3.94), calcium carbonate was the predominant precipitate and led to a decrease in permeability of only 1.16 orders of magnitude. Acetic acid injected into the columns revealed that the CCSH phases were more resistant to dissolution at low pH than calcium carbonate, which could result in longer-lasting seals for undesirable fluid migration in the subsurface.

The second application addresses CCSH performance in the context of precast cement and compares characteristics of strength, durability, resistance to acid-dissolution, and environmental impact to those of Portland and carbonate-based cements. Precast mortar specimens were prepared via a novel curing technique that involved first allowing the specimens to harden in a CO_2 atmosphere and then submerging them in a heated carbonate-rich solution buffered with NaOH in order for CCSH phases to precipitate. A Taguchi design of experiments was implemented to optimize the curing conditions, which yielded mortar with comparable strength as the alternatives (13.9 MPa at 7 days of curing), while possessing lower diffusivity to dissolved ions, and more resistance to acid-attack. Relative to Portland cement, a lifecycle analysis shows that CCSH cement could be produced with 85% lower CO_2 emissions.

Acknowledgements

It's been a long five years for me in Charlottesville. At the same time, it's gone by in the blink of an eye. All the late nights and early mornings in the lab, the deadlines and papers and proposals, the wine festivals, tubing adventures, and trips around the world. All those experiences mean nothing without friends to share them with. To Riley and Thankful (and Ez), Stuart and Mait, Buddy, Andrei, Bo, and Tao, thank you all for making Charlottesville my home and a place I'll always remember.

To my committee, thank you all for your words of wisdom and encouragement. I've long known that my dream is to become a professor and getting to know and work with each of you has solidified the reason why. What a privilege it has been to collaborate with such talented and accomplished individuals who I admire so much. Thank you, Lisa, Jose, Beth, and Catherine. And to Lindsay Ivey Burden, I thank you for bringing me to UVa.

Andres, believe it or not, the most important thing I've learned in your lab isn't that pseudowollastonite can react with CO₂ in unexpected ways. It's that thinking big, telling your story, and connecting with people is how we make progress. You are incredible at developing people, being cautiously optimistic, and always – in your words – moving the needle and I feel so privileged to have learned so much from you. Thank you for always laughing with me, staying patient, and for giving me an opportunity. I look forward to the big projects we can tackle together in the future.

To Catherine McCloskey and Tonya Harrelson: it's safe to say that neither of you know the impact you've had on my life. Both of you, at different times, saw something in me that no one else did. It's upsetting that teachers do not get the recognition or praise that they deserve but, then again, they don't become teachers for recognition or praise. They become teachers to inspire generations to aim high and meet their potential. Both of you saw my potential and I hope that this document serves as a small testament to your power and influence.

To Gina: You know how I always say I'm the unluckiest person on the planet? Well it's getting harder and harder to say that with a straight face. I can't imagine making it through all of this without you and I just can't believe how lucky I am to marry you. As I'm writing this, we have no idea where we're about to end up. But, for me – at the risk of sounding like a hand-painted sign on Etsy – home will be wherever I'm with you. And I can't wait for that.

Mom and dad. I don't mean to give you the shortest acknowledgement, it's just that I have no words. What do you say to two people that have given you everything and asked for nothing? I could never repay you for the sacrifices you've made for me but I hope that I continue to make you proud and know that whatever I go on to accomplish is because of you.

Table of Contents

Chapter 1. Overview	1
1.1. Motivation and Objectives.....	1
1.2. Background.....	5
1.2.1. Ordinary Portland Cement	5
1.2.2. Environmentally Preferable Cement Materials.....	7
1.2.3. Carbonation of Conventional Cements.....	7
1.2.4. Carbonation of Mineral Silicates.....	8
1.2.5. Roman Cement.....	8
Chapter 2. Calcium Silicate Crystal Structure Impacts Reactivity with CO ₂ and Precipitate Chemistry	10
2.1. Chapter Summary.....	10
2.2. Introduction.....	11
2.3. Materials and Methods	13
2.3.1. Materials	13
2.3.2. Batch Experiments.....	14
2.3.3. Analytical Methods.....	14
2.4. Results and Discussion	15
2.4.1. Layered Calcium Silicate Formation.....	15
2.4.2. Mechanism for Layered Calcium Silicate Formation.....	17
2.5. Chapter 2 Acknowledgements	21
Chapter 3. Targeted Permeability Control in the Subsurface Via Calcium Silicate Carbonation.....	22
3.1. Chapter Summary.....	22
3.2. Introduction.....	23
3.3. Experimental Materials and Methods.....	26
3.3.1. Sand Column Experiments.....	26
3.3.2. Powder Batch Experiments.....	29
3.3.3. Air Permeability Measurements.....	30
3.3.4. Materials Characterization	30
3.4. Results	32
3.4.1. Precipitates and their Impact on Sand Column Permeability	32
3.4.2. μ XRF Mapping of Precipitation and Diffusivity	33
3.4.3. Precipitation Locations Within Pores	35
3.4.4. Temporal Evolution of Reaction Fronts	37
3.4.5. Effects of Ion Concentrations on Precipitation Products and Permeability.....	38
3.4.6. Stability of Reacted Columns Under Acidic Conditions.....	39
3.4.7. Effects of Temperature on CESH Precipitation.....	40
3.4.8. Effect of Time on CESH Composition.....	41
3.5. Environmental Implications.....	42
3.6. Chapter 3 Acknowledgements	44
Chapter 4. Formation of Low-Carbon Crystalline Cement via Calcium Silicate Carbonation.....	45
4.1. Chapter Summary.....	45
4.2. Introduction.....	46
4.3. Results	49
4.3.1. Compressive Strength and Carbon Utilization of Various Cement Types.....	49

4.3.2. Comparisons of Durability.....	52
4.3.3. Lifecycle Analysis of CCSH Cement.....	55
4.4. Discussion.....	57
4.5. Methods.....	58
4.5.1. Pseudowollastonite Synthesis.....	58
4.5.2. Mortar Cube Design of Experiments.....	58
4.5.3. Carbon Uptake.....	59
4.5.4 Diffusion Mapping.....	59
4.5.5. Acid Dissolution Tests.....	60
4.5.6. Lifecycle Analysis.....	61
Chapter 5. Conclusions and Future Work.....	64
5.1. Conclusions.....	64
5.2. Future Work.....	66
References.....	69
Appendix I: Supporting Information for Chapter 3 - Targeted Permeability Control in the Subsurface Via Calcium Silicate Carbonation.....	A1.1
Appendix II: Supporting Information for Chapter 4 - Formation of Low-Carbon Crystalline Cement via Calcium Silicate Carbonation.....	A2.1

List of Figures and Tables

Figure 1.1. China’s 2.4 billion tonnes of cement produced in 2018 was more than the rest of the world’s production, combined. Figure: Niall McCarthy, Forbes, USGS.....	2
Figure 1.2. (a) Crystalline calcium silicate hydrate phases found in ancient Roman cement are distinctly different from (b) amorphous calcium silicate hydrate gels that typically form in cured ordinary Portland cement and exhibit a similar composition and morphology to (c) calcium silicate hydrate phases found in this work.....	3
Figure 1.3. The Pantheon, completed ca. 126 AD demonstrates the longevity and resilience of Roman cement. Photo: Jean-Christophe Benoit, Wikimedia Commons.....	9
Figure 2.0. Experimental data in this chapter shows that the reaction of wollastonite with $\text{CO}_{2(\text{aq})}$ produces CaCO_3 and amorphous SiO_2 while the reaction involving its polymorph, pseudowollastonite, has the potential to produce crystalline calcium silicate hydrate phases in addition to CaCO_3 and amorphous phases.....	11
Table 2.1. Selection of experimental conditions and reaction products described in this work. Products listed in accordance to prevalence, as determined by SEM/EDS analysis coupled with XRD. Here, “irregular” phases (IR) include amorphous silica as well as unreacted CaSiO_3 , solid carbonates include Calcite (Cal) and Aragonite (Ara) and layered calcium silicate phases (plate-like (PL)) are also observed.....	16
Figure 2.1. Representative SEM micrographs (a-d) of the phases produced in these experiments, including calcite (Cal), aragonite (Ara), and irregular silica phases (Ir). At elevated pH and moderate dissolved carbonate concentrations, appreciable quantities of plate-like (PL) calcium silicates are produced (c,d). EDS spectra (e) are presented for each of the identified phases in (a-d). The spectra show that the PL phases are rich in both calcium and silica. TEM micrographs (f,g) show the nature of the PL phases and EDS confirms an abundance of Si and Ca.	17
Figure 2.2. A proposed mechanism for how the crystal structures of wollastonite (a) and pseudowollastonite (b), both polymorphs of CaSiO_3 , influence the reactions that proceed in the presence of $\text{CO}_{2(\text{aq})}$. Wollastonite dissolves non-stoichiometrically, as evidenced by ICP-OES measurements of dissolved Si and Ca. The resulting leached layer of SiO_x is depicted, as is the reaction of calcium with dissolved carbonate to generate CaCO_3 . Pseudowollastonite dissolves congruently. The elevated concentration of dissolved silica promotes precipitation of layered calcium silicates. In parallel, CaCO_3 may precipitate, consuming dissolved carbonate and some calcium ions.	19
Figure 2.3. SEM micrographs and EDS analyses of unreacted pseudowollastonite (a) showed no evidence of CaCO_3 while those from reacted pseudowollastonite (b) showed a significant quantity. After acid washing, CaCO_3 was not observed while plate-like phases remained, unaltered (c).	20
Figure 3.0. This chapter investigates the efficacy of (left) carbonate precipitates and (right) crystalline calcium silicate hydrate phases to limit flow in porous media. SEM micrographs of the morphology of both types of precipitates is shown alongside synchrotron X-ray fluorescence maps of the inlet of pseudowollastonite-containing sand columns that were reacted in the presence of CO_2 under conditions representative of the subsurface.....	23
Figure 3.1. Sand columns were injected with a water-pseudowollastonite suspension and then submerged, upright, in a Teflon-lined, stainless-steel pressure vessel. CO_2 was injected into the headspace of the vessel with a syringe pump, where it equilibrated with the batch solution. CO_2 and other dissolved species could diffuse through the top (inlet) of the columns and react with the CaSiO_3	27
Table 3.1. Experimental Conditions for Column Experiments.	28
Figure 3.2. (a) Representative calcium carbonate and amorphous silica morphologies, which result from aqueous pseudowollastonite carbonation with unmodified pH (no NaOH added) at 1.1 MPa P_{CO_2} . (b,c) An example of CCSH morphology from an epoxied and sectioned column, resulting from aqueous pseudowollastonite carbonation with elevated pH (0.1 M NaOH). Sheet-like morphology was the only one observed for CCSHs in the columns.....	31
Figure 3.3. The log reduction of permeability for columns reacted in (blue) CO_2 only and (orange) $\text{CO}_2 + \text{NaOH}$ as a function of reaction time.	32
Figure 3.4. Micro-XRF maps of (green) Sr and (blue) Br for the inlet 8 mm of columns reacted for 495 hr in (a,b) CO_2 only and (c,d) $\text{CO}_2 + \text{NaOH}$ compared to (e,f) an unreacted column. Dissolved Sr was present during the	

reaction period and appeared to coprecipitate with Ca in Ca-carbonate. Columns were submerged, upright, in a Br solution after the reaction period to visualize diffusivity of the columns, as a complement to permeability measurements. Each Sr map shares a common color scale. Likewise, each Br map shares a common color scale. The intensities shown in these maps are proportional to element concentrations.34

Figure 3.5. (a) SEM micrograph of a representative pore in a CO₂ column, where Ca-carbonate and amorphous silica precipitated throughout the pore body indiscriminately. (b) Compared to SEM cross-section of a representative pore in CO₂ + NaOH columns, showing a relatively open pore body but dense CCSH precipitation along sand grain edges and in the pore throats. (c,d) Inset EDS maps show that CCSHs in this pore appear to contain both calcium and silicon.36

Figure 3.6. (a) Br and (b) Sr μXRF maps of 96 hr CO₂ column experiments show a uniform carbonation front normal to the direction of diffusion. In contrast, at 495 hr of reaction, the (c) Br and (d) Sr μXRF maps show a reaction front that is non-uniform and indicates redissolution of solid carbonates near the inlet of the column.....37

Figure 3.7. Permeabilities of (blue) CO₂ only columns and (orange) CO₂ + NaOH columns prior to CaSiO₃ injection, after injection, after the 72 hr reaction period, and after 16 hr acid diffusion at (top) pH 4 and (center) pH 6, and with only DI water diffusion (bottom)40

Figure 3.8. Silicon to Ca ratios of CCSH phases from powder batch experiments reacted in 0.1 M NaOH + 0.19 M CO₂ for 24, 72, and 168 hr. The ratio for unreacted pseudowollastonite is also shown at 0 hr. The Si:Ca ratios vary widely at all time periods and do not clearly seem to approach any particular ratio.42

Figure 4.1. The global economy includes some sectors that are ready to decarbonize and some that are more challenging to decarbonize. Of those more recalcitrant sectors, cement production is particularly challenging both because its use is accelerating worldwide and low-carbon alternatives have yet to be proposed.....47

Figure 4.2. Macro- and micro-scale differences between (a) ordinary Portland cement mortar, (b) CCSH cement mortar, and (c) carbonate cement mortar. (d) The compressive strength of 28-day OPC formulations (based on ASTM C270) are shown relative to 7-day compressive strengths of the alternative cements, along with 7-day CO₂ uptake measurements50

Figure 4.3. Diffusion of a Br tracer into (a) a 7-day OPC mortar specimen and (b) a 3-day CCSH cement mortar specimen. The top of both maps align with the outer edge of the specimens and color map is shared, allowing a comparison of relative Br concentrations.53

Figure 4.4. Mortar cubes made with (a) ordinary Portland cement, (b) carbonate-based cement, and (c) CCSH-based cement were aged for 7 days in an acidic solution (pH = 5). The visible corrosion and change in mass reveal the extent to which CCSH phases are resistant to acid attack when compared to the alternatives presented in this work.54

Figure 4.5. Lifecycle analysis results of OPC and CCSH cement reported on here suggest three major ways in which emission profiles are significantly different. First, significantly less limestone is required for CCSH cement, leading to fewer emissions from calcination. Second, during pyroprocessing, the lower temperatures required to make pseudowollastonite saves on fuel emissions, compared to compared to OPC clinker. Finally, while curing, CCSH cement uptakes a significant amount of CO₂ (here, shown in terms of data from 7-day curing).56

Chapter 1. Overview

1.1. Motivation and Objectives

Chemical reactions involving cements have been studied for millennia. Ancient Roman engineers discovered that certain sources of calcium and silicon could be combined with water to produce a useful building material that hardened over time. That technology was lost and a similar one was discovered in the 18th century and has been an important topic of research and of our daily lives since then, in the form of Portland cement. Each year, nearly 4 tonnes of concrete made from Portland cement are produced per person on the planet. In addition, mineral silicates are the most abundant class of rock-forming minerals and their reaction with water and carbon dioxide are important in many natural and engineered processes. But, after centuries of industrial use and scientific inquiry, many of the reaction pathways that influence the synthesis and weathering of these materials are still not yet fully understood, underscoring their complexity and the need to understand them in a variety of contexts. Further, there is an urgent need to minimize global carbon emissions and create solutions to address the drivers and impacts of global climate change. Coupling the ideas of resource and energy conservation, resilience of engineered systems, and carbon management techniques is critical to sustaining the environment in which we live.

Nearly 85 million tonnes* of ordinary Portland cement (OPC) are consumed in the United States each year with between 10-20% of that used to manufacture pre-cast concrete products.^{1,2} Global consumption of cement is increasing is driven largely by development in China, which is currently responsible for 2.4 out of the 4.1 billion tonnes of worldwide cement production per year, shown in Figure 1.1.¹ To produce cement at the global scale requires about 14 EJ, or 3-4% of the world's energy consumption, and results in the production of 5-10% of global CO₂ emissions.³⁻⁵

* 'Tonne' implies a metric tonne (1,000 kg) as opposed to a short ton (approximately 907.2 kg)

Those figures are particularly impactful considering that, in general, OPC structures have designed lifetimes of decades. For example, most of nation’s bridges were designed with a 50-year lifespan and 9.1% are currently structurally deficient, with the national backlog of bridge rehabilitation costs currently at \$123 billion.⁶ Short lifetimes increase the product’s lifecycle impact in a range of engineering applications, especially in marine environments, where calcium hydroxide and calcium silicate hydrate (CSH) gels (the products of cement hydration) dissolve and generate flow paths to rebar or other internal reinforcement of the material.⁷⁻⁹ The resulting networks of cracks allow water penetration, which can impact the mechanical integrity of cements subject to freeze/thaw cycles.

In deep subsurface environments such as those associated with hydrocarbon production, CO₂ storage, and enhanced geothermal energy production, there is growing interest in managing environmental impacts associated with undesirable fluid migration.¹⁰⁻¹⁵ Many of these technologies rely on high-pressure fluid injection to the subsurface and under certain conditions,

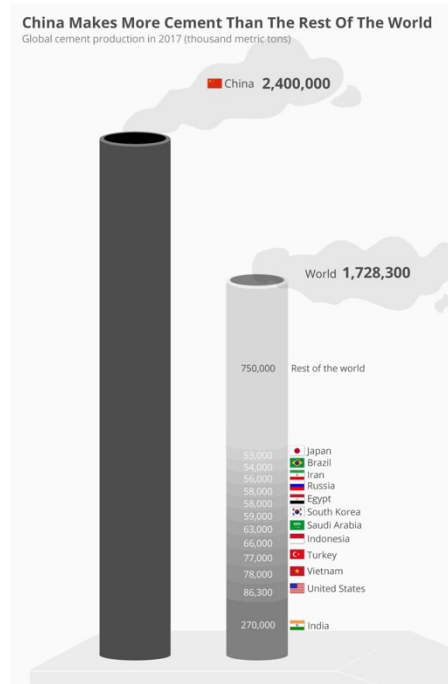


Figure 1.1. China’s 2.4 billion tonnes of cement produced in 2018 was more than the rest of the world’s production, combined. Figure: Niall McCarthy, Forbes, USGS.

this activity can lead to groundwater contamination, fugitive emissions, and induced seismicity. Current methods of mitigating undesirable fluid migration center around two main techniques: plugging wellbores with Portland cement or carbonating *in situ* minerals to generate pore-blocking solid carbonates in the formation matrix itself. Each of these methods has clear advantages and shortcomings. Portland cement is readily available and economical but it is becoming increasingly clear that it is susceptible to corrosion, degradation, and cracking over the course of decades. Mineralization reactions have the distinct advantage of high injectability and the potential to sequester CO₂ in a solid form. However, many of the solid carbonate precipitates readily dissolve in acidic conditions (for example, when the concentration of dissolved CO₂ is high) and allow fluid to migrate over time. Research concerning the utilization and control of the deep subsurface is highly active as the search for cleaner energy and carbon management is at an all-time high and, because many of these technologies are relatively new, the techniques for managing them are generally not yet optimized.

The work presented here answers several fundamental and applied research questions surrounding the durability, strength, and permeability of materials created via a novel chemical reaction pathway involving calcium silicate, CO₂, and water. The inspiration for these materials stems from ancient Roman cement, which is the foundation for many millennia-old concrete

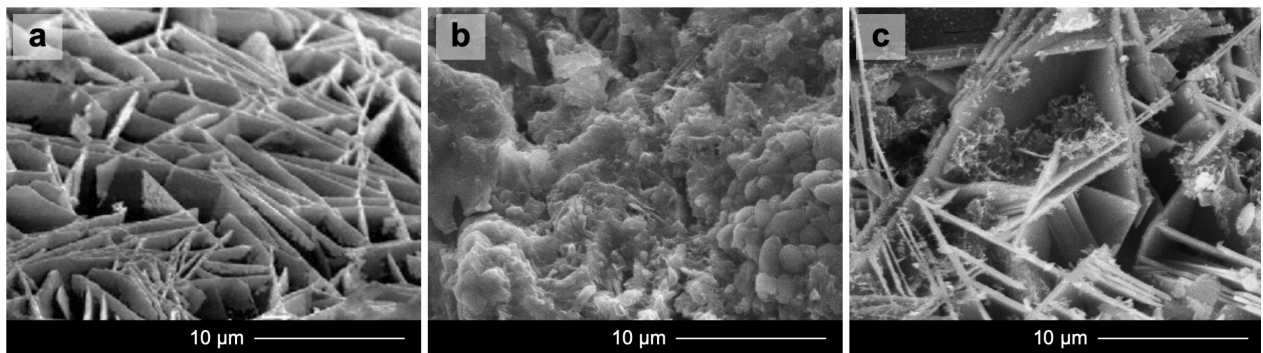


Figure 1.2. (a) Crystalline calcium silicate hydrate phases found in ancient Roman cement are distinctly different from (b) amorphous calcium silicate hydrate gels that typically form in cured ordinary Portland cement and exhibit a similar composition and morphology to (c) calcium silicate hydrate phases found in this work.

structures that are still standing today. Roman cement (Figure 1.2a¹⁶, compared to OPC, 1.2b) has been found to gain strength over time and retard the spread of microfractures. Its strength and resilience come from the hydration of calcium oxide and pozzolana, a form of porous silica of volcanic origin that contained cations such as Na⁺, Ca²⁺, and Mg²⁺. The reaction produced crystalline calcium silicate hydrate phases (CCSHs) such as tobermorite (Ca₅Si₆O₁₆(OH)₂·4H₂O), phillipsite ((Ca,Na₂,K₂)₃Al₆Si₁₀O₃₂·12H₂O), and strätlingite (Ca₂Al₂SiO₇·8H₂O). Not only do these products provide excellent strength characteristics but, more importantly, they resist the attack of alkali cations, which accelerates the disintegration of Portland cement. While Roman cement has proven itself to be among society's most impressive building materials, its production is severely hindered by the need for volcanic silica that is limited and unavailable in most regions of the world.

In addition to the mineral phases in Figure 1.2, the reaction of mineral silicates with CO_{2(aq)} is highly studied since it is representative of natural and accelerated weathering processes and because it has the potential to sequester carbon in the solid carbonate form.¹⁷⁻²⁰ A common mineral silicate to study in this system is CaSiO₃ because it reacts relatively quickly, compared to other mineral silicates, allowing studies on experimentally-feasible timescales. Typically, when CO_{2(aq)} and CaSiO₃ react, the expected products are solid calcium carbonate (CaCO₃) and amorphous silica (SiO₂). The work for this dissertation began with the investigation of that reaction in the context of geologic carbon sequestration. Indeed, when carbonation reactions were carried out with wollastonite (CaSiO₃, Wol), only calcium carbonate and silica formed. However, when the reactions were carried out with the polymorph, pseudowollastonite (CaSiO₃, PWol), CCSHs that resembled those of Roman cements in both morphology and chemistry were discovered (Figure 1.2c). Because of the relation of the calcium silicate hydrate phases to Roman cement mineralogy

and because of the potential to utilize and sequester carbon, this dissertation answers several research questions to fill fundamental and applied gaps in knowledge by characterizing the carbonation and hydration of PWol and properties of the produced mineral phases as they relate to permeability in porous media, as well as to strength and chemical stability in cement applications.

Those questions are:

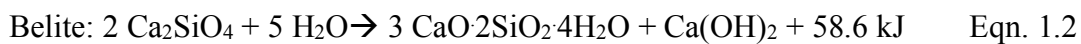
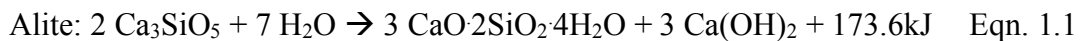
1. *Why does the aqueous carbonation of pseudowollastonite result in different products than its polymorph, wollastonite, and how are the products fundamentally different?*
2. *How do these products differ in terms of their impact on fluid flow in porous media and ability to sequester carbon in the subsurface?*
3. *Can these products be leveraged to produce environmentally sustainable cement that is comparable to traditional Portland cement?*

1.2. Background

This section seeks to preface the topics of research that are prevalent throughout this dissertation. It should be noted that each of the subsequent chapters contains a more detailed background of pertinent topics that are presented there.

1.2.1. Ordinary Portland Cement

The chemistry of ordinary Portland cement is complex and varied. Many of the relationships between molecular and macro-scale properties in cements are based on the ratio of CaO to SiO₂ in the CSH gel that forms upon hydration of dicalcium and tricalcium silicates (Ca₂SiO₄ and Ca₃SiO₅).²¹



By definition, OPC mixes must contain a ratio of calcium oxide to silica ≥ 2 so the CSH gel that precipitates has a moderate-to-high Ca:Si ratio (typically 1.4-2 as Eqns 1.1 and 1.2 generalize), with the remaining Ca as calcium hydroxide, $\text{Ca}(\text{OH})_2$. Calcium hydroxide occupies up to 15% of the volume of cured cement and does not contribute to its overall strength.²² Further, it is water-soluble, contributing to increased porosity of the concrete and accelerated dissolution and degradation over time.

The degradation of OPC is problematic in roadway, marine, or subsurface applications where dissolved magnesium, sulfate, sodium, and carbonate have been shown to quickly dissolve calcium hydroxide and CSH gels.⁹ In CO_2 injection wells, there exists a particular concern regarding the cement's stability over time. In these systems, carbon dioxide dissolves in water at high pressure, forming carbonic acid, which reacts with calcium hydroxide in the cement, yielding calcium carbonate. The calcium carbonate continues to react with excess carbonic acid to form calcium bicarbonate, which is water-soluble. Barlet-Gouedard et al. studied the degradation of the Portland cement in a wellbore system with a diffusion-dominated supply of CO_2 .²³ Their analysis suggests that for a common cement sheath of 2 to 2.5 cm, full degradation of the casing could occur on the order of several years. Brunet et al. reported that the mechanical strength of the degraded zone may be less than half the original strength and permeability and diffusivity typically vary by 1-3 orders of magnitude over time.²⁴

In addition to these issues, OPC concrete comes at a high environmental cost. The principal raw material for most OPC is calcium carbonate (limestone), which must be mined, transported to manufacturing facilities, and heated to approximately 1450 °C with sources of silica to form clinker. The clinker is mixed with gypsum ($\text{CaSO}_4 \cdot 2\text{H}_2\text{O}$) to create cement. One analysis estimates that the manufacturing of one tonne of OPC generates approximately 70 kg CO_2 from electricity

usage, approximately 340 kg CO₂ from fossil fuel consumption and more than 480 kg CO₂ from calcination processes to make clinker.²⁵

1.2.2. Environmentally Preferable Cement Materials

Concerted effort to reduce the environmental burdens of cement production over the past two decades has focused on using waste material and minimizing production processes to avoid environmental impacts. Among the most prevalent efforts in this regard are the substitution of fly ash (typically 15-20%) for cement,^{26,27} the use of natural pozzolans,^{28,29} the use of waste materials,³⁰ and the incorporation of nanocomposites into the cement matrix.³¹ Each of these technologies offers unique advantages and disadvantages compared to OPC and all cement alternatives are subject to constraints related to the availability of feedstocks used in their formulation and by the cultural/technical preference of construction/concrete engineers.³²

1.2.3. Carbonation of Conventional Cements

Carbonation of OPC occurs naturally from CO₂ in the air and can affect the long-term performance of the material.³³ Carbonated cement has been found to perform poorly in earthquake resistance due to poor ductility, particularly after experiencing a peak load.³⁴ Carbonation of concrete also serves as a means by which carbon dioxide can be stored. Shao et al. showed, through accelerated carbonation experiments on conventional concrete blocks, 16% CO₂ uptake and improvements in strength.³⁵ Monkman and Shao tested several types of concrete blocks that had been subjected to accelerated carbonation and concluded that the presence of fly ash increased the amount of CO₂ sequestered (because the Ca(OH)₂ in fly ash decomposes to produce water, which is essential to the carbonation process), although strength gain was negligible.³⁶

1.2.4. Carbonation of Mineral Silicates

In an effort to address some of the challenges of conventional cement, a group of researchers recently pioneered the formulation of wollastonite-based cements and then commercialized them through a company called Solidia, Inc.³⁷ Cured Solidia cement contains no calcium hydroxide – only calcium carbonate and silica.³⁸ Their pre-formed concrete structures are cured for >20 hours at 60-90°C and atmospheric pressures of nearly-pure, gas-phase CO₂. The resulting solid phase consumes a significant amount of CO₂ in the form of calcite (CaCO₃). Solidia is making progress toward developing a more carbon-neutral alternative to conventional Portland cement, though the high concentration of calcite in their product leaves it susceptible to acid attack. The dissolution of calcite by weak acids is the same process that leads to the creation of sinkholes and caves from groundwater in some environments or the dissolution of statues from acid rain in others.³⁹

1.2.5. Roman Cement

In contrast to conventional or Solidia cements, ancient Roman cement has been found to contain high concentrations of platy crystalline mineral silicate phases, such as tobermorite and phillipsite, which penetrate and transect amorphous and porous silica phases, increasing the mechanical strength of the cement.¹⁶ Unlike Portland cement, where the ratio of CaO to SiO₂ is greater than 2, Roman cements exhibited lower calcium content and higher silica content. Specifically, the Romans used 1 part CaO (derived from limestone) to 2-3 parts pozzolana, which was mostly porous SiO₂ from regional volcanic rock that often displayed high concentrations of ions such as sodium, chloride, potassium, calcium, magnesium, and aluminum. The cement quickly gained strength via hydration reactions where these ions, CaO, and water generated calcium-(aluminum)-silicate hydrate [C(A)SH] gel phases. Over time, they diagenetically

transitioned to crystalline phases, which are sometimes broadly classified as ‘tobermorites’ and are insoluble in most natural environments.⁴⁰ It is generally accepted that the alkalinity of sea water that the concrete was mixed with and was exposed to over centuries contributed to the formation of the crystalline phases, which gained considerable strength as they grew and transected one another, while remaining relatively ductile. That strength and ductility, along with chemical resilience of the tobermorites resulted in one of the most resilient building materials in history.⁴¹ A testament to that is the Pantheon’s dome, which is still the world’s largest unreinforced concrete dome, with a diameter of 43 meters, shown in Figure 1.3.⁴²



Figure 1.3. The Pantheon, completed ca. 126 AD demonstrates the longevity and resilience of Roman cement. Photo: Jean-Christophe Benoist, Wikimedia Commons

Chapter 2. Calcium Silicate Crystal Structure Impacts Reactivity with CO₂ and Precipitate Chemistry

2.1. Chapter Summary

The reaction of CO_{2(aq)} with calcium silicates creates precipitates that can impact fluid flow in subsurface applications such as geologic CO₂ storage and geothermal energy. These reactions nominally produce calcium carbonate (CaCO₃) and amorphous silica (SiO₂). Here we report evidence that the crystal structure of the parent silicate determines the way in which it reacts with CO₂ and the resulting structures of the reaction products. Batch experiments were carried out using two polymorphs of a model calcium silicate (CaSiO₃), wollastonite (chain-structured) and pseudowollastonite (ring-structured), at elevated temperatures (150 °C) and partial pressures of CO₂ (0 – 11 MPa). Reaction of CO_{2(aq)} with wollastonite produced CaCO₃ and SiO₂, whereas reaction of CO_{2(aq)} with pseudowollastonite produced plate-like crystalline calcium silicate phases, along with CaCO₃ and SiO₂, illustrated in Figure 2.0. A reaction mechanism is proposed that explains the observations in relation to dissolution of the parent silicate, pH of the solution, and presence of nucleation sites. The mechanism is supported with ICP-OES measurements and SEM/TEM-SAED characterization of solid products. These findings are important for a number of reasons; among them, the fact that the crystalline silicate precipitates are more stable than CaCO₃ at low pH conditions, which could be valuable for creating permanent seals in subsurface applications. †

† This chapter was adapted from: Plattenberger, D. A., Ling, F. T., Tao, Z., Peters, C. A., & Clarens, A. F. (2018). Calcium Silicate Crystal Structure Impacts Reactivity with CO₂ and Precipitate Chemistry. *Environmental Science & Technology Letters*, 5(9), 558-563.

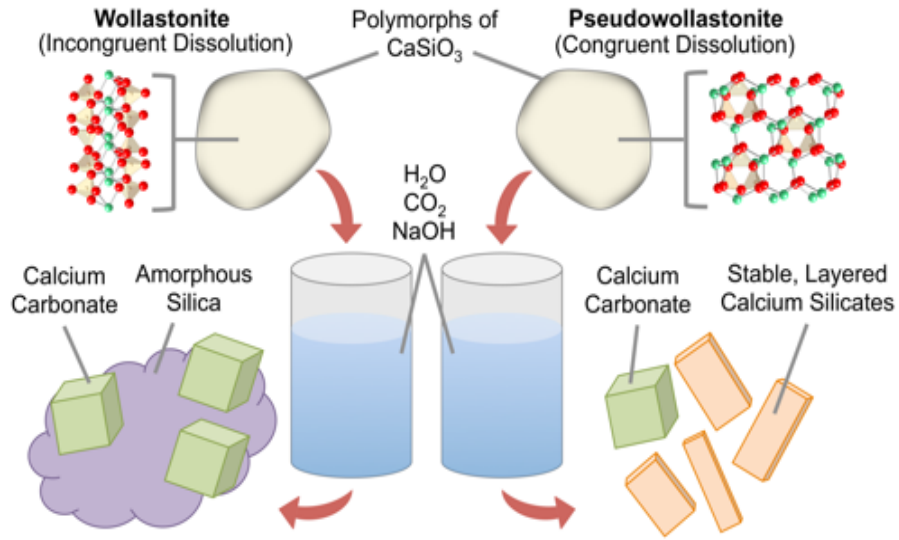


Figure 2.0. Experimental data in this chapter shows that the reaction of wollastonite with $CO_{2(aq)}$ produces $CaCO_3$ and amorphous SiO_2 while the reaction involving its polymorph, pseudowollastonite, has the potential to produce crystalline calcium silicate hydrate phases in addition to $CaCO_3$ and amorphous phases.

2.2. Introduction

In deep subsurface environments such as those associated with hydraulic fracturing, CO_2 storage, and enhanced geothermal energy production, there is growing interest in managing environmental impacts associated with undesirable fluid migration.^{10–15} The targeted deployment of mineral precipitation reactions is one strategy that has been proposed to manage the fate of fluid flow properties in porous media.^{20,43,44} Calcium silicates are a common and broad class of minerals that could be used in these applications. They dissolve in acid to produce cations (Ca^{2+}) and amorphous silica (SiO_2) which can create an opportunity for pore plugging.



The rates at which the cation and silica are released into solution have been shown to vary considerably based on the crystal structure of the parent compound, even among minerals having the same chemical formula.^{45,46} Wollastonite, $CaSiO_3$, dissolves incongruently, resulting in non-stoichiometric release of calcium and silicon.^{47,48} Wollastonite has a pyroxenoid silicate chain structure and resists rapid Si leaching due to the strength of Si-O bonds in the silicate chains,

resulting in preferential Ca leaching. In contrast, the polymorph pseudowollastonite has an isolated trisilicate ring structure in which the Ca^{2+} ions are weakly bonded to O atoms resulting in rapid, stoichiometric dissolution and equal release of Ca and Si during dissolution.^{49,50}

Under conditions where $\text{CO}_{2(\text{aq})}$ is present, the cation can complex with carbonate ions and precipitate as calcium carbonate (CaCO_3).



In this reaction, CO_2 provides both the reactant (carbonate ions) and the source of hydrogen ions (carbonic acid). If CO_2 is present in high enough concentrations, it will drive the reaction to the left. Understanding these competing effects is critical for controlling this chemistry in engineered applications.

When wollastonite dissolves in the presence of $\text{CO}_{2(\text{aq})}$, a calcium-depleted leached layer forms and the calcium ions can react with $\text{CO}_{2(\text{aq})}$ to form solid carbonates⁵¹ in accordance with Eqns 2.1 and 2.2. In contrast, we hypothesized that when pseudowollastonite dissolves in the presence of $\text{CO}_{2(\text{aq})}$, the availability of cations and high concentrations of dissolved silica can result in precipitation of non-carbonate mineral phases with low ratios of cation to silica (≤ 1) similar to tobermorite⁵² ($\text{Ca}_5\text{Si}_6\text{O}_{16}(\text{OH}_2)\cdot 4\text{H}_2\text{O}$) and magadiite⁵³ ($\text{NaSi}_7\text{O}_{13}(\text{OH})_3\cdot 4(\text{H}_2\text{O})$). Those products have been noted for their high strengths,⁵⁴ adsorption properties,⁵⁵ and low reactivities⁵⁶ and the availability of nucleation sites has been shown to play an important role in controlling the morphology and rate of their precipitation.^{57,58}

The reaction of calcium silicates with CO_2 has been well studied in the context of carbon sequestration. Examples include reactions in basalts^{17,59} and exposed mantle peridotites,⁶⁰ engineered weathering of silicate minerals,^{61,62} and sequestration in deep saline aquifers.⁶³ We are interested in these reactions not because of their potential to mineralize CO_2 directly but because

of their potential to create precipitates other than carbonates. Silicates could be delivered into pore spaces, where resulting precipitates could seal porous and fractured rocks and cements or stabilize and encase carbonate precipitates.⁶⁴

Here we present new evidence for the role of crystal structure (rather than simply elemental composition) of the parent silicate in controlling the chemistry of the precipitated minerals. This is a connection that has not yet been reported in the literature and is one that could have important implications in a number of applications in the subsurface requiring strength and stability. Batch experiments were carried out using wollastonite and pseudowollastonite under a range of pH, pressure, and CO₂ conditions to establish a proposed mechanistic understanding of the dissolution and precipitation reactions that control the formation of these chemically-stable mineral phases.

2.3. Materials and Methods

2.3.1. Materials

A citrate-nitrate gel auto-combustion method was used to make a calcium silicate ash that was calcined at 950°C or 1250°C for two hours to produce wollastonite and pseudowollastonite, respectively.⁶⁵ The calcium silicate powders were then ground separately and sieved to isolate the 74-149 μm fraction. The crystal structures and morphologies of the calcium silicates were confirmed via powder X-ray diffraction (XRD), coupled with scanning electron microscopy (SEM) and energy dispersive X-ray spectroscopy (EDS). In experiments where sand was used to test the effects of heterogeneous nucleation, Ottawa sand (US Silica, F-50) was sieved to obtain the 250-595 μm fraction, washed in 1N HCl (Sigma Aldrich), and rinsed with deionized water (>18.0 MΩ-cm). Sodium hydroxide (98% NaOH, Sigma Aldrich) and sodium chloride (99% NaCl, EM Science) were used as received.

2.3.2. Batch Experiments

To investigate these reactions, experiments were conducted in batch systems to isolate the chemical processes and enable observation of reaction products, while limiting macro-scale mass-transfer limitations and heterogeneity that exists in column experiments. For each set of experimental conditions, 15mg of wollastonite and pseudowollastonite powder were placed into separate, identical, Teflon boats (approx. 0.75 cm³) and put in a single Teflon-lined stainless-steel pressure vessel. Within each boat, 1g of sand and 0.5mL of deionized water (with various concentrations of NaOH and/or NaCl) were added. Pressure vessels were heated to 150±3°C. CO₂ was injected into the vessels via a syringe pump (Teledyne ISCO) and the concentration of dissolved CO₂ was calculated by its partial pressure in the headspace using PHREEQC, equilibrated with the water phase, for each CO₂ concentration that was tested. Once CO₂ pressure equilibrated, the pump was switched to nitrogen gas and pressure was increased to 15.5MPa. Each experiment was conducted for 24 hours and afterwards, the samples, in the Teflon boats, were oven-dried at 75°C where sheet silicate precipitates are not expected to form.^{66,67} Upon drying, the sand and powders became separable and the powders were then rinsed three times to remove any remaining NaOH and dried at 50°C for 12 hours. The products of select samples were then divided and a portion was acid-washed in pH 5.5 acetic acid/sodium acetate buffered solution for 6 hours.⁶⁸ To remove the acid, those samples were again rinsed and oven-dried.

2.3.3. Analytical Methods

The reaction products were analyzed via SEM-EDS (FEG Environmental-SEM, Oxford AZtec EDS system) for morphology and elemental composition and via powder XRD (Bruker D8 Advance) for phase identification. Data were collected with a Ag tube source ($\lambda = 0.56 \text{ \AA}$) over a 2θ range of 4° – 20°, with a step size of 0.025° – 0.05°. Identification was performed using the

powder diffraction database in Diffrac.Eva V3.1 (Bruker). For single particles from one sample, transmission electron microscopy (TEM), selected-area electron diffraction (SAED), and additional EDS were conducted (FEI Talos (S)TEM, 200 kV). Inductively coupled plasma optical emission spectrometry (ICP-OES, Thermo Scientific iCap 6200) was also used to analyze aqueous phases to determine relative dissolution rates of wollastonite and pseudowollastonite.

2.4. Results and Discussion

2.4.1. Layered Calcium Silicate Formation

The experiments conducted here, summarized in Table 2.1, yielded very different products for wollastonite and pseudowollastonite. When wollastonite reacted with $\text{CO}_{2(\text{aq})}$, only amorphous silica and CaCO_3 formed. Conversely, pseudowollastonite yielded a variety of morphologies observed via SEM, suggesting the presence of multiple mineral phases. For each experiment, the relative abundance of reaction products is listed in order of prevalence based on qualitative SEM/EDS microscopy coupled with XRD. For instances of CaCO_3 , calcite and aragonite were identified via XRD, except in samples 0, 6, and 7, where calcite was reported. Figure 2.1 presents representative micrographs and EDS spectra of the morphologies described in Table 2.1. The layered calcium silicate phases are likely crystalline calcium silicate hydrates. TEM-SAED confirmed that the material was crystalline but did not match pseudowollastonite. TEM-EDS showed that one of the platelets had a 54:46 Ca:Si ratio. Previous work⁶⁹ identified trace amounts of nano-scale calcium silicate hydrates after reacting wollastonite with CO_2 while others³⁷ noted silicate polymerization during carbonation of natural wollastonite under high relative humidity conditions. To our knowledge, no work to date has reported the formation of such dissimilar reaction products from polymorphs of the same parent silicate.

Table 2.1. Selection of experimental conditions and reaction products described in this work. Products listed in accordance to prevalence, as determined by SEM/EDS analysis coupled with XRD. Here, “irregular” phases (IR) include amorphous silica as well as unreacted CaSiO₃, solid carbonates include Calcite (Cal) and Aragonite (Ara) and layered calcium silicate phases (plate-like (PL)) are also observed.

ID	pCO ₂ (MPa)	NaOH (M)	pH ^a	inter- face	wollastonite reaction products	pseudowollastonite reaction products	analytical techniques
0	0	0.1	10.5	Sand	Ir	Ir	SEM, EDS
1	1.1	0	3.9	Sand	Ir>Ara>Cal	Ir>Ara>>PL	SEM, EDS, XRD
2	1.1	0.1NaCl	3.9	Sand	Ir>Cal>>Ara	Ir>Ara>>PL	SEM, EDS, XRD
3	1.1	0.1	6.7	None	Ir>Cal>>Ara	Ir>Ara	SEM, EDS, XRD
4 ^b	1.1	0.1	6.7	Sand	Ir>Cal>>Ara	PL>Ara>Ir	SEM, EDS, XRD
5	1.1	0.1	6.7	Sand	Ir>Cal>>Ara	PL>Ara>Ir	SEM, EDS, XRD, TEM
6	5.5	0.1	5.9	Sand	Ir>Cal	Cal>Ir	SEM, EDS
7	11	0.1	5.7	Sand	Ir>Cal	Cal>Ir	SEM, EDS

^a = Calculated for batch solution at equilibrium with CO₂ at 150°C using PHREEQC

^b = Experiment conducted at low total pressure (1.1MPa)

The differences observed between the reaction products of wollastonite and pseudowollastonite were sensitive to both the presence of CO₂ and pH. In experiment 0, where no CO₂ was present, no layered calcium silicate phases were observed from reacting either polymorph. At high CO₂ concentrations (experiments 6 and 7), CaCO₃ was the predominant reaction product and significantly more CaCO₃ existed in pseudowollastonite than in wollastonite reaction samples.

When calcium silicates reacted with intermediate concentrations of CO₂, the reaction products depended on several factors, including the initial CaSiO₃ crystal structure, pH, and the availability of heterogeneous nucleation sites (i.e., sand). Comparison of the results from experiments 3 and 5 suggest that, in pseudowollastonite experiments, nucleation sites are needed to yield layered calcium silicate precipitates. Also, where pH was increased using 0.1 M NaOH (experiments 4 and 5), an abundance of plate-like phases was observed. To better understand the role of Na in this reaction mechanism (since NaOH was used), experiment 2 was conducted at the same Na molar concentration as experiment 5, with NaCl rather than NaOH. Only a very small

quantity of plate-like phases was found in experiment 2 and the results nearly mirror experiment 1. Overall, XRD analyses suggest that calcite was the predominant CaCO_3 mineral in wollastonite samples and aragonite was predominant in pseudowollastonite samples. Because pseudowollastonite dissolves more rapidly, this observation is likely due to the relative concentrations of dissolved calcium in the aqueous phase.⁷⁰ All experiments were conducted at high total pressure (15.5 MPa) to simulate conditions in the deep subsurface except experiment 4, which was conducted at 1.1 MPa, to confirm that total pressure had little-to-no effect on products.

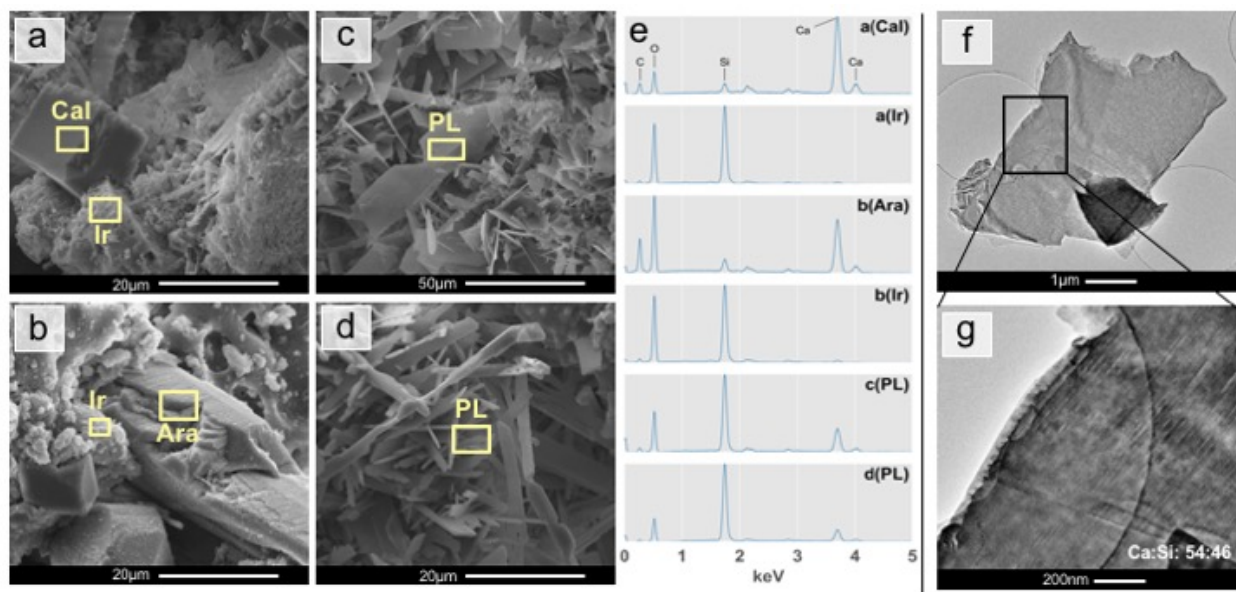


Figure 2.1. Representative SEM micrographs (a-d) of the phases produced in these experiments, including calcite (Cal), aragonite (Ara), and irregular silica phases (Ir). At elevated pH and moderate dissolved carbonate concentrations, appreciable quantities of plate-like (PL) calcium silicates are produced (c,d). EDS spectra (e) are presented for each of the identified phases in (a-d). The spectra show that the PL phases are rich in both calcium and silica. TEM micrographs (f,g) show the nature of the PL phases and EDS confirms an abundance of Si and Ca.

2.4.2. Mechanism for Layered Calcium Silicate Formation

These experiments provide insight into the mechanism that governs the formation of layered calcium silicates instead of CaCO_3 . A schematic of the proposed mechanism is presented in Figure 2.2. Figure 2.2a depicts the reaction of wollastonite in water, where the pyroxenoid silicate chains lead to non-stoichiometric dissolution of calcium ions and a silica network that

hinders further dissolution of calcium. Previous work⁷¹⁻⁷⁴ demonstrated that in silicate-glass corrosion, this leached-layer of silica gel restructures and cross-links, effectively closing pores around the periphery of the glass. However, hydrolysis of Si-O bonds allows the limited release of polymerized vitreous silica, meaning the aqueous phase surrounding the solid surface is therefore calcium-rich but relatively low in silica, which is supported by the ICP-OES data in Figure 2.2a. When CO₂ is present, the precipitation of CaCO₃ is highly favorable. In contrast, Figure 2.2b depicts the case of pseudowollastonite reacting with water and CO₂. The trisilicate rings are readily dissolved, releasing stoichiometric quantities of Ca and Si (silicic acid, Si(OH)₄). With the exogenous elevation of the pH (NaOH), the concentration of dissolved Si increases, becomes supersaturated, complexes with calcium (and possibly, carbon) and precipitates as layered calcium silicates, with Ca:Si stoichiometry dependent on the local ion concentrations. Simultaneously, some Ca may be consumed by the precipitation of CaCO₃. Not depicted in the figure is the impact of temperature on the morphologies and crystal structures of precipitates but previous work^{66,67} as well as our experiments suggest that the layered calcium silicates are more prevalent at temperatures >120 °C. Experiments carried out over longer timescales, not shown, produced similar results suggesting the results are not time-dependent over the timescales evaluated here.

ICP-OES analyses confirmed that dissolution rates in CaSiO₃ could be driving the difference in precipitate chemistry. Experiments were carried out to mimic the conditions of experiment 4 except HCl was used in place of CO₂ to prevent rapid CaCO₃ precipitation. The molar concentrations of aqueous Ca and Si (0.55g of 74-150µm CaSiO₃ in 500mL stirred water) upon reaching 150 °C are shown. The plots show that Ca dissolves more quickly than Si in wollastonite but dissolve stoichiometrically in pseudowollastonite. Additionally, these

experiments produced no crystalline silicate phases or CaCO_3 (as determined by SEM/EDS) which underscores the importance of CO_2 in the system.

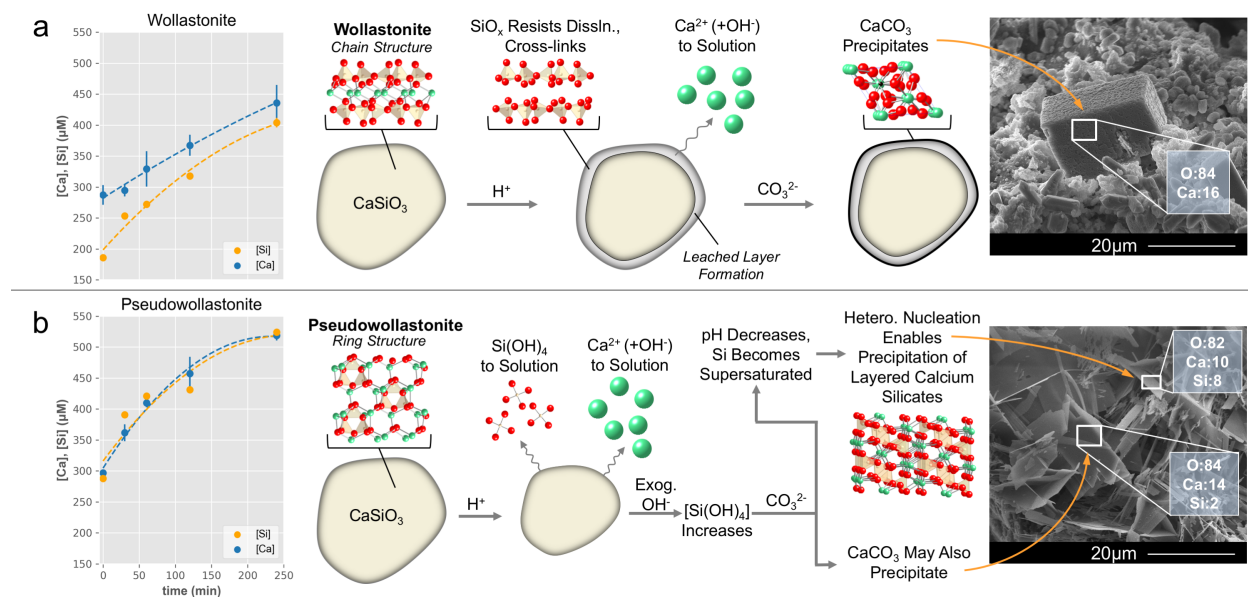


Figure 2.2. A proposed mechanism for how the crystal structures of wollastonite (a) and pseudowollastonite (b), both polymorphs of CaSiO_3 , influence the reactions that proceed in the presence of $\text{CO}_2(\text{aq})$. Wollastonite dissolves non-stoichiometrically, as evidenced by ICP-OES measurements of dissolved Si and Ca. The resulting leached layer of SiO_x is depicted, as is the reaction of calcium with dissolved carbonate to generate CaCO_3 . Pseudowollastonite dissolves congruently. The elevated concentration of dissolved silica promotes precipitation of layered calcium silicates. In parallel, CaCO_3 may precipitate, consuming dissolved carbonate and some calcium ions.

The results of the acetic acid washing provide insights into the chemical stability of the layered calcium silicates produced relative to CaCO_3 . Representative SEM micrographs and layered EDS maps (Ca, Si, C) are presented in Figure 2.3 of (a) unreacted pseudowollastonite, (b) products from CO_2 -reacted pseudowollastonite (experiment 4), and (c) products from CO_2 -reacted and acid-washed pseudowollastonite (experiment 4). The EDS maps in (b) show intense regions of calcium and carbon that align with the regions that appear to be CaCO_3 . The remainder (and majority) of the sample is comprised primarily of plate-like phases, which remained entirely intact after acid washing, along with some irregular phases. CaCO_3 could not be found in the acid-washed samples.

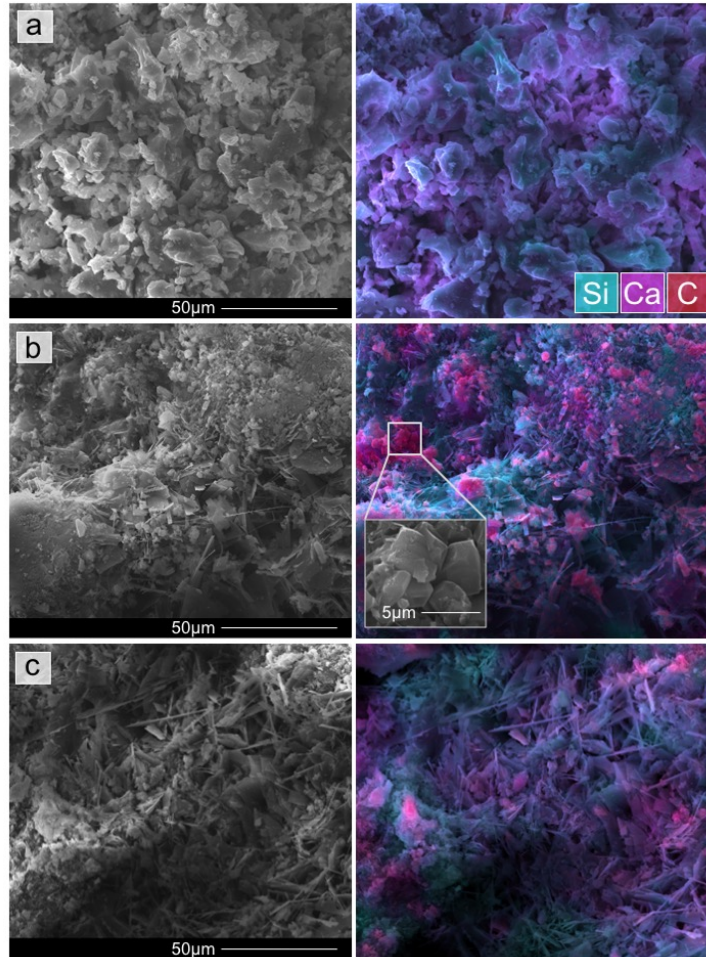


Figure 2.3. SEM micrographs and EDS analyses of unreacted pseudowollastonite (a) showed no evidence of CaCO_3 while those from reacted pseudowollastonite (b) showed a significant quantity. After acid washing, CaCO_3 was not observed while plate-like phases remained, unaltered (c).

The chemical resilience of the layered crystalline calcium silicates suggests they could have important applications in subsurface engineering contexts, among others. While pseudowollastonite is less common than wollastonite, the role of ion concentration revealed here could be leveraged to deliver mixtures of other more abundant minerals that would produce ideal reactant concentrations to generate layered calcium silicates in applications such as geologic CO_2 storage, geothermal energy, or hazardous waste containment. Pseudowollastonite nanoparticles or some combination of calcium and silica from waste streams delivered at the right ratios could create the pore conditions that would result in the precipitation of stable mineral phases, which

could enable dramatic decreases in permeability, even in harsh environmental conditions. In *ex situ* carbon storage and cement applications, these results could inform novel ways to produce unreactive passivating layers on carbonates that would resist weathering and improve the long-term stability of the materials produced.

2.5. Chapter 2 Acknowledgements

Support for this work came from the United States Department of Energy National Energy Technology Laboratory (Grant DE-FE0026582) and the U.S. National Science Foundation (to AFC) (CBET-1134397). We acknowledge the use of Princeton's Imaging and Analysis Center, which is partially supported by Princeton Center for Complex Materials from National Science Foundation (NSF)-MRSEC program (DMR-1420541).

Chapter 3. Targeted Permeability Control in the Subsurface Via Calcium Silicate Carbonation

3.1. Chapter Summary

Efforts to develop safe and effective next-generation energy and carbon-storage technologies in the subsurface require novel means to control undesired fluid migration. Here we demonstrate that the carbonation of calcium silicates can produce reaction products that dramatically reduce the permeability of porous media and that are stable. Most calcium silicates react with CO₂ to form solid carbonates but some polymorphs (here, pseudowollastonite, CaSiO₃) can react to form a range of crystalline calcium silicate hydrates (CCSHs) at intermediate pH, illustrated in Figure 3.0. High-pressure (1.1–15.5 MPa) column and batch experiments were conducted at a range of temperatures (75–150 °C) and reaction products were characterized using SEM-EDS and synchrotron μXRD and μXRF. Two characteristics of CCSH precipitation were observed, revealing unique properties for permeability control relative to carbonate precipitates. First, precipitation of CCSHs tends to occur on the surface of sand grains and into pore throats, indicating that small amounts of precipitation relative to the total pore volume can effectively block flow, compared to carbonates which precipitate uniformly throughout the pore space. Second, the precipitated CCSHs are more stable at low pH conditions, which may form more secure barriers to flow, compared to carbonates, which dissolve under acidic conditions.[§]

[§] This chapter was adapted from: Plattenberger, D., Ling, F. T., Peters, C. A., & Clarens, A. F. (2019). Targeted Permeability Control in the Subsurface Via Calcium Silicate Carbonation. *Environmental Science & Technology*.

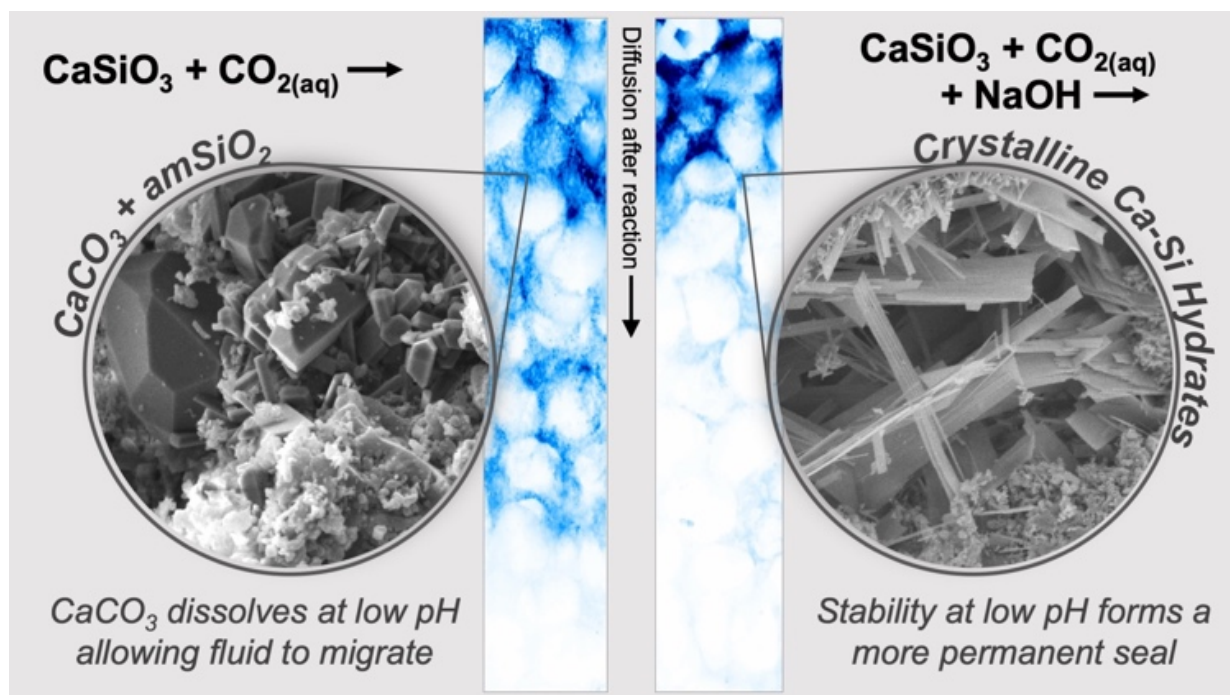


Figure 3.0. This chapter investigates the efficacy of (left) carbonate precipitates and (right) crystalline calcium silicate hydrate phases to limit flow in porous media. SEM micrographs of the morphology of both types of precipitates is shown alongside synchrotron X-ray fluorescence maps of the inlet of pseudowollastonite-containing sand columns that were reacted in the presence of CO₂ under conditions representative of the subsurface.

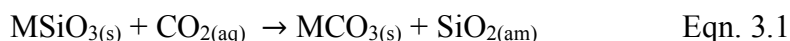
3.2. Introduction

The subsurface environment has traditionally been the source of most of our energy but a growing number of applications seek to use it to offset the environmental impacts of energy production.^{20,75,76} Geologic carbon storage (GCS), enhanced geothermal energy (EGS), and compressed air energy storage leverage some of the unique characteristics of the subsurface (e.g., its size, temperature, and pressure) to store fluids or extract heat.^{77–82} Because of the pressure gradients associated with fluid injection/production, strategies are needed to control fluid flow in target formations. Geophysical and/or geochemical alteration of the subsurface environment can create new and undesirable pathways for fluid migration.^{83,84} In EGS, these are often referred to as thief zones, and undermine the economic viability of production. In GCS, leakage can contribute

to groundwater contamination.⁸⁵ In addition, the influence that fluid migration has on induced seismicity remains problematic and difficult to predict.^{86–89}

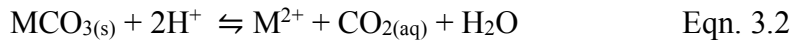
Strategies to control undesirable fluid migration are limited. The oil and gas industry has developed swelling polymers⁹⁰ and novel cementitious materials,⁹¹ but they have limited utility in some subsurface applications because either the temperatures are too high or the leaks occur too far from the wellbore to reach.^{92–94} Cements are also problematic because they are susceptible to degradation in acidic environments (like those present in CO₂ storage applications)^{95–97} because they consist largely of calcium hydroxide [Ca(OH)₂], which is soluble at low pH.⁹⁸ In addition, the high viscosity of cement limits its use to the wellbore vicinity and there, it does not often bind to metal casings or subsurface media, creating pathways that can grow over time.⁹⁴

The use of mineralization reactions could sidestep some of the limitations associated with polymers or cement-based approaches. Recent work has demonstrated the viability of using microbially-mediated calcite precipitation as a means of mitigating leakage in abandoned wells.^{99,100} Other work has proposed the injection of a mineral silicate slurry followed by CO₂ to generate solid carbonates.²⁰ The most well-studied carbonates in these contexts are magnesium- or calcium-based minerals, which react via:



where M is the divalent cation. Magnesium-based carbonates prevail in basalt formations that are of interest from a CO₂-storage perspective¹⁹ and calcium-based carbonates have faster reaction kinetics so they are common in laboratory experiments. The aqueous carbonation of wollastonite (CaSiO₃) under reservoir conditions (e.g., 90 °C, 25 MPa CO₂) produces porous, amorphous silica surrounding wollastonite cores, along with calcite, and sometimes, nanometer-scale Ca-phyllosilicates.⁶⁹ At 65 °C with ambient pressure of CO₂, Ashraf et al. reported similar products,

including Ca-modified silica gels and Ca-carbonate/silica gel composites.¹⁰¹ A common characteristic of solid carbonates is that they are sensitive to dissolution at low pH, meaning they could be an impermanent means of controlling flow:⁸⁷



In the mineral silicate system, the precipitation of these solid carbonates is dependent on the crystal structure of the parent silicates and the pH of the aqueous phase.¹⁰² In chain-silicate minerals, preferential leaching of the cation allows the precipitation of solid carbonates in the presence of $\text{CO}_{2(\text{aq})}$ and leaves a relatively unreactive porous silica network that condenses over time.⁴⁷ Our group recently reported that some mineral silicates can react with $\text{CO}_{2(\text{aq})}$ to generate non-carbonate products.¹⁰² Specifically, a ring-structured calcium silicate, pseudowollastonite (CaSiO_3) was shown to generate crystalline calcium silicate hydrates (CCSHs) in addition to Ca-carbonate when pH was increased at elevated temperature (150 °C) and moderate CO_2 concentration (0.18 M). The strained ring structure in pseudowollastonite allows for stoichiometric release of both Ca and dissolved Si, which allows for the precipitation of various non-carbonate phases. We refer to these precipitates CCSHs to distinguish them from the amorphous calcium silicate hydrate phases that form in Portland cement, which are typically referred to as CSH gels. This nomenclature is also adapted from Richardson's work that summarized and modeled the calcium silicate hydrates that exist in nature and in engineered cements.¹⁰³ The composition of phases that form in the $\text{CaO-SiO}_2\text{-(CO}_2\text{)-H}_2\text{O}$ system is complex and highly variable, depending primarily on molar ratios of dissolved species, as shown in phase diagrams and schematics in Kaprálik et al.¹⁰⁴

The goal of this work is to examine how the precipitation dynamics of carbonates and CCSHs impact fluid transport in porous media under natural or engineered conditions

representative of the deep subsurface, which are expected to vary widely. For example, in basalt-based GCS, the relatively high pH of natural waters (9-11)¹⁰⁵ may facilitate CCSH precipitation, particularly in regions where the concentration of CO₂ is relatively low (e.g., the periphery of the CO₂ plume or in leakage locations). Likewise, pore solutions in concrete applications (e.g., wellbores) are often quite basic (approaching pH 13)¹⁰⁶ and could allow the precipitation of CCSHs. In saline-aquifer-based GCS, formation waters equilibrated with CO₂ are expected to be acidic, which would promote solid carbonate precipitation, followed by re-dissolution, unless the pH can be exogenously buffered enough to promote CCSH precipitation.

In particular, this work seeks to understand how permeability evolves over time in diffusion-limited carbonated silicate systems and is impacted by the presence of acid, which is common in many subsurface environments. These objectives were studied first via a series of sand column experiments that simulate porous media, in which pseudowollastonite was injected and then reacted with CO_{2(aq)}. Pseudowollastonite was selected based on our previous study that found it can generate a variety of carbonate and CCSHs, based on aqueous conditions.¹⁰² The reacted columns were then characterized via synchrotron-based X-ray diffraction and X-ray fluorescence mapping as well as with electron microscope analyses which, together, allowed for spatial mapping of product phases under various conditions over time. Small powder batch experiments were also conducted to more fully characterize the reaction products and develop phenomenological relationships that might inform the deployment of this chemistry in the field.

3.3. Experimental Materials and Methods

3.3.1. Sand Column Experiments

Pseudowollastonite powder (average powder diameter = 10.2 μm, SD = 8.4 μm, spongy/aggregated shape) was used as received from Sigma Aldrich. NaOH (Sigma Aldrich) was

used to increase pH. Ottawa sand (500 – 841 μm fraction) was washed with 1 N HCl to remove surface impurities and rinsed with deionized water (18.2 M Ω cm, Millipore).

Sand columns, 1.59 cm in diameter and 5 cm in length, were produced by packing the washed and dried sand in 316 stainless-steel tubes that were capped at each end with stainless-steel washers and 250 μm stainless-steel mesh. After packing the tubes and oven drying, permeability and mass were measured for each column. Each was then placed in a press that held the columns in place while allowing fluid to be flowed through. Pseudowollastonite powder was suspended in deionized water (3 g/L) and injected into the columns at 10 MPa. During injection, a 20 μm porous disc was placed at the outlet end of each column to allow the passage of water and retention of pseudowollastonite. After injection, the columns were dried at 75 $^{\circ}\text{C}$ for 24 hr and permeability and mass were again measured.

The bottom end of each column was pressed into a Teflon cap to seal it while the top end remained opened and they were then submerged upright in deionized water with either 0 M NaOH or 0.1 M NaOH in a 600 mL Teflon-lined stainless-steel pressure vessel, depicted in Figure 3.1. Hereafter, columns reacted with only CO_2 are referred to as ‘ CO_2 columns’ and ones that were reacted with both CO_2 and NaOH are referred to as ‘ $\text{CO}_2 + \text{NaOH}$ columns’. The experimental

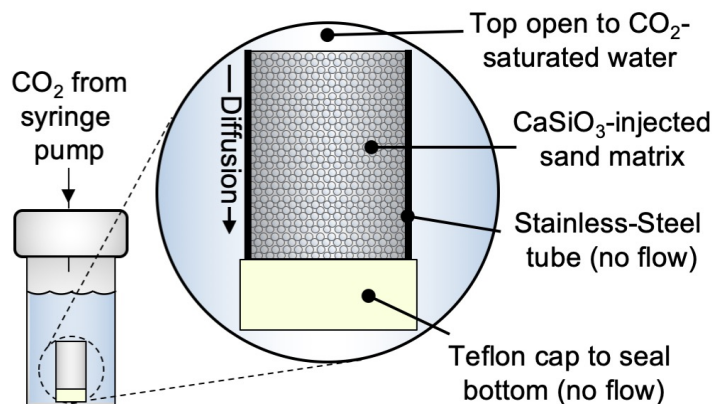


Figure 3.1. Sand columns were injected with a water-pseudowollastonite suspension and then submerged, upright, in a Teflon-lined, stainless-steel pressure vessel. CO_2 was injected into the headspace of the vessel with a syringe pump, where it equilibrated with the batch solution. CO_2 and other dissolved species could diffuse through the top (inlet) of the columns and react with the CaSiO_3 .

conditions are listed in Table 3.1. The water-CO₂ equilibrium pH was calculated with PHREEQC (V 2.18) with the PHREEQC database. The vessel was placed in an oven and heated while CO₂ (or N₂ for control columns) was injected into the headspace. We previously determined that total pressure has no observable impact on the reaction pathways in this work. Instead, the partial pressure of CO₂ plays a crucial role. The columns were reacted for various times ranging from 12-495 hr at temperatures ranging from 90-150 °C. While these temperatures are higher than those in most GCS applications, they were selected to accelerate chemical kinetics so that the experiments could be carried out over practical timescales. They were then dried at 75 °C and permeability and mass were again measured.

Table 3.1. Experimental Conditions for Column Experiments.

column number	reaction time (hr)	temperature (°C)	[NaOH] (M)	pCO ₂ (MPa)	[C] (M) [†]	batch pH [†]
1	24	90	0.1	1.1	0.22	6.16
2,3	48	90	0.1	1.1	0.22	6.16
4	96	90	0.1	1.1	0.22	6.16
5,6	168	90	0.1	1.1	0.22	6.16
7	16	150	0.1	1.1	0.19	6.65
8	24	150	0.1	1.1	0.19	6.65
9,10	48	150	0.1	1.1	0.19	6.65
11-13	96	150	0.1	1.1	0.19	6.65
14	108	150	0.1	1.1	0.19	6.65
15,16	288	150	0.1	1.1	0.19	6.65
17,18	447	150	0.1	1.1	0.19	6.65
19	495	150	0.1	1.1	0.19	6.65
20	12	150	0	1.1	0.09	3.94
21,22	48	150	0	1.1	0.09	3.94
23-26	96	150	0	1.1	0.09	3.94
27,28	168	150	0	1.1	0.09	3.94
29,30	447	150	0	1.1	0.09	3.94
31	495	150	0	1.1	0.09	3.94
32	24	150	0.1	0	0	10.49
33	96	150	0.1	0	0	10.49
34	24	150	0.1	3.4	0.38	6.16
35-41	72	150	0.1	3.4	0.38	6.16
42-47	72	150	0	3.4	0.29	3.68
48	24	150	0.1	15.5	1.35	5.52
49	24	150	0.1	3.4	0.28	3.65
50	0	N/A	N/A	N/A	N/A	N/A

[†] Initial batch pH, equilibrated with CO₂, calculated with PHREEQC

In select samples (columns 11-13, 19, 23-25, 31, and 50), the batch solutions were also doped with 15 mM strontium chloride hexahydrate, where Sr could diffuse into the columns and substitute for Ca in the precipitation of solid carbonates,¹⁰⁷ allowing for μ XRF visualization of their precipitation dynamics. The Sr substitution method was required because Si and C are unobservable via μ XRF and both the parent (CaSiO_3) and product (CaCO_3) minerals contained the same amount of Ca, rendering differentiation between the two otherwise challenging.

After the reaction periods and drying, the bottom ends of the same columns were again sealed and the columns were submerged upright in a 0.1 M NaBr solution, where the Br could diffuse into the column inlets and act as a visual complement to permeability with μ XRF mapping (since no Br existed in the system prior to this step). To understand the temporal evolution of the reactions, 96 hr and 495 hr columns were injected with epoxy and were sectioned along their length (1 mm thickness) for synchrotron μ XRF and SEM-EDS. The remaining columns were thin-sectioned (to 30 μm) and mounted to Suprasil 2A quartz glass for synchrotron μ XRD/ μ XRF.

To test the stability of the precipitates at different pH values, one set of experiments (numbers 35-47) that was reacted at 3.4 MPa CO_2 , with or without NaOH, for 72 hr were submerged in 1 M sodium acetate/acetic acid solutions⁶⁸ at pH values from 4 to 6 or in DI water and then flushed through with 20 mL DI water. They were then dried and the permeability and mass were measured.

3.3.2. Powder Batch Experiments

Small-scale powder batch experiments, were also conducted with the intention of isolating the effects of time and temperature on CCSH morphology and composition. The experimental setup for these experiments was described previously.¹⁰² Briefly, 15 mg of pseudowollastonite powder was placed in 0.75 cm^3 Teflon boats with 1 g of sand and 0.5 mL of DI water, either with

or without 0.1 M NaOH. The samples were reacted in a stainless-steel pressure vessel at 1.1 MPa CO₂ at a given experimental temperature and time. After each experiment, the samples were dried at 75 °C. One sample was dried in air at ambient temperature to compare to oven-dried samples. CCSHs were observed in the sample via SEM so we do not attribute their formation to the oven-drying process.

3.3.3. *Air Permeability Measurements*

For column experiments, permeability was determined by measuring the flow rate and pressure potential of air across the columns based on the technique of Tanikawa and Shimamoto¹⁰⁸ and is further described in Appendix 1.

3.3.4. *Materials Characterization*

Column samples were analyzed via synchrotron μ XRD and/or μ XRF at Argonne National Laboratory's Advanced Photon Source (13IDE). Further details about the beamline setup are described in Lanzirotti et al.¹⁰⁹ and in Appendix I. Spectral fitting of XRF data, XRF mapping, and local analyses of XRD data were performed in Larch.¹¹⁰

A majority of the columns were cut open after reaction (whether epoxied or not) and observed under SEM-EDS (FEI Quanta LV200). For powder batch systems, SEM-EDS was used to analyze all samples and select samples were analyzed with TEM/SAED (FEI Titan).

To analyze Si:Ca ratios for small powder batch experiments, CCSHs that formed over various reaction periods were observed under SEM by scanning across sample stubs and locating as many CCSH clusters as possible. When clusters were located, EDS spectra were acquired for individual plates and the silicon-to-calcium ratios were recorded.

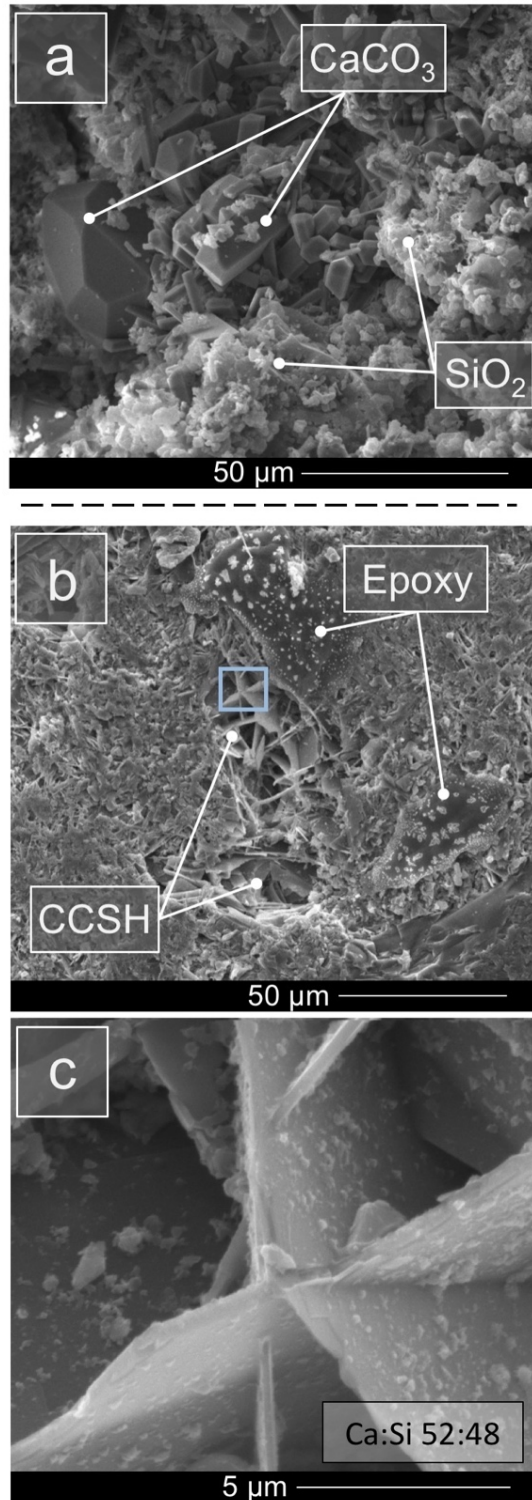


Figure 3.2. (a) Representative calcium carbonate and amorphous silica morphologies, which result from aqueous pseudowollastonite carbonation with unmodified pH (no NaOH added) at 1.1 MPa P_{CO_2} . (b,c) An example of CCSH morphology from an epoxied and sectioned column, resulting from aqueous pseudowollastonite carbonation with elevated pH (0.1 M NaOH). Sheet-like morphology was the only one observed for CCSHs in the columns.

3.4. Results

3.4.1. Precipitates and their Impact on Sand Column Permeability

Two broad classes of precipitate morphologies were observed in the experimental and control columns as shown in the SEM micrographs presented in Figure 3.2. The reaction products observed in columns injected with pseudowollastonite and reacted only in the presence of CO_2 are presented in Figure 3.2a. Under these conditions the reaction with pseudowollastonite follows Eqn. 3.1 and yields Ca-carbonate and amorphous SiO_2 , primarily. In contrast, the reaction products observed in columns reacted in the presence of $\text{CO}_2 + \text{NaOH}$ are presented in Figures 3.2b and 3.2c.

The two types of precipitates shown in Figure 3.2 had distinctly different impacts on permeability over time, as shown in Figure 3.3. While decreases in permeability were observed in all columns, there were order-of-magnitude differences for those containing carbonates alone and

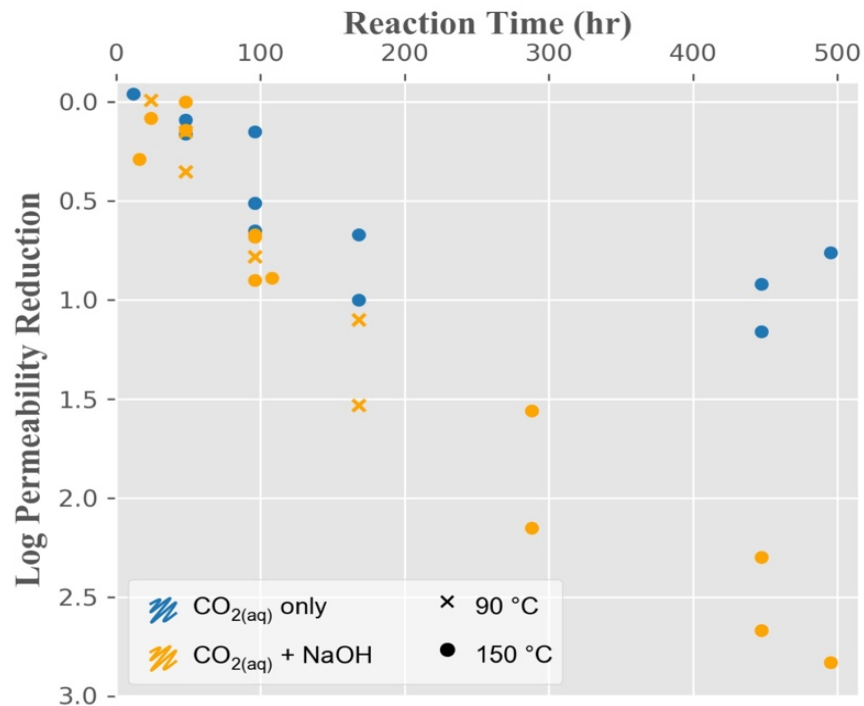


Figure 3.3. The log reduction of permeability for columns reacted in (blue) CO_2 only and (orange) $\text{CO}_2 + \text{NaOH}$ as a function of reaction time.

those containing CCSHs. The results in Figure 3.3 are plotted as a permeability reduction relative to the permeability of columns prior to reaction, which was generally on the order of 10-100 mD. Results from CO₂ columns, presented in blue, show that permeability reduction from the precipitation of carbonates was limited to a maximum 1.16 orders of magnitude (from 37 to 2.5 mD) in the 495 hr reaction time at 150 °C (columns 20-31) and permeability reduction slowed after 168 hr of reaction. In contrast, the CO₂ + NaOH columns (presented in orange, columns 7-19) exhibited continuously decreasing permeability, with a maximum reduction of 2.83 orders of magnitude (from 163 to 0.24 mD) after 495 hr of exposure. CO₂ + NaOH columns that were reacted at 90 °C (to determine whether CCSHs could form and impact permeability at a range of temperatures, columns 1-6) follow a similar trend in permeability. For example, at 96 hr, the 90 °C column experienced a decrease in permeability of 0.78 orders of magnitude while the 150 °C columns experienced an average 0.75 orders of magnitude decrease. In control columns (32 and 33), where N₂ was used instead of CO₂, there was nearly no change in permeability (in fact, a slight increase from 69 to 99 mD at 96 hr of reaction) and there were no observed reaction products.

3.4.2. μ XRF Mapping of Precipitation and Diffusivity

Synchrotron μ XRF maps of columns 31 (CO₂), 19 (CO₂ + NaOH), and 50 (unreacted control) are presented in Figure 3.4. Each map was collected from the column's inlet (top) to a depth of 8 mm, over a width of 1.5 mm. Strontium substituted for Ca in aragonite, as expected, which was the principle carbonate that precipitated under these conditions (from μ XRD analyses).

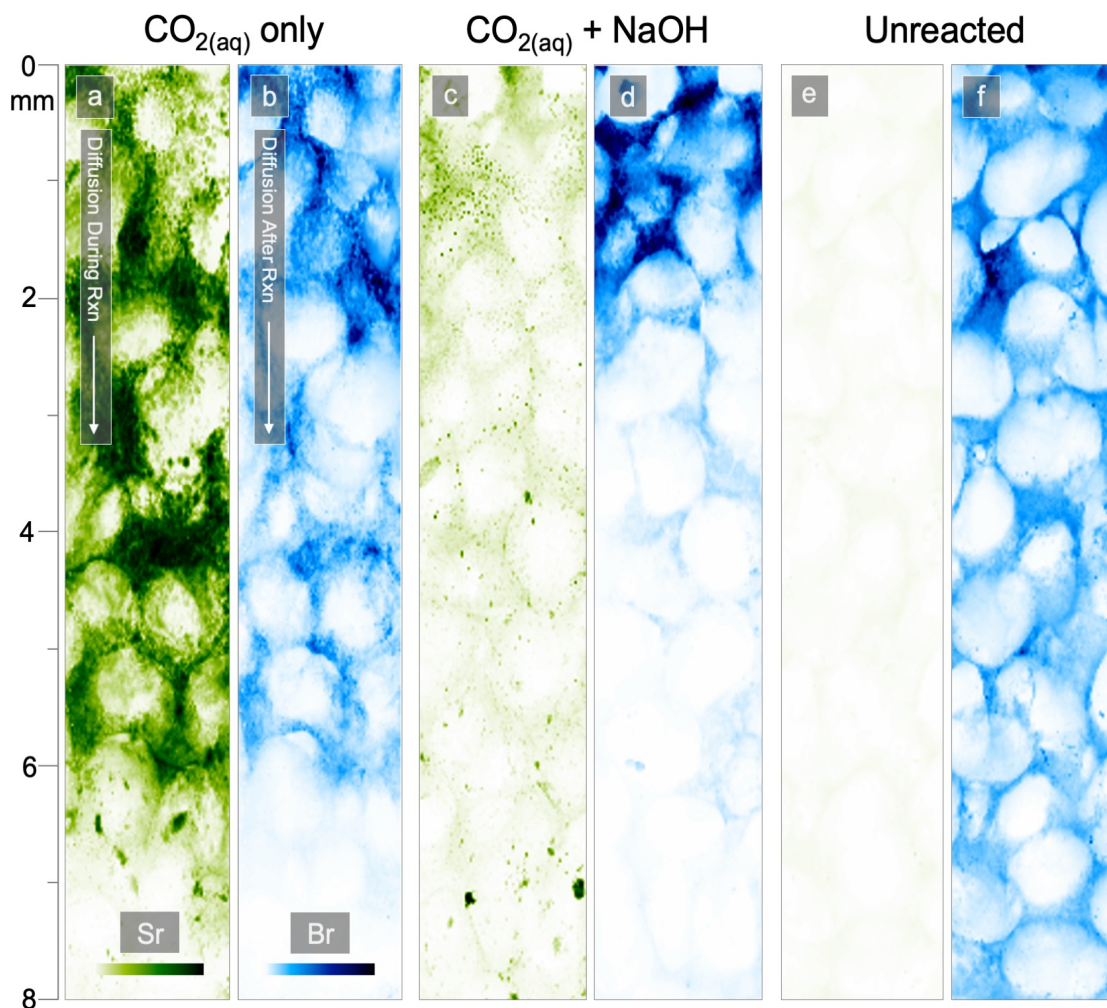


Figure 3.4. Micro-XRF maps of (green) Sr and (blue) Br for the inlet 8 mm of columns reacted for 495 hr in (a,b) CO_2 only and (c,d) $\text{CO}_2 + \text{NaOH}$ compared to (e,f) an unreacted column. Dissolved Sr was present during the reaction period and appeared to coprecipitate with Ca in Ca-carbonate. Columns were submerged, upright, in a Br solution after the reaction period to visualize diffusivity of the columns, as a complement to permeability measurements. Each Sr map shares a common color scale. Likewise, each Br map shares a common color scale. The intensities shown in these maps are proportional to element concentrations.

In contrast, Sr did not substitute to a large extent in the CSHs so the green Sr maps in Figure 3.4 show the differences in carbonate precipitation between the columns.

In the CO_2 column, an abundance of Sr was observed in the first 7 mm (Figure 3.4a), indicating a large quantity of solid carbonate precipitation. The Br maps illustrate the relative diffusivity of water into the columns following the reaction period. The Br front (Figure 3.4b) nearly mirrored the Sr front, confirming that precipitates play an important role in controlling

permeability. The permeability of the CO₂ column decreased from 87 mD to 15 mD during the reaction period. In contrast, the maps of the CO₂ + NaOH column show Sr at relatively lower concentrations than in the CO₂ column, indicating less precipitation of solid carbonates (Figure 3.4c) and bromine (Figure 3.4d) was generally limited to the first 2-3 mm of the column but at high concentrations relative to the inlet of the CO₂ column. The permeability of the column decreased from 163 mD to 0.24 mD during the reaction period. It should also be noted that even though the columns were approximately 50 mm in length, the vast majority of precipitation and physical change occurred within the first ~5-8 mm at 495 hr. Permeability measurements assume a homogeneous medium throughout the entire length of the column and assuming the change in permeability is due primarily to the reacted regions, the permeabilities of the reacted zones are likely significantly lower than reported. The final column shown in Figure 3.4 is a control that was unreacted (and therefore never exposed to Sr) so μ XRF mapping shows no observable quantities of Sr (Figure 3.4e) and the bromine front exceeded 8 mm (Figure 3.4f). The permeability of that column was 141 mD.

3.4.3. Precipitation Locations Within Pores

Micro-XRF and SEM-EDS analyses of thin-sectioned columns suggest that the mechanisms that drive the reductions in permeability in the CO₂ and the CO₂ + NaOH columns are observably different. In the CO₂ columns, solid carbonates precipitated randomly, without any preferred location within a given pore (e.g., in the pore body, along sand grain surfaces, or in pore throats; Figure 3.5a), which was expected from previous work in carbonate precipitation.¹¹¹ In contrast, the CSHs that formed in the CO₂ + NaOH columns tended to form preferentially along the edges of sand grains, including in pore throats, which left a considerable amount of the pore body relatively open. A representative cross-section of a pore is shown in Figure 3.5b where the

dark region, filled with epoxy, indicates a large open pore body (also evident from μ XRF in Figure 3.4d). EDS maps of the region (Figure 3.5c,d) show that the CCSHs are Si-rich but also contain Ca. The tendency for these CCSHs to nucleate and grow on sand grain surfaces, including where grains are close to one another, indicates that pore throats are filled relatively quickly, potentially leading to dramatic decreases in permeability.

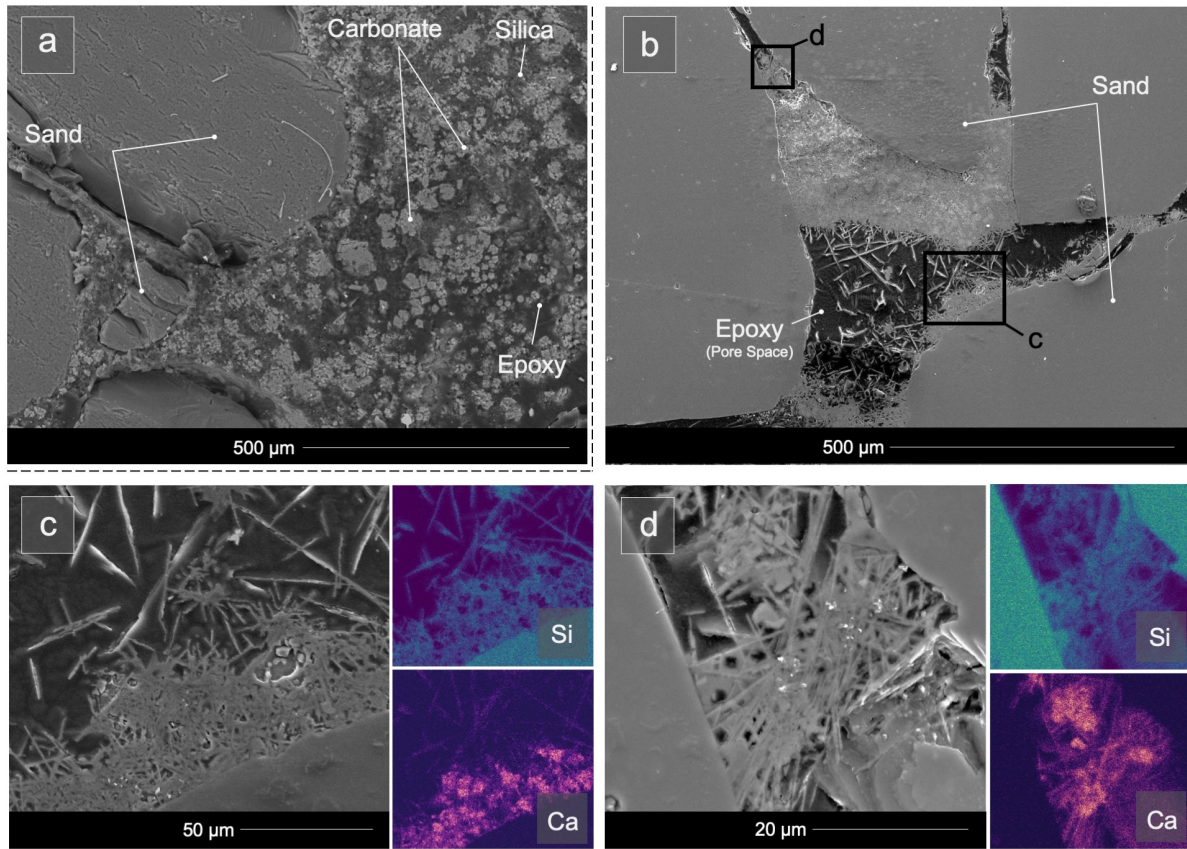


Figure 3.5. (a) SEM micrograph of a representative pore in a CO₂ column, where Ca-carbonate and amorphous silica precipitated throughout the pore body indiscriminately. (b) Compared to SEM cross-section of a representative pore in CO₂ + NaOH columns, showing a relatively open pore body but dense CCSH precipitation along sand grain edges and in the pore throats. (c,d) Inset EDS maps show that CCSHs in this pore appear to contain both calcium and silicon.

3.4.4. Temporal Evolution of Reaction Fronts

The reaction fronts in the CO₂ and CO₂ + NaOH columns evolved differently over time. After reacting for 96 hr, the carbonation front in CO₂ columns penetrated approximately 3 mm into the column and was uniformly distributed across the inlet of the column (Figure 3.6a). Bromine was abundant and exceeded 8mm, indicating that water was able to diffuse through this column (the first 5 mm are shown in Figure 3.6b while a 16 mm Br map is shown in Appendix I). After reaction for 495 hr, the Sr front advanced to nearly 8 mm but was non-uniformly distributed normal to the direction of diffusion (Figure 3.6c). In some areas near the inlet, both Sr and Ca concentrations (Ca not shown) were low, suggesting that the carbonate that precipitated in this region dissolved in accordance with Eqn. 3.2, leaving large, open spaces (see Appendix I) allowing

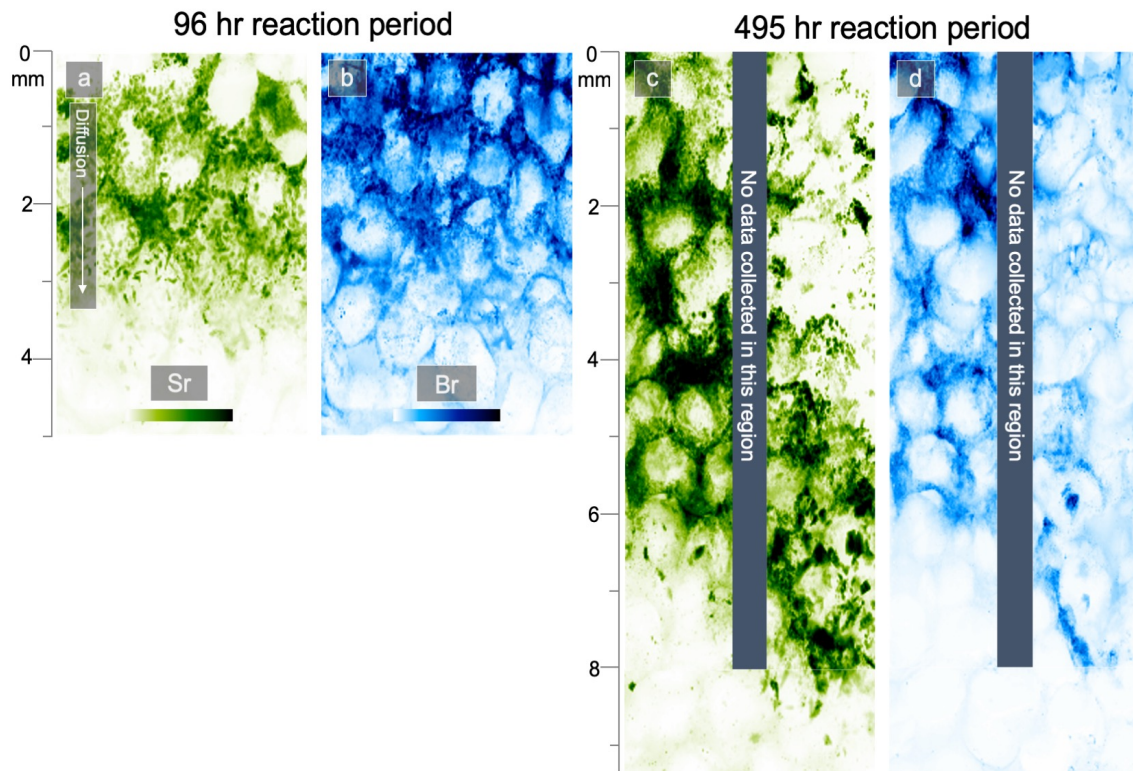


Figure 3.6. (a) Br and (b) Sr μ XRF maps of 96 hr CO₂ column experiments show a uniform carbonation front normal to the direction of diffusion. In contrast, at 495 hr of reaction, the (c) Br and (d) Sr μ XRF maps show a reaction front that is non-uniform and indicates redissolution of solid carbonates near the inlet of the column.

Br to diffuse to a depth >8 mm (Figure 3.6d). The carbonate redissolution could explain why the permeability in the CO₂ columns did not continue to decrease over longer durations.

In contrast, the reaction front of CO₂ + NaOH columns never exceeded ~3 mm, regardless of reaction time. This could explain why the permeability in these columns continued to drop over time. SEM analyses suggest that the large re-dissolved regions did not exist in the CO₂ + NaOH columns.

3.4.5. Effects of Ion Concentrations on Precipitation Products and Permeability

To explore the effect of CO₂ on CSH formation in columns, the partial pressure of CO₂ was varied in several experiments. When the P_{CO₂} was increased to 3.4 MPa for 24 hr (column 34, 0.1M NaOH), an abundance of CSHs and Ca-carbonate were observed near the inlet of the column. The permeability of the column decreased by 1.02 orders of magnitude (47.8 to 4.6 mD) during reaction. At higher partial pressures of CO₂ (15.5 MPa, 24 hr, column 48), the permeability after reaction was too low to measure in the laboratory, suggesting at least three orders of magnitude reduction (from 42.5 mD). Evaluation of the columns following reaction revealed that abundant CSH and Ca-carbonate precipitates had formed in the first several mm of the column (see Appendix I).

These results suggest that the formation of CSHs is pH dependent, which is consistent with studies of CSH gel in concrete. Interestingly, a few columns reacted without NaOH, at 3.4 MPa CO₂ for 72 hr (numbers 42-47), also yielded some CSHs, although at a much lower concentration than in columns containing NaOH. This result was unexpected, because we had not previously observed CSH formation without NaOH present. Because of this result, we postulate that the concentration of dissolved carbon plays an important role in CSH precipitation. Modeling (PHREEQC) suggests that in the 1.1 MPa experiments, the addition of NaOH increases

the total dissolved carbon concentration in the batch solution from 0.09 to 0.19 M. In the 3.4 MPa experiments, the dissolved carbon concentration is already high in both conditions due to the high pressure of CO₂ (0.38 and 0.29 M carbon, with and without NaOH, respectively). To ensure that the role of NaOH in this reaction mechanism was driven by the acid/base properties of OH⁻ and not Na⁺ (since cations in solution have been shown to affect CO₂-induced dissolution of minerals),¹¹² one additional column (number 49) was reacted with 3.4 MPa CO₂ and 0.1 M NaCl rather than NaOH. The only products that were observed were Ca-carbonate and silica. In analogous work in Mg carbonation, NaCl increased carbonate precipitation by increasing the Mg²⁺ dissolution rate, so the lack of CCSHs in this column could be due to that effect¹¹³ or impacts from ionic strength but our previous experiments have shown that NaCl does not have a notable impact on CCSH formation when NaOH is present.

3.4.6. Stability of Reacted Columns Under Acidic Conditions

To evaluate the long-term stability of these precipitated CCSHs, the permeability of two column types was evaluated following reaction for 72 hr at a CO₂ pressure of 3.4 MPa (columns 35-47). The permeability of each sample was measured after a 16 hr acid treatment in acetic acid/sodium acetate solutions⁶⁸ ranging from pH 4 to 6 (and a DI water control). As shown in Figure 3.7, in the CO₂ + NaOH columns, the permeability remained nearly constant after acid treatment, while in the CO₂ columns, permeability increased and approached the pre-reaction

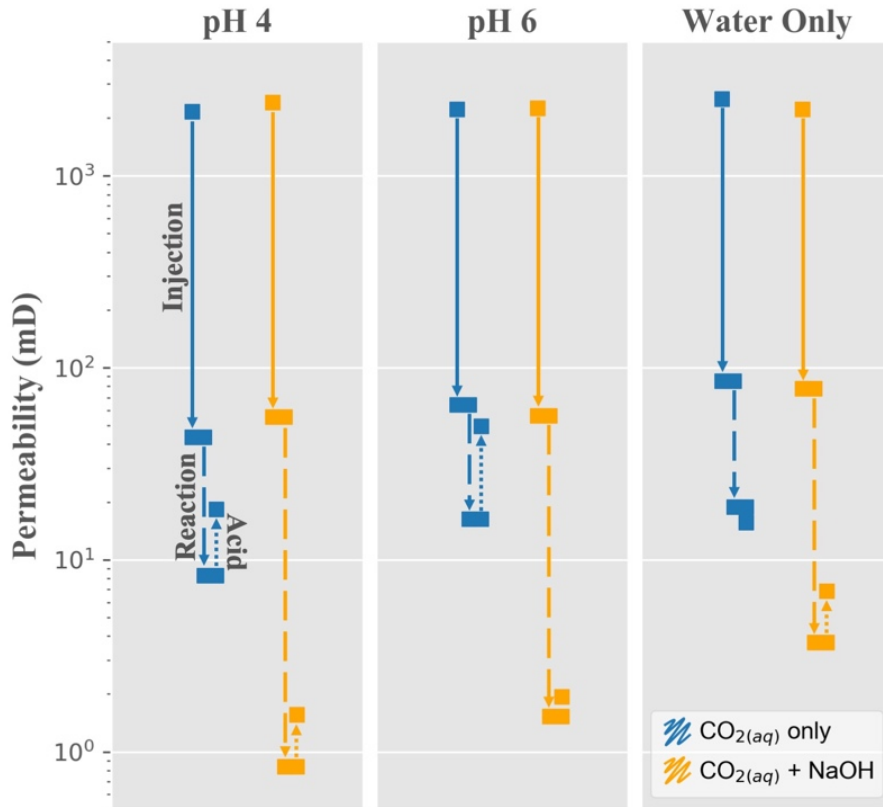


Figure 3.7. Permeabilities of (blue) CO_2 only columns and (orange) $\text{CO}_2 + \text{NaOH}$ columns prior to CaSiO_3 injection, after injection, after the 72 hr reaction period, and after 16 hr acid diffusion at (top) pH 4 and (center) pH 6, and with only DI water diffusion (bottom).

permeabilities. The pH 4.5 columns and the DI water columns were sectioned and observed under SEM, where it was apparent that CCSHs remained intact at approximately the same quantity (based on SEM observation) regardless of acid treatment while the Ca-carbonate in the pH 4.5 columns had largely been dissolved compared to the water control column (shown in Appendix I).

3.4.7. Effects of Temperature on CCSH Precipitation

In our previously-reported mechanism for precipitation of CCSHs, local concentrations of Ca and Si ions governed the stoichiometric ratios in the precipitates. In that case, a wide range of Ca and Si concentrations might be expected in the CCSHs because local ion concentrations are expected to vary considerably due to dissolution, precipitation, temperature, and chemical and pressure gradient effects. To extend that mechanism and study these reaction products, additional

powder batch experiments were performed to better understand the effects that time and temperature have on these precipitates in the absence of the mass-transfer and heterogeneity effects that may exist in column experiments.

The first condition that was tested was the effect of temperature on CCSH formation. Experiments with 0.1 M NaOH and 1.1 MPa CO₂ were conducted for 24 hr at 75, 90, 110, and 150 °C. At 75 and 90 °C (see Appendix I), Ca-carbonate precipitates predominated and even though CCSHs were present, they were small. At 110 °C, CCSHs were abundant and there were no obvious differences from the 150 °C samples.

3.4.8. Effect of Time on CCSH Composition

An additional set of batch experiments at 150 °C was conducted for 24, 72, and 168 hr to investigate the effect of time on CCSH composition. We did not observe a trend in Si:Ca ratios of the precipitated phases (Figure 3.8). It is clear that over the time scales tested here, a wide variety of mineral compositions are present within these CCSHs, from Si-rich to Ca-rich.

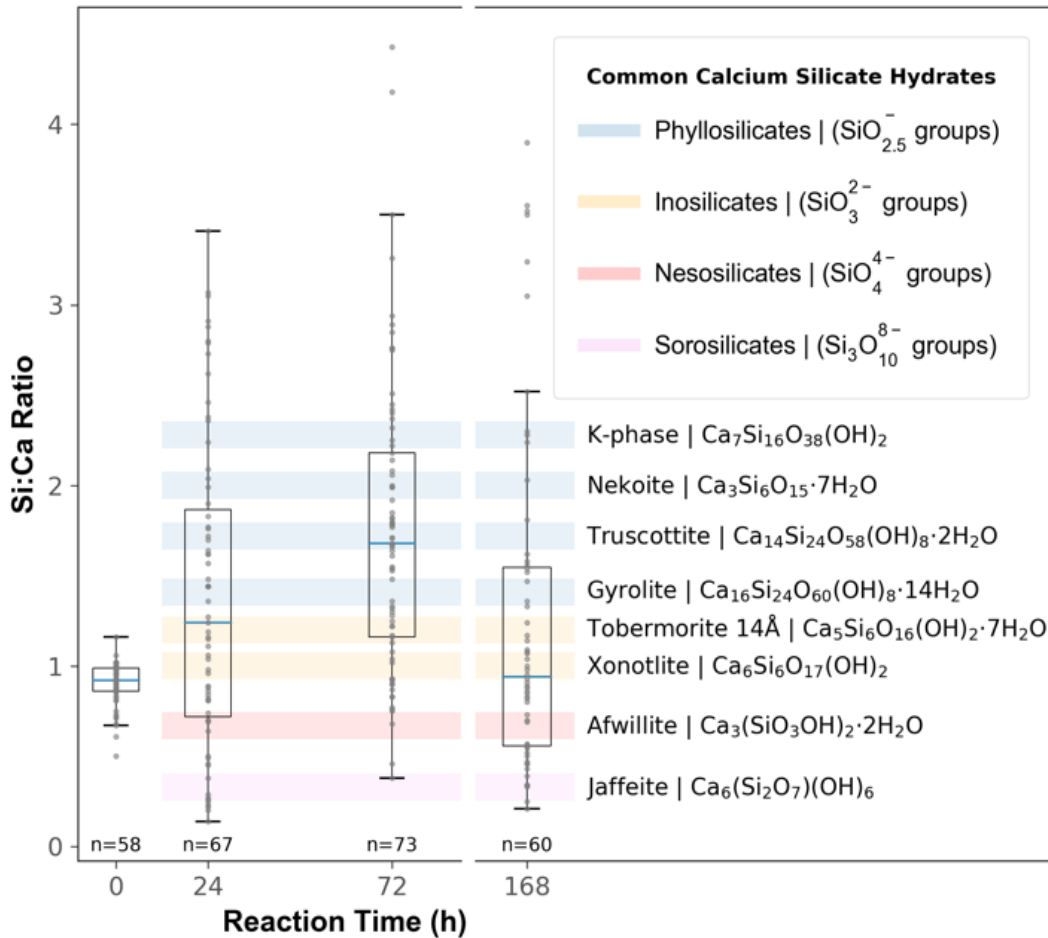


Figure 3.8. Silicon to Ca ratios of CCSH phases from powder batch experiments reacted in 0.1 M NaOH + 0.19 M CO₂ for 24, 72, and 168 hr. The ratio for unreacted pseudowollastonite is also shown at 0 hr. The Si:Ca ratios vary widely at all time periods and do not clearly seem to approach any particular ratio.

TEM-SAED analyses from 24 and 168 hr experiments confirmed that the CCSHs were crystalline (i.e., bright diffraction spots) but each sample had a unique diffraction pattern and we were unable to definitively match any to known materials (see Appendix I). Approximately 90° symmetries were observed so only CCSHs that have at least partially orthogonal geometries are presented in Figure 3.8.

3.5. Environmental Implications

The results presented here could enable new methods for controlling fluid flow in the subsurface. From a phenomenological perspective, the carbonation of calcium silicates that

produce CCSHs effectively reduces the permeability of porous media to a greater extent than calcium silicates that produce only carbonates. From a mechanistic standpoint, we present evidence that the formation of these CCSHs is somewhat sensitive to pH but will form over a range of time, temperature, and P_{CO_2} conditions. Taken together, these results inform an understanding needed to deploy this chemistry in the field, which may involve injecting mineral silicates in a pH-controlled slurry or tailoring the chemistry of injected fluids into formations.

The deliberate formation of CCSHs is an attractive means for blocking flow for a number of reasons. The apparent tendency for the CCSHs to precipitate on interfaces and in pore throats suggests that the reaction pathways identified here could be an efficient way to block flow in porous media. The stability of CCSHs relative to carbonates when exposed to acidic solutions suggests that CCSHs may be more effective at long-term stabilization and permeability control in geoengineering applications.

Naturally, there will be challenges associated with using CCSHs to block flow in the subsurface. Understanding and, in some cases, engineering appropriate aqueous chemistry in complex and heterogeneous formations will require substantial efforts in field-scale observation and modeling. In some settings, such as EGS, CCSH-producing silicates might be injected. In other applications, such as GCS in basalts, having a detailed understanding of this chemistry could help explain fluid migration in some cases.

Finally, a number of aspects of CCSH formation are still poorly understood. For example, the role of CO_2 in these reactions has not yet been fully characterized. The formation of CCSHs does not appear to proceed without CO_2 yet none of the phases we have observed match known

carbonate-containing calcium silicates, so future work could assess the specific role that CO₂ is playing in these reactions.**

3.6. Chapter 3 Acknowledgements

Support for this work came from the United States Department of Energy National Energy Technology Laboratory (Grant DE-FE0026582) and the U.S. National Science Foundation (to AFC) (CBET-1134397 and CBET-1805075). Portions of this work were performed at GeoSoilEnviroCARS (The University of Chicago, Sector 13), Advanced Photon Source (APS), Argonne National Laboratory. GeoSoilEnviroCARS is supported by the National Science Foundation - Earth Sciences (EAR - 1634415) and Department of Energy- GeoSciences (DE-FG02-94ER14466). This research used resources of the Advanced Photon Source, a U.S. Department of Energy (DOE) Office of Science User Facility operated for the DOE Office of Science by Argonne National Laboratory under Contract No. DE-AC02-06CH11357.

** Supporting information is available for this chapter. This information is available free of charge via the Internet at <http://pubs.acs.org> and at the end of this document.

Chapter 4. Formation of Low-Carbon Crystalline Cement via Calcium Silicate Carbonation

4.1. Chapter Summary

Cement is the most consumed man-made material in the world. Here we report on a new method for synthesizing crystalline calcium silicate hydrate (CCSH) phases, which are more similar in chemical composition to ancient Roman cements than to modern ordinary Portland cement (OPC), with low energy and carbon emissions. The materials were made by curing silicate feedstocks, with equimolar ratios of calcium and silica, under elevated partial pressures of CO₂ in buffered aqueous solutions. CCSH mortars cured for seven days achieved compressive strength of 13.9 MPa, which is comparable to the 28-day strength of Type-S OPC mortar. Bromide diffusivity tests, used as an indicator of durability of the materials, show that CCSH mortars have significantly lower diffusivity than OPC. The resistance to dissolution at low pH of the materials was measured using acid exposure tests and found that CCSH mortar lost 3.1% of its mass compared to 12.1% in OPC. Total carbon measurements showed that these materials can sequester between 169 and 338 g of CO₂ per kg of cement, compared to negligible CO₂ uptake during the hydration of OPC. A lifecycle analysis of CCSH cement production suggests that these materials could be produced at an industrially-relevant scale with a fraction of the energy and carbon emissions of OPC.*

* This work was prepared and styled for submission to *Nature Sustainability*, in collaboration with Elizabeth J. Opila, Rouzbeh Shahsavari, and Andres F. Clarens

4.2. Introduction

Decarbonizing the global economy to address climate change will require dramatic changes to our energy, transportation and industrial infrastructure. While some of these transitions, e.g., electrifying transportation, seem increasingly achievable, others, e.g., decarbonizing industrial production, remain elusive.¹¹⁴ Of all the industries that are difficult to decarbonize, iron/steel and cement manufacturing stand out as the two largest global emitters of greenhouse gas emissions (Figure 4.1).¹¹⁴⁻¹¹⁶ Cement is particularly problematic because its demand is growing roughly twice as fast as global steel production and its importance in infrastructure makes it the most produced material in the world. Over 4.1 billion metric tonnes of Portland cement were produced in 2018 contributing between 5-10% of global CO₂ emissions.^{3,4,117,118} Most of this production is occurring in developing countries like China, which produced more cement between 2017 and 2018 than the United States did in the entire 20th century.¹ Meeting mid-century goals for global carbon emissions reductions will require new ways to synthesize cementitious materials that have the combination of cost, scale, and performance of cement.

Ordinary Portland cement (OPC), the most common form of cement used worldwide, is carbon intensive for two principal reasons. First, OPC is generally produced by heating limestone, predominantly comprised of calcium carbonate (CaCO₃), to produce CaO, via:



This calcination reaction produces approximately 550 kg of CO₂ per tonne of cement.¹¹⁹ Second, the CaO is subsequently heated to between 1400-1500 °C with sources of silica and alumina (generally clay, shale, and sand) at (3:1) and (2:1) ratios to produce clinker (consisting predominantly of calcium silicates such as Ca₃SiO₅ and Ca₂SiO₄), the raw form of OPC. Heating

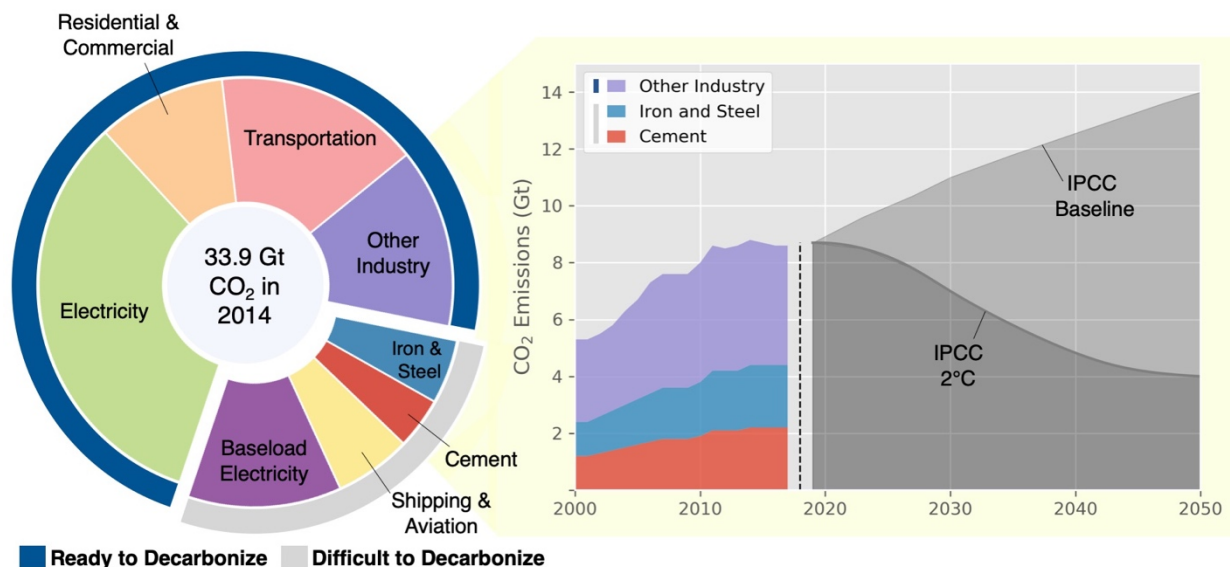


Figure 4.1. The global economy includes some sectors that are ready to decarbonize and some that are more challenging to decarbonize. Of those more recalcitrant sectors, cement production is particularly challenging both because its use is accelerating worldwide and low-carbon alternatives have yet to be proposed.

the feedstock to these high temperatures requires large amounts of energy and the industry uses predominantly coal (69%), oil (17%), and natural gas (9%).¹²⁰ Reliance on these fossil sources of energy is carbon intensive and it has been estimated that the heating related emissions from OPC production are between 267 and 534 kg CO₂/tonne cement.^{119,121}

The chemistry of OPC is complex and varied but is generally related to its calcium:silicon ratio and the three-dimensional structure of calcium silicate hydrates (CSH) that emerges when the material is hydrated.¹²² Even though most of the demand for cement is in pour-in-place applications, the fastest growing sub-sector in the cement market is for pre-cast structures that are manufactured under highly controlled conditions and delivered to construction sites ready for assembly. This precast market currently comprises approximately 12% of the market for OPC in the United States.² Precast elements are desirable because curing conditions can be carefully controlled and the lifespan of the material can be extended.¹²³ Cements often degrade when dissolved cations (e.g., magnesium, sulfate, carbonate) attack calcium hydroxide and CSH gels.¹²⁴

The precipitates from these reactions (e.g., ettringite, brucite, aragonite) are often insoluble but they can adsorb water, which can cause swelling from within the bulk of the material, generating internal pressure, cracking the concrete.¹²⁵ The failure of concrete continues as fractures develop between the cement binder and the sand or aggregate. As these microcracks form, there is little to stop their propagation, enabling infiltration of water and freeze-thaw cycles that further degrade the integrity of the material. In reinforced structures, these fractures allow water, often containing salt, to reach metal reinforcements leading to corrosion, opening even more fractures and negating the tensile strength of the concrete, allowing further degradation to occur.

Efforts to develop cements with improved durability have generally focused on additives that reduce the permeability of the material since corrosion typically occurs via solute penetration and attack.¹²⁶ Efforts to reduce the environmental impact of cements have generally sought to blend pozzolanic waste materials, e.g., fly ash, slag, with cement to avoid some of the manufacturing burdens of making ordinary Portland cement. Ongoing work seeks to create cement from non-hydraulic calcium silicates (wollastonite, CaSiO_3) that react with CO_2 to produce CaCO_3 and SiO_2 .¹²⁷ These cements sequester a significant amount of CO_2 during curing but may not outperform ordinary Portland cement in terms of lifetime, particularly under mildly acidic conditions. Centuries ago, Roman engineers generated famously-durable hydraulic cements with a low Ca/Si ratio, which yielded plate-like crystalline silicate hydrate mineral phases such as tobermorite and phillipsite, among others.⁴⁰ Roman cements rely on raw materials that are not common outside of volcanically active regions and are therefore difficult to scale⁴² but they provide inspiration for the long-lasting performance that is achievable in concrete.

Here we report on a new method to synthesize crystalline calcium silicate hydrate (CCSH) phases, similar to those in Roman cements while also utilizing and storing CO_2 . The reactions that

lead to these phases are sensitive to calcium/silica ratio in the dissolved aqueous phase as well as pH and partial pressure of CO₂. This work sought to test three hypotheses related to the feasibility of using these materials in infrastructure applications. The first is that these materials have mechanical properties that are comparable to conventional ordinary Portland cement because of the cementitious behavior of the crystalline precipitates. The second is that these materials have lower permeability due to the transecting manner in which the precipitates form and thus higher durability than conventional OPC. The third is that these materials would have a significantly lower carbon footprint than OPC and could be an enabling chemistry for decarbonizing the cement industry.

4.3. Results

4.3.1. Compressive Strength and Carbon Utilization of Various Cement Types

Ordinary Portland cement derives its strength from the hydration of tricalcium and dicalcium silicates (i.e., alite and belite) that forms amorphous calcium silicate hydrate (CSH) gels, shown in Figure 4.2a. The CSH gels form around aggregate (sand grains in the case of mortar), binding the materials together and increase in strength over the course of weeks.

Figure 4.2b shows how distinct CCSH phases synthesized in this work are from the CSH phases in OPC. In our experiments, pseudowollastonite (CaSiO₃), a calcium silicate that produces equimolar concentrations of calcium and silica when it dissolves in water, was reacted with CO₂ at elevated pH to produce interlocked platy crystalline phases. In previous work,¹⁰² we have shown that this stoichiometric dissolution mechanism distinguishes pseudowollastonite from wollastonite and that an exogenous increase in pH is crucial for generating CCSH phases that are reminiscent of those credited with providing the strength and durability to Roman concrete^{16,54} along with calcium carbonate and silica, as generalized in the equation in Figure 4.2b. The CCSH phases

presented here tend to precipitate on solid-fluid interfaces (i.e., on sand grains) and form a lattice-like structure that is low permeability, compared to calcium carbonate precipitation, which occurs under the same conditions when pH is not buffered (shown in Figure 4.2c).¹²⁸ While it is clear from our previous work that the CSH phases are cementitious, this sections seeks to quantify the macroscale strength of mortar made from them and compare the strength to carbonate-based mortar and standards for OPC.

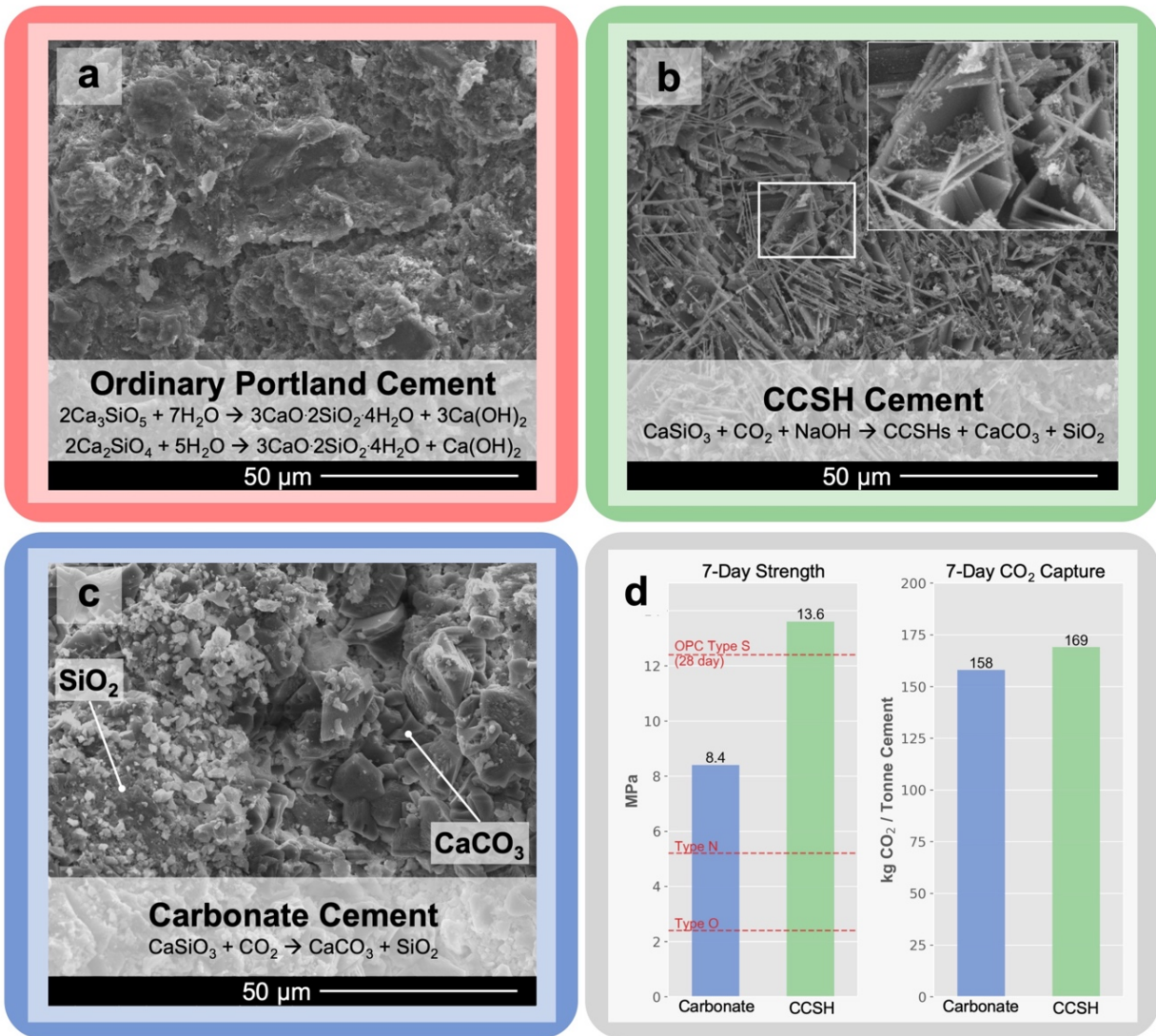


Figure 4.2. Macro- and micro-scale differences between (a) ordinary Portland cement mortar, (b) CESH cement mortar, and (c) carbonate cement mortar. (d) The compressive strength of 28-day OPC formulations (based on ASTM C270) are shown relative to 7-day compressive strengths of the alternative cements, along with 7-day CO₂ uptake measurements

A Taguchi design of experiments¹²⁹ was employed to optimize certain curing conditions and mix ratios for 2-in mortar cubes to serve as a proof-of-concept that these precipitates could serve as alternative cement materials. The design is further described in the methods and in Appendix II. In short, we investigated the impacts of buffered pH in the water used to mix the specimens, the pressure of CO₂ during an initial 3-day setting phase in a CO₂ gas atmosphere, and the temperature, pH, and pCO₂ during a subsequent 4-day wet curing phase where the specimens were submerged in buffered water in a pressure vessel with CO₂ in the headspace.

Mortar specimens were tested in triplicate following the ASTM C109¹³⁰ procedure in order to compare compressive strength with OPC standard strengths of unit masonry from ASTM C270,¹³¹ presented as red lines in Figure 4.2d. Our experiments concluded that CCSH mortar achieved compressive strengths as high as 13.6 MPa in 7 days of curing when the initial mix water pH (equilibrated with CO₂ in the headspace of the pressure vessel) was increased to 6.5, the pressure of CO₂ was 0.55 MPa, the pH of the 4-day curing water (equilibrated with headspace CO₂) was increased to 6.5 with 0.76 MPa CO₂ at 140 °C. The analysis of variance of this Taguchi design indicated that the pH of the initial mix water, the pressure of CO₂ in the initial setting phase, and the temperature during the wet curing phase had the largest impacts on compressive strength. To test the strength of carbonate-mortar, similar specimens without any pH adjustment were tested in parallel and were found to have a compressive strength of 8.4 MPa, indicated in Figure 4.2d.

The carbon content of the optimal CCSH-mortars and the carbonate-mortar were measured by sampling fractured pieces from the compression tests. We found that, in the optimized CCSH mortar, an average of 1.23% (mass) was carbon, which indicates that 169 kg of CO₂ per tonne of pseudowollastonite cement could be captured and utilized during the curing phase. For two specimens that were cured for 28 days, that percent increased to 2.46%, or 338 kg CO₂ per tonne

of cement. The carbon uptake in 7-day carbonate mortar was 1.15%, indicating utilization of 158 kg CO₂ per tonne of cement and the percent increased to 1.93% (265 kg CO₂ per tonne) in 28 days. While there is some calcium carbonate present in the CCSH mortar, the fact that its carbon uptake was greater than that of the carbonate mortar could be indicative of the CCSH phases incorporating carbon as phases such as scawtite [Ca₇(Si₃O₉)₂CO₃·2H₂O] or spurrite [Ca₅(SiO₄)₂(CO₃)], in addition to non-carbon-containing phases similar to tobermorite. In previous work, we demonstrated that the CCSH phases that formed under similar conditions were of mixed composition, with a range of calcium-to-silicon ratios (median of approximately 1) and a variety of crystal lattice parameters.¹²⁸

4.3.2. Comparisons of Durability

Cement durability is often reported in terms of solute diffusivity into the bulk material because interactions between the cement (or steel reinforcement) and dissolved ions is the principal failure mode in many applications.¹³² To evaluate the diffusivity of ions into our experimental and control samples, mortar samples were produced and submerged in a 0.1 M NaBr solution. Chlorine is often used for this purpose in the cement literature but in order to visualize the ion diffusion using synchrotron-based fluorescence, we used bromine, which behaves like chlorine but is much more easily detected. The results shown in Figure 4.3 show that over a relative short 6-hr exposure to the NaBr solution, the bromine penetrated much further into the OPC sample (Figure 4.3a) than it did into the CCSH sample (Figure 4.3b). These results are consistent with air permeability measurements (results previously reported) which show order-of-magnitude differences between CCSH materials and an alternative cement.¹²⁸

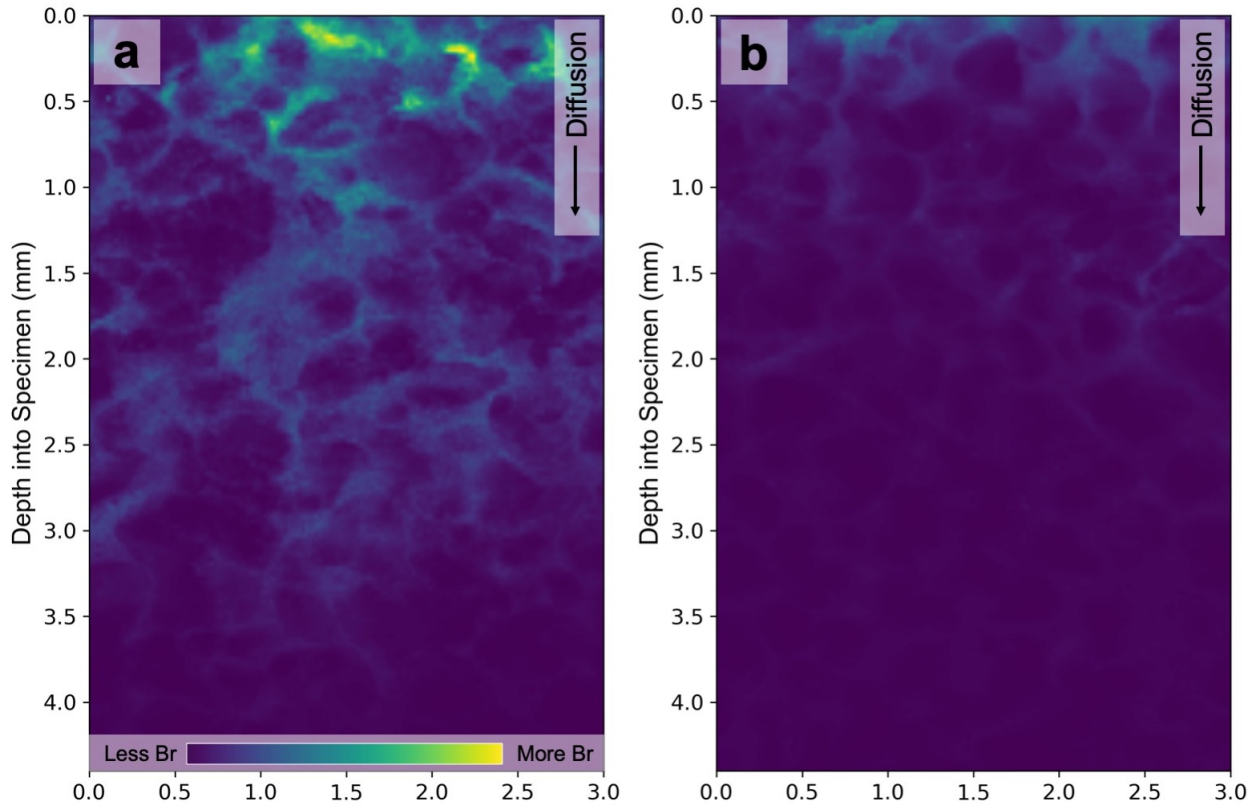


Figure 4.3. Diffusion of a Br tracer into (a) a 7-day OPC mortar specimen and (b) a 3-day CCSH cement mortar specimen. The top of both maps align with the outer edge of the specimens and color map is shared, allowing a comparison of relative Br concentrations.

The performance of cement is also sometimes evaluated in terms of its reactivity under acidic conditions, which are common in the environment and which can lead to deterioration and premature failure. To evaluate the efficacy of CCSH cements relative to OPC and carbonate alternatives, mortar cubes (2 OPC, CCSH, and carbonate cubes, each) were submerged in aqueous solutions with a pH of 5 (acetic acid and sodium acetate) were aged for 7 days. There were clear visual differences between the samples as shown in Figure 4.4. Both the OPC specimens and the carbonate-mortar specimens (Figures 4.4a and 4.4b, respectively) exhibited significant deterioration around the edges. The OPC specimens also experienced discoloration that was clearly visible in cross sections (Figure 4.4a inset). In contrast, the CCSH specimens (Figure 4.4c) largely remained intact under identical conditions. The mass of all specimens was recorded before and after aging. The OPC and carbonate specimens respectively lost 12.1 and 14.7% of their mass. In

contrast, the CCSH specimens lost 3.1%. This difference in reactivity suggests that CCSH-based cements could be well-suited for relatively aggressive applications and/or would provide a more permanent form of CO₂ storage than other cement types that might dissociate even under modestly low pH conditions.

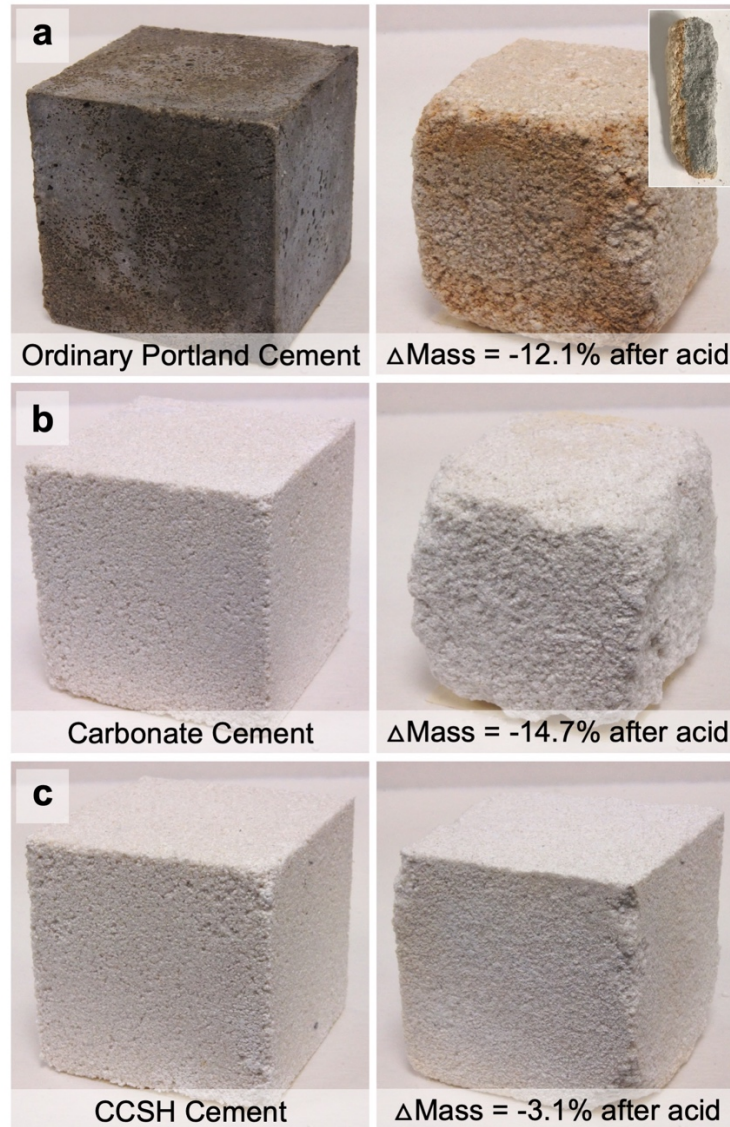


Figure 4.4. Mortar cubes made with (a) ordinary Portland cement, (b) carbonate-based cement, and (c) CCSH-based cement were aged for 7 days in an acidic solution (pH = 5). The visible corrosion and change in mass reveal the extent to which CCSH phases are resistant to acid attack when compared to the alternatives presented in this work.

4.3.3. Lifecycle Analysis of CCSH Cement

Lifecycle analysis was used to quantify the carbon emissions profiles of CCSH materials relative to conventional OPC. The results, presented in Figure 4.5, show CO₂ emissions to manufacture both one tonne of concrete (assuming 14% cement by mass) and one tonne of cement. The results suggest that three lifecycle phases in particular – the limestone feedstock required (calcination emissions), pyroprocessing (fuel emissions), and CO₂-uptake during curing – contribute most of the emissions savings observed for CCSH cements when compared to OPC.

During the calcination process for one tonne of OPC, approximately 1.41 tonnes of limestone must be calcined to produce CaO.³ Dissociation during that process results in 620 kg of CO₂ emissions. In contrast, we estimate that between 0.57 and 0.72 tonnes of limestone must be calcined to manufacture one tonne of cured CCSH-cement using the general process and materials we used in this work to make pseudowollastonite. That would produce approximately 251-315 kg CO₂, or 40-51% of the emissions from this process in OPC manufacture.

During pyroprocessing for OPC clinker production, CaO and sources of silica and alumina must be heated to 1450 °C to produce clinker. There are numerous kiln configurations and techniques for this process but we used Huntzinger and Eatmon's estimations of coal, fuel oil, and natural gas quantities used to heat one tonne of OPC,³ along with U.S Energy Information Agency emissions factors¹³³ for those sources to estimate that 406 kg CO₂ are emitted per tonne of OPC cement. Conversely, pseudowollastonite for CCSH cement must be heated to 1175 °C, which results in much lower fossil energy-related emissions for heating – approximately 218-273 kg per tonne of cured cement, assuming the same mix of heating sources.

Additionally, when CCSH cement is cured, there is uptake and utilization of approximately 169-338 kg CO₂ per tonne of cement (calculated from total carbon measurements of cured 7-day

and 28-day specimens in this work), resulting in a pulse of negative emissions, which does not exist during OPC curing. While the process outlined here for CCSH cement curing requires moderate temperatures (90 °C up to 140 °C), it is possible that waste heat from the pyroprocessing stage or from power plants could be utilized to provide that heat and both would also be sources concentrated CO₂, which is also required.

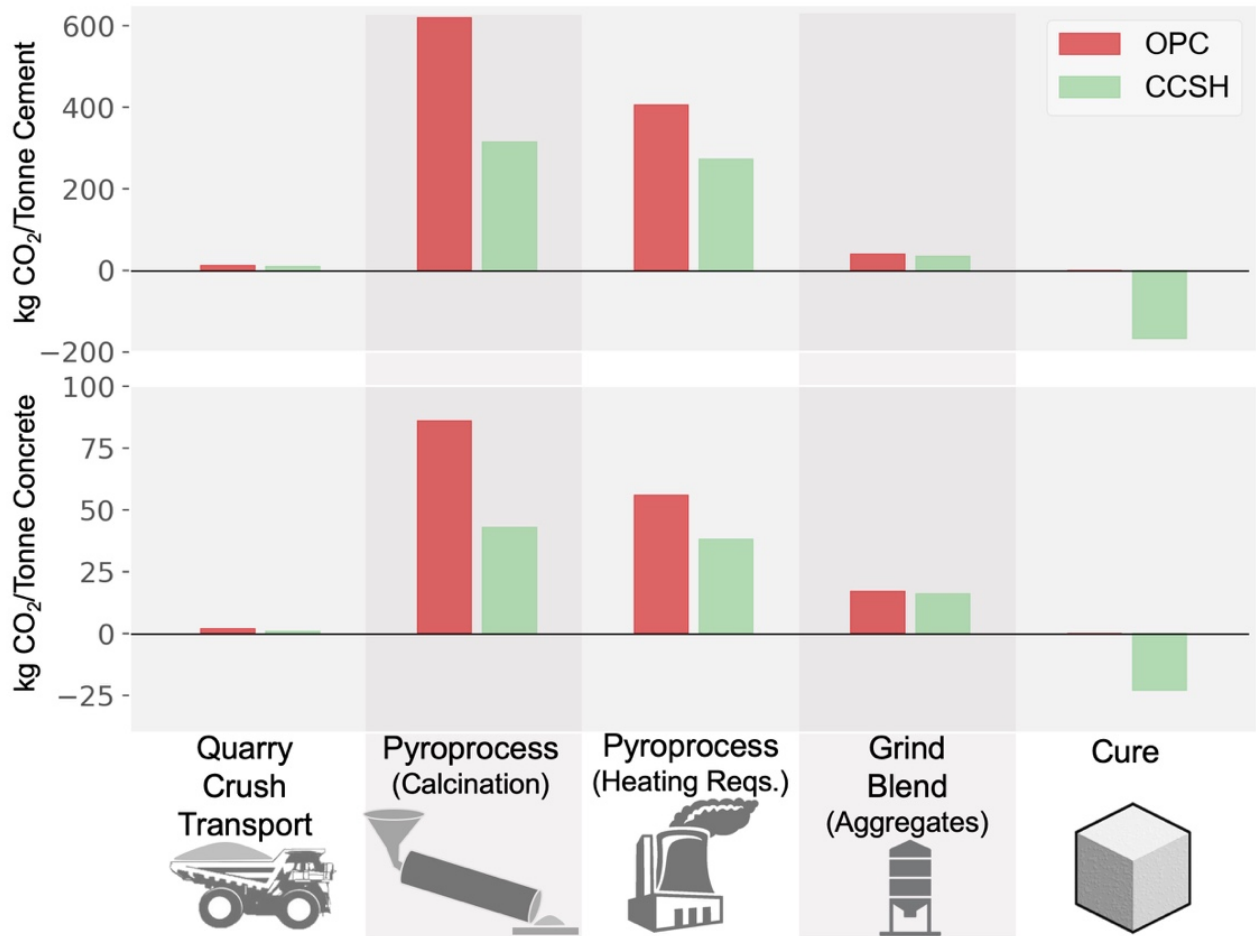


Figure 4.5. Lifecycle analysis results of OPC and CCSH cement reported on here suggest three major ways in which emission profiles are significantly different. First, significantly less limestone is required for CCSH cement, leading to fewer emissions from calcination. Second, during pyroprocessing, the lower temperatures required to make pseudowollastonite saves on fuel emissions, compared to OPC clinker. Finally, while curing, CCSH cement uptakes a significant amount of CO₂ (here, shown in terms of data from 7-day curing).

Taken collectively, we estimate that CCSH cement and concrete would have CO₂ emissions of 165-461 and 35-75 kg CO₂/tonne, respectively, whereas conventional OPC has

emissions of 1,077 and 160 kg CO₂/tonne. The complete life cycle model is available in Appendix II.

4.4. Discussion

The results presented here provide the first connection between formulations, curing methods, mechanical properties, and environmental footprint of CCSH phases in the context of high-performance and low-environmental-impact cement. While this study was designed to provide a proof-of-concept, other important metrics of cement performance could be carried out moving forward. For example, cements are often evaluated in terms of their ductility because ductile concrete is able to deflect under stress without cracking, thereby limiting freeze-thaw and solute transport effects. The ductility of ancient Roman cements has been identified as one of the reasons they performed as well as they did. In addition, we report moderate strength achieved by CCSH-mortar in 7 days because that period is common in OPC literature. The curing process reported here is meant to demonstrate that there are feasible pathways that lead to CCSH cements and that those cements should be of interest to the scientific community because of the lifecycle analyses and performance metrics presented here, including durability, chemical stability, and carbon uptake. Although our proposed curing process is most appropriate for precast and unit concrete/masonry, which is relatively limited in use compared to pour-in-place, it is the fastest growing share of the cement market and is expected to exceed 20% in the coming years.

At the systems-scale, our analysis suggests that these materials could be synthesized with a fraction of the energy demand and climate impact of conventional Portland cement. Considerable effort has focused on identifying industrial waste streams that could be used as substitutes for mined sources of CaO and SiO₂ in OPC and the curing approach proposed here could rely on some

of these waste streams to produce pseudowollastonite or aqueous conditions needed to produce high-performance cements with even lower emissions than reported here.

4.5. Methods

4.5.1. Pseudowollastonite Synthesis.

A 1:1 calcium:silicon mixture was produced on the kilogram-scale by milling HuberCrete G Extra Fine Limestone (Huber Engineered Materials) with Elkem Microsilica 965U (Elkem Materials, Inc.) in 5-liter ball mills for one hour. The milled powder was then mixed with a 5% NaOH/water solution at 25%. The NaOH acts as a flux during the heating process to create higher-purity pseudowollastonite, though it is not required.¹³⁴ The mixture was dried and then heated at 1225 °C for 6 hours in a kiln, although temperatures as low as 1175 °C and shorter durations were tested and yielded pseudowollastonite. We chose to use NaOH, higher temperature, and longer heating time to ensure the highest possible quality pseudowollastonite for research purposes. The pseudowollastonite was then ground, ball-milled for 1 hour, and sieved to pass the number 200 sieve. X-ray diffraction, via a Panalytical X'pert Pro diffractometer with a copper source ($K\alpha = 1.5406 \text{ \AA}$) from 15 - 65° 2 θ , shown in Appendix II. Analysis via Panalytical HighScore Plus with PDF-4+ 2019 database confirmed an excellent match for pseudowollastonite.

4.5.2. Mortar Cube Design of Experiments.

2-in mortar cubes were cast and tested in compression in accordance with standard ASTM specification C109. From previous work,^{102,128} along with preliminary experiments, we established a general methodology for curing the mortar specimens, which includes (1) elevating the pH of the mix water, curing the specimens at 90 °C and (2) elevated pressure of CO₂ gas for 72 hr until the specimens are hardened, then demolding and submerging them in (3) an alkaline solution again at (4) elevated temperature with (5) CO_{2(aq)} for 96 hours, for a total of 7 days of curing. Water-CO₂

equilibrium pH was calculated with PHREEQC (V 2.18) with the PHREEQC database. The purpose for the 3-day dry-curing period was to harden the cubes so that they could be demolded and handled and the initial (buffered) mix water within the cubes facilitated the carbonation/hydration reactions. During the 4-day wet-curing phase, the CO₂ in the headspace equilibrates with the water, depending on temperature, partial pressure, and concentration of NaOH and previous work has shown that these factors all affect CCSH precipitation dynamics so the Taguchi design of experiments was employed to determine the curing conditions to yield the highest 7-day compressive strength by testing three levels of each of the five factors, which is shown in Appendix II. After the initial Taguchi matrix was completed, another three-factor, two-level one (see Appendix II) was used to determine optimal mix proportions of sand, pseudowollastonite, and water, also in terms of compressive strength, which was measured with a Humboldt Master Loader Elite Series load frame.

4.5.3. Carbon Uptake.

Portions from crushed mortar specimens were collected, ground with a mortar and pestle, and analyzed via a Shimadzu SSM5000A total carbon analyzer. The analyzer heats the samples to 980 °C, where solid carbon decomposes, and detects the mass of carbon in a stream of oxygen. Because the samples include the sand from the mortar, the carbon content, a percent of the original sample mass, was adjusted to be expressed in terms of the mass of cement (pseudowollastonite) based on the mix proportions of cement-to-sand.

4.5.4 Diffusion Mapping.

A small cylindrical mortar sample (14 mm diameter by 30 mm length) was cast and cured in conditions similar to the optimized curing conditions from the first Taguchi matrix, with the exception that it was set in dry CO₂ for 24 hours and then set in the aqueous phase for 48 hours.

An ordinary Portland cement mortar specimen (Type I/II) of the same size was made with C109 standard mix proportions and was cured for 1 day in the mold then submerged, demolded, in water and allowed to cure for 6 more days. Both samples were then then submerged in fresh DI water for 1 hour to saturate the samples. Subsequently, they were submerged in a 0.1 M NaBr (J.T. Baker, ACS reagent) solution for 6 hours where the Br diffused from the solution, into the samples. They were then removed and dried in an oven at 75 °C, epoxied (Buhler EpoThin 2), and sectioned lengthwise.

For each sample, synchrotron X-ray fluorescence mapping of Br was conducted on a 3 mm wide by 4.5 mm deep section that began at the outer edge of the specimen. The mapping was completed at the 13-IDE sector at the Advanced Photon Source with a 4-element silicon drift diode detector at an incident energy of 18 keV with 20 μm steps and dwell times of 20 ms. More information about the beam and sector setup can be found in Lanzirotti et al.¹⁰⁹ Map data were exported from Larch software¹¹⁰ and visualized in Python 3.6 with the viridis colormap. The colormap ranges were identical between both maps. For each pixel, the Br counts were normalized to the incident energy for that pixel to account for fluctuations in the beam intensity. Because the colors are equal representations of the Br counts detected at each pixel in each sample, and because the detector geometry was the same between both, the relative concentrations of Br may be compared between the two maps.

4.5.5. Acid Dissolution Tests.

Two mortar cubes were cured similarly to the optimal design from the first Taguchi matrix to test their resistance to acid dissolution. Two additional, predominately carbonate cubes were created with the same mix but without any pH buffering from NaOH and two additional OPC cubes were cured for 28 days. All six cubes were dried, weighed, and submerged for 7 days in a 1

M sodium acetate and acetic acid solution at pH 5.⁶⁸ After 7 days, the specimens were removed, oven dried, and loose materials were gently removed by hand. They were then reweighed to determine mass loss during the acid treatment. Compressive strengths could not be determined because the surfaces of the specimens were rough and no longer remotely planar in some cases.

4.5.6. Lifecycle Analysis.

The functional unit for the lifecycle comparison between OPC and CCSH cement manufacturing emissions was 1 metric tonne of cured cement. We also expressed emissions in terms of 1 tonne of cured concrete, assuming that cement comprises 14% of concrete. The use phase was outside of the scope of the LCA because of its high variability, though it should be noted that it is possible for OPC to carbonate (and CCSH cement to continue carbonating) over decades with exposure to atmospheric CO₂. However, those timescales, along with an inability to predict the carbonation extents, make it difficult to incorporate those emissions reductions and do not align with the urgent need to decarbonize as established by the IPCC.¹¹⁵

The emissions associated with raw material quarrying, crushing, and transporting were retrieved from an extensive analysis by Marceau et al. for OPC that assumed the use of raw materials including limestone, sand, clay, iron ore, and gypsum.¹¹⁹ Since our production scenario for pseudowollastonite is currently based on utilizing waste silica fume (or fly ash) and mined limestone, the emissions for 1 tonne of OPC for this process were scaled based on the mass of limestone for pseudowollastonite manufacture compared to the mass of all raw materials mined for OPC manufacture. Also, since CCSH cement sequesters CO₂ as a solid, which accounts for some percentage of the mass of the cured cement, less pseudowollastonite would be required to produce 1 tonne of cured CCSH cement so less limestone is required based on that aspect as well. Those figures are tabulated in Appendix II.

The emissions based on the calcination are based on the theoretical mass of CO₂ (molar mass = 44 g/mol) in limestone, which was assumed to be pure CaCO₃ (100 g/mol). The mass of limestone required to make one tonne of cured OPC and CCSH-cement was multiplied by 0.44 to obtain CO₂ emissions from this process.

The pyroprocess emissions from fuel combustion that is required to heat raw materials to 1450 °C for OPC manufacture was calculated by first determining typical fuel requirements, established by Huntzinger and Eatmon.³ Those fuel sources include coal, fuel oil, and natural gas, the percentages of which admittedly may vary widely with time and geographic location. Those fuel requirements were multiplied by the appropriate emissions factors established by the U.S. Energy Information Administration (EIA).¹³³ The emissions for this process were assumed to scale linearly from 1450 °C for OPC to 1175 °C for pseudowollastonite (the temperature we have determined to be acceptable in our work).

Emissions from finish grinding and blending of OPC were also calculated by multiplying the typical fuel source requirements (energy from coal, fuel oil, and natural gas) from Huntzinger and Eatmon by the appropriate EIA emissions factors. The same energy requirements for this process were assumed for pseudowollastonite manufacture with the exception of scaling for the pseudowollastonite required to produce our functional unit, 1 tonne of cured cement.

Carbon uptake during the curing process for OPC was assumed to be negligible because it cures via hydration (not carbonation) in atmospheric concentrations of CO₂. For CCSH cement, CO₂ uptake was based on empirical data of percent carbon in the 7-day and 28-day mortar specimens presented in this work. The percent of carbon in mortar was measured and was then expressed in terms of the percent carbon in the cement phase (pseudowollastonite) of the mortar based on our mortar mix ratios. The percent carbon in the cement was then expressed in terms of

percent CO₂ in the cement phase by multiplying by the ratio of the molar mass of CO₂ to the molar mass of carbon.

To express lifecycle emissions in terms of concrete, cement emissions were multiplied by the percent of cement that typically exists in concrete. Here, we assumed 14% based on a mix of 1-part cement, 3-parts sand, 3-parts larger aggregate, and 0.5 parts water (half of which is consumed during hydration). That mixture was assumed to be identical between OPC concrete and CCSH-based concrete. We also added typical emissions that are associated with aggregate production, concrete plant operations, and cement/aggregate transport to concrete facilities based on volumetric emissions from an analysis of precast concrete performed by Nisbet et al.¹³⁵ and we assumed those emissions to be identical for both types of concrete. Those volumetric emissions were converted to mass emissions by assuming a concrete density of 2,400 kg/m³. Although CCSH concrete would be cured at elevated temperatures, we assume that heat is waste from other industrial processes as described in the main text so those emissions have been omitted.

Chapter 5. Conclusions and Future Work

5.1. Conclusions

This dissertation explored the reactivity and application of calcium silicates in the presence of CO₂ solutions. The complexity and nuance of mineral carbonation was shown to be impacted by the crystal structure of the silicate reactant and solution chemistry demonstrated in Chapter 2. In prior literature, the reaction of model mineral silicates (CaSiO₃) with CO₂ was assumed to follow a reaction pathway that yielded a solid carbonate and amorphous silica. This work showed that other pathways exist that yield CCSH phases with significantly different chemical and mechanical properties. The applications of these CCSH phases in a variety of carbon storage and infrastructure applications was explored in Chapters 3 and 4. In conclusion, this section will summarize the main contributions presented here by returning to the three research questions posed in Chapter 1.

1. *Why does the aqueous carbonation of pseudowollastonite result in different products than its polymorph, wollastonite, and how are the products fundamentally different?*

- Using ICP-OES measurements of calcium and silicon concentrations during wollastonite and pseudowollastonite dissolution, this work shows that wollastonite dissolves incongruently (with Ca being released sooner and at higher concentrations than Si) while pseudowollastonite dissolves congruently. The availability of Si in the aqueous phase is crucial for the precipitation of non-carbonate phases.
- With pseudowollastonite, it was shown that pH plays a key role in precipitate chemistry, most likely by allowing greater concentrations of reactive Si to exist in the aqueous phase. When CO₂ is introduced and pH decreases, the Si becomes supersaturated and complexes with Ca and possibly carbon to form CCSHs.

- The CCSH phases were found to be highly variable in terms of their Si:Ca ratios (SEM-EDS) and of their crystal structures (XRD, TEM-SAED) but were found to be more resistant to dissolution at low pH than calcium carbonate was.
2. *How do these products differ in terms of their impact on fluid flow in porous media and ability to sequester carbon in the subsurface?*
- Pseudowollastonite-injected sand columns were used as surrogate porous media in conditions representative of CO₂ injection into the subsurface. When CO₂ was allowed to diffuse into the columns, calcium carbonate was found to precipitate, which resulted in 1.16 orders of magnitude reduction in permeability at 495 hr. In contrast, when pH was buffered and CO₂ was injected, CCSHs were found to form and decrease permeability by 2.83 orders of magnitude at 495 hr.
 - In carbonate-dominated columns, calcium carbonate was found to dissolve near the column inlets and precipitate deeper into the columns over time. The location of CCSHs were not observed to change over the same experimental timeframe, which could suggest they may form more permanent seals in the subsurface.
 - Calcium carbonate was found to precipitate indiscriminately throughout pore bodies while CCSHs tended to precipitate along the sand grain interfaces, leaving a large portion of the pore body open. This suggests that carbon may be sequestered not only in CCSHs (e.g., as scawtite) and solid carbonates, but also in the pore solution (i.e., solubility trapping).
3. *Can these products be leveraged to produce environmentally sustainable cement that is comparable to traditional Portland cement?*

- CCSH-based mortar samples created with pseudowollastonite and a novel curing technique (that requires $\text{CO}_{2(\text{aq})}$ in a buffered solution) suggest compressive strength comparable to that of OPC-based mortar may be achieved in 7 days.
- The CCSH-based mortar was shown to exhibit lower diffusivity to dissolved ions compared to OPC, which may indicate enhanced durability.
- CCSH-based mortar was also shown to be more resistant to dissolution at low pH than carbonate-based and OPC-based mortars, which may also lead to increased longevity, particularly in harsh environments.
- Finally, a lifecycle analysis suggested that CCSH cement may be produced with 85% lower CO_2 emissions than OPC, which could significantly contribute to decarbonization of the global economy.

5.2. Future Work

Much of the work presented in this dissertation involves model calcium silicates, wollastonite and pseudowollastonite, both of which are commonly used in the laboratory setting due to their relatively fast reaction rates compared to other mineral silicates. But, just as described in Chapter 2, there are likely unforeseen reaction pathways that take place with other common minerals, including di- and tricalcium silicates (important in concrete chemistry) and magnesium silicates (important in carbon sequestration in basalt). Experiments involving these other common minerals could explore environmental conditions similar to those presented throughout this work to determine whether the trends involving the mechanism of dissolution and impact of pH established in Chapter 2 are universal or limited to CaSiO_3 and whether novel reaction products (i.e., other than solid carbonates) are able to form.

Among the most challenging and unachievable tasks in this work has been the conclusive identification of the CCSH phases. This issue is shared in concrete chemistry work as CSH gels are often difficult, if not impossible, to identify with most techniques. However, solid-state nuclear magnetic resonance spectroscopy (NMR) is an advanced technique that is used to determine local magnetic fields around atomic nuclei, thereby resolving atomic structure. This technique could be used to identify the CCSH phases but because they are heterogenous in composition and NMR requires homogeneous samples on the mg-scale, the same issues of identification could arise. While it was not found that the CCSHs approach any definite elemental composition under the conditions tested here in 7 days, it is possible that much longer experiments may yield more homogeneous precipitates.

In the context of cement research, there are many more tests to determine physical characteristics of cured specimens than are presented in this work. Of principal importance is to scale mortar tests to concrete in order to fully evaluate the potential strength of CCSH-based cement. In addition, curing conditions should continue to be investigated, with special technoeconomic and feasibility considerations in mind. The work here serves as a proof-of-concept for CCSH cement but there are many years of work to be done to truly ‘optimize’ any concrete formulation. Yet to be determined are characteristics of CCSH-cement ductility. Some researchers believe that high ductility is partially responsible for the longevity of Roman cements because ductile concrete is able to deflect under stress without cracking, thereby limiting freeze-thaw and solute transport effects.

Finally, there is a great deal of ongoing research concerned with utilizing industrial waste streams to increase performance or decrease the environmental footprint of OPC. However, here it has been shown that the lower Ca:Si cements are capable of yielding CCSHs similar to those in

Roman cements and the lower amount of calcium translates to significant reductions in CO₂ emissions when using limestone as the CaO source. Combining the knowledge presented here in the context of Ca:Si ratios and the idea of waste-stream-utilization may have a profound impact on the cement industry and may eventually lead to carbon-negative cement.

References

- (1) United States Geological Survey. *Mineral Commodity Summaries: Cement*; 2019.
- (2) Van Oss, H. G. *Cement 2015*; Vol. 16.
- (3) Huntzinger, D. N.; Eatmon, T. D. A Life-Cycle Assessment of Portland Cement Manufacturing: Comparing the Traditional Process with Alternative Technologies. *J. Clean. Prod.* **2009**, *17* (7), 668–675. <https://doi.org/10.1016/J.JCLEPRO.2008.04.007>.
- (4) Miller, S. A.; Horvath, A.; Monteiro, P. J. M. Readily Implementable Techniques Can Cut Annual CO₂ Emissions from the Production of Concrete by over 20%. *Environ. Res. Lett.* **2016**, *11* (7), 074029. <https://doi.org/10.1088/1748-9326/11/7/074029>.
- (5) Worrell, E.; Price, L.; Martin, N.; Hendriks, C.; Meida, L. O. CARBON DIOXIDE EMISSIONS FROM THE GLOBAL CEMENT INDUSTRY. *Annu. Rev. Energy Environ.* **2001**, *26* (1), 303–329. <https://doi.org/10.1146/annurev.energy.26.1.303>.
- (6) American Society of Civil Engineers. *A Comprehensive Assessment of America's Infrastructure*.
- (7) Pellenq, R. J.-M.; Kushima, A.; Shahsavari, R.; Van Vliet, K. J.; Buehler, M. J.; Yip, S.; Ulm, F.-J. A Realistic Molecular Model of Cement Hydrates. *Proc. Natl. Acad. Sci. U. S. A.* **2009**, *106* (38), 16102–16107. <https://doi.org/10.1073/pnas.0902180106>.
- (8) Frias, M.; Goñi, S.; García, R.; Vigil de La Villa, R. Seawater Effect on Durability of Ternary Cements. Synergy of Chloride and Sulphate Ions. *Compos. Part B Eng.* **2013**, *46*, 173–178. <https://doi.org/10.1016/J.COMPOSITESB.2012.09.089>.
- (9) Ben-Yair, M. The Durability of Cement and Concrete in Sea Water. *Desalination* **1967**, *3* (2), 147–154. [https://doi.org/10.1016/0011-9164\(67\)80004-3](https://doi.org/10.1016/0011-9164(67)80004-3).
- (10) Zhang, C.; Dehoff, K.; Hess, N.; Ostrom, M.; Wietsma, T. W.; Valocchi, A. J.; Fouke, B. W.; Werth, C. J. Pore-Scale Study of Transverse Mixing Induced CaCO₃ Precipitation and Permeability Reduction in a Model Subsurface Sedimentary System. *Environ. Sci. Technol.* **2010**, *44* (20), 7833–7838. <https://doi.org/10.1021/es1019788>.
- (11) Nogues, J. P.; Fitts, J. P.; Celia, M. A.; Peters, C. A. Permeability Evolution Due to Dissolution and Precipitation of Carbonates Using Reactive Transport Modeling in Pore Networks. <https://doi.org/10.1002/wrcr.20486>.
- (12) Stack, A. G.; Fernandez-Martinez, A.; Allard, L. F.; Bañuelos, J. L.; Rother, G.; Anovitz, L. M.; Cole, D. R.; Waychunas, G. A. Pore-Size-Dependent Calcium Carbonate Precipitation Controlled by Surface Chemistry. *Environ. Sci. Technol.* **2014**, *48* (11), 6177–6183. <https://doi.org/10.1021/es405574a>.
- (13) Poonoosamy, J.; Curti, E.; Kosakowski, G.; Grolimund, D.; Van Loon, L. R.; Mäder, U. Barite Precipitation Following Celestite Dissolution in a Porous Medium: A SEM/BSE and μ -XRD/XRF Study. *Geochim. Cosmochim. Acta* **2016**, *182*, 131–144. <https://doi.org/10.1016/J.GCA.2016.03.011>.
- (14) Hajirezaie, S.; Wu, X.; Peters, C. A. Scale Formation in Porous Media and Its Impact on Reservoir Performance during Water Flooding. *J. Nat. Gas Sci. Eng.* **2017**, *39*, 188–202. <https://doi.org/10.1016/J.JNGSE.2017.01.019>.
- (15) Li, Q.; Steefel, C. I.; Jun, Y.-S. Incorporating Nanoscale Effects into a Continuum-Scale Reactive Transport Model for CO₂-Deteriorated Cement. *Environ. Sci. Technol.* **2017**, *51* (18), 10861–10871. <https://doi.org/10.1021/acs.est.7b00594>.
- (16) Stanislao, C.; Rispoli, C.; Vola, G.; Cappelletti, P.; Morra, V.; De Gennaro, M. Contribution to the Knowledge of Ancient Roman Seawater Concretes: Phlegrean Pozzolan Adopted in the Construction of the Harbour at Soli-Pompeiiopolis (Mersin,

- Turkey). *Period. di Mineral.* **2011**, *80* (3), 471–488. <https://doi.org/10.2451/2011PM0031>.
- (17) Xiong, W.; Wells, R. K.; Menefee, A. H.; Skemer, P.; Ellis, B. R.; Giammar, D. E. CO₂ Mineral Trapping in Fractured Basalt. *Int. J. Greenh. Gas Control* **2017**, *66*, 204–217. <https://doi.org/10.1016/J.IJGGC.2017.10.003>.
- (18) Menefee, A. H.; Giammar, D. E.; Ellis, B. R. Permanent CO₂ Trapping through Localized and Chemical Gradient-Driven Basalt Carbonation. *Environ. Sci. Technol.* **2018**, *52* (15), 8954–8964. <https://doi.org/10.1021/acs.est.8b01814>.
- (19) Giammar, D. E.; Wang, F.; Guo, B.; Surface, J. A.; Peters, C. A.; Conradi, M. S.; Hayes, S. E. Impacts of Diffusive Transport on Carbonate Mineral Formation from Magnesium Silicate-CO₂-Water Reactions. *Environ. Sci. Technol.* **2014**. <https://doi.org/10.1021/es504047t>.
- (20) Tao, Z.; Fitts, J. P.; Clarens, A. F. Feasibility of Carbonation Reactions to Control Permeability in the Deep Subsurface. *Environ. Eng. Sci.* **2016**, *33* (10), 778–790. <https://doi.org/10.1089/ees.2016.0026>.
- (21) Richardson, I. . The Nature of C-S-H in Hardened Cements. *Cem. Concr. Res.* **1999**, *29* (8), 1131–1147. [https://doi.org/10.1016/S0008-8846\(99\)00168-4](https://doi.org/10.1016/S0008-8846(99)00168-4).
- (22) Midgley, H. G. The Determination of Calcium Hydroxide in Set Portland Cements. *Cem. Concr. Res.* **1979**, *9* (1), 77–82.
- (23) Barlet-Gouedard, V.; Rimmele, G.; Goffe, B.; Porcherie, O. Mitigation Strategies for the Risk of CO₂ Migration through Wellbores. In *IADC/SPE drilling conference*; Society of Petroleum Engineers, 2006.
- (24) Brunet, J.-P. L.; Li, L.; Karpyn, Z. T.; Kutchko, B. G.; Strazisar, B.; Bromhal, G. Dynamic Evolution of Cement Composition and Transport Properties under Conditions Relevant to Geological Carbon Sequestration. *Energy & Fuels* **2013**, *27* (8), 4208–4220. <https://doi.org/10.1021/ef302023v>.
- (25) Kajaste, R.; Hurme, M. Cement Industry Greenhouse Gas Emissions – Management Options and Abatement Cost. *J. Clean. Prod.* **2016**, *112*, 4041–4052. <https://doi.org/10.1016/J.JCLEPRO.2015.07.055>.
- (26) Khatib, J. M. Performance of Self-Compacting Concrete Containing Fly Ash. *Constr. Build. Mater.* **2008**, *22* (9), 1963–1971.
- (27) Berndt, M. L. Properties of Sustainable Concrete Containing Fly Ash, Slag and Recycled Concrete Aggregate. *Constr. Build. Mater.* **2009**, *23* (7), 2606–2613.
- (28) Sata, V.; Jaturapitakkul, C.; Kiattikomol, K. Influence of Pozzolan from Various By-Product Materials on Mechanical Properties of High-Strength Concrete. *Constr. Build. Mater.* **2007**, *21* (7), 1589–1598.
- (29) Uzal, B.; Turanli, L.; Mehta, P. K. High-Volume Natural Pozzolan Concrete for Structural Applications. *ACI Mater. J.* **2007**, *104* (5), 535–538.
- (30) Batayneh, M.; Marie, I.; Asi, I. Use of Selected Waste Materials in Concrete Mixes. *Waste Manag.* **2007**, *27* (12), 1870–1876.
- (31) Konsta-Gdoutos, M. S.; Metaxa, Z. S.; Shah, S. P. Highly Dispersed Carbon Nanotube Reinforced Cement Based Materials. *Cem. Concr. Res.* **2010**, *40* (7), 1052–1059.
- (32) Suhendro, B. Toward Green Concrete for Better Sustainable Environment. *Procedia Eng.* **2014**, *95*, 305–320.
- (33) Park, D. C. Carbonation of Concrete in Relation to CO₂ Permeability and Degradation of Coatings. *Constr. Build. Mater.* **2008**, *22* (11), 2260–2268. <https://doi.org/10.1016/J.CONBUILDMAT.2007.07.032>.

- (34) Xiao, J.; Li, J.; Zhu, B.; Fan, Z. Experimental Study on Strength and Ductility of Carbonated Concrete Elements. *Constr. Build. Mater.* **2002**, *16* (3), 187–192. [https://doi.org/10.1016/S0950-0618\(01\)00034-4](https://doi.org/10.1016/S0950-0618(01)00034-4).
- (35) Shao, Y.; Rostami, V.; He, Z.; Boyd, A. J. Accelerated Carbonation of Portland Limestone Cement. *J. Mater. Civ. Eng.* **2014**, *26* (1), 117–124. [https://doi.org/10.1061/\(ASCE\)MT.1943-5533.0000773](https://doi.org/10.1061/(ASCE)MT.1943-5533.0000773).
- (36) Monkman, S.; Shao, Y. Assessing the Carbonation Behavior of Cementitious Materials. *J. Mater. Civ. Eng.* **2006**, *18* (6), 768–776. [https://doi.org/10.1061/\(ASCE\)0899-1561\(2006\)18:6\(768\)](https://doi.org/10.1061/(ASCE)0899-1561(2006)18:6(768)).
- (37) Ashraf, W.; Olek, J. Carbonation Behavior of Hydraulic and Non-Hydraulic Calcium Silicates: Potential of Utilizing Low-Lime Calcium Silicates in Cement-Based Materials. *J. Mater. Sci.* **2016**, *51* (13), 6173–6191. <https://doi.org/10.1007/s10853-016-9909-4>.
- (38) Ashraf, W.; Olek, J.; Tian, N. Nanomechanical Characterization of the Carbonated Wollastonite System; Nanotechnology in Construction; Springer, 2015; pp 71–77.
- (39) Newton, J. G. Natural and Induced Sinkhole Development in the Eastern United States. In *Proceedings of the Third International Symposium on Land Subsidence, International Association of Hydrological Sciences, Wallingford, UK*; 1984; pp 549–564.
- (40) Jackson, M. D.; Vola, G.; Všíanský, D.; Oleson, J. P.; Scheetz, B. E.; Brandon, C.; Hohlfelder, R. L. Cement Microstructures and Durability in Ancient Roman Seawater Concretes. In *Historic Mortars*; Springer Netherlands: Dordrecht, 2012; pp 49–76. https://doi.org/10.1007/978-94-007-4635-0_5.
- (41) Jackson, M. D.; Chae, S. R.; Mulcahy, S. R.; Meral, C.; Taylor, R.; Li, P.; Emwas, A.-H.; Moon, J.; Yoon, S.; Vola, G.; et al. Unlocking the Secrets of Al-Tobermorite in Roman Seawater Concrete. *Am. Mineral.* **2013**, *98* (10), 1669–1687. <https://doi.org/10.2138/am.2013.4484>.
- (42) Delatte, N. J. Lessons from Roman Cement and Concrete. *J. Prof. Issues Eng. Educ. Pract.* **2001**, *127* (3), 109–115. [https://doi.org/10.1061/\(ASCE\)1052-3928\(2001\)127:3\(109\)](https://doi.org/10.1061/(ASCE)1052-3928(2001)127:3(109)).
- (43) Deng, H.; Bielicki, J. M.; Oppenheimer, M.; Fitts, J. P.; Peters, C. A. Leakage Risks of Geologic CO₂ Storage and the Impacts on the Global Energy System and Climate Change Mitigation. *Clim. Change* **2017**, *144* (2), 151–163. <https://doi.org/10.1007/s10584-017-2035-8>.
- (44) Zahasky, C.; Benson, S. M. Evaluation of the Effectiveness of Injection Termination and Hydraulic Controls for Leakage Containment. *Energy Procedia* **2014**, *63*, 4666–4676.
- (45) Yang, Y.; Min, Y.; Lococo, J.; Jun, Y.-S. Effects of Al/Si Ordering on Feldspar Dissolution: Part I. Crystallographic Control on the Stoichiometry of Dissolution Reaction. *Geochim. Cosmochim. Acta* **2014**, *126*, 574–594.
- (46) Yang, Y.; Min, Y.; Jun, Y.-S. Effects of Al/Si Ordering on Feldspar Dissolution: Part II. The PH Dependence of Plagioclases' Dissolution Rates. *Geochim. Cosmochim. Acta* **2014**, *126*, 595–613.
- (47) Casey, W. H.; Westrich, H. R.; Banfield, J. F.; Ferruzzi, G.; Arnold, G. W. Leaching and Reconstruction at the Surfaces of Dissolving Chain-Silicate Minerals. *Nature* **1993**, *366* (6452), 253–256. <https://doi.org/10.1038/366253a0>.
- (48) Schott, J.; Pokrovsky, O. S.; Spalla, O.; Devreux, F.; Gloter, A.; Mielczarski, J. A. Formation, Growth and Transformation of Leached Layers during Silicate Minerals Dissolution: The Example of Wollastonite. *Geochim. Cosmochim. Acta* **2012**, *98*, 259–

- 281.
- (49) Yang, H.; Prewitt, C. T. On the Crystal Structure of Pseudowollastonite (CaSiO₃). *Am. Mineral.* **1999**, *84* (5–6), 929–932.
- (50) Casey, W. H. Glass and Mineral Corrosion: Dynamics and Durability. *Nat. Mater.* **2008**, *7* (12), 930.
- (51) Bracco, J. N.; Grantham, M. C.; Stack, A. G. Calcite Growth Rates as a Function of Aqueous Calcium-to-Carbonate Ratio, Saturation Index, and Inhibitor Concentration: Insight into the Mechanism of Reaction and Poisoning by Strontium. *Cryst. Growth Des.* **2012**, *12* (7), 3540–3548.
- (52) Galvánková, L.; Másilko, J.; Solný, T.; Štěpánková, E. Tobermorite Synthesis Under Hydrothermal Conditions. *Procedia Eng.* **2016**, *151*, 100–107.
<https://doi.org/10.1016/J.PROENG.2016.07.394>.
- (53) Fletcher, R. A.; Bibby, D. M. Synthesis of Kenyaite and Magadiite in the Presence of Various Anions. *Clays Clay Miner.* **1987**, *35* (4), 318–320.
- (54) Jackson, M. D.; Moon, J.; Gotti, E.; Taylor, R.; Chae, S. R.; Kunz, M.; Emwas, A.; Meral, C.; Guttmann, P.; Levitz, P. Material and Elastic Properties of Al-tobermorite in Ancient Roman Seawater Concrete. *J. Am. Ceram. Soc.* **2013**, *96* (8), 2598–2606.
- (55) Mokhtar, M. Application of Synthetic Layered Sodium Silicate Magadiite Nanosheets for Environmental Remediation of Methylene Blue Dye in Water. *Materials (Basel)*. **2017**, *10* (7), 760.
- (56) Jackson, M. D.; Mulcahy, S. R.; Chen, H.; Li, Y.; Li, Q.; Cappelletti, P.; Wenk, H.-R. Phillipsite and Al-Tobermorite Mineral Cements Produced through Low-Temperature Water-Rock Reactions in Roman Marine Concrete. *Am. Mineral. J. Earth Planet. Mater.* **2017**, *102* (7), 1435–1450.
- (57) Ma, Y.; Liu, N.; Jin, X.; Feng, T. Hydrothermal Synthesis of Mesoporous Magadiite Plates via Heterogeneous Nucleation. *Clays Clay Miner.* **2013**, *61* (6), 525–531.
<https://doi.org/10.1346/CCMN.2013.0610605>.
- (58) Garrault-Gauffinet, S.; Nonat, A. Experimental Investigation of Calcium Silicate Hydrate (CSH) Nucleation. *J. Cryst. Growth* **1999**, *200* (3–4), 565–574.
- (59) Snæbjörnsdóttir, S. Ó.; Gíslason, S. R.; Galeczka, I. M.; Oelkers, E. H. Reaction Path Modelling of In-Situ Mineralisation of CO₂ at the CarbFix Site at Hellisheidi, SW-Iceland. *Geochim. Cosmochim. Acta* **2018**, *220*, 348–366.
<https://doi.org/10.1016/J.GCA.2017.09.053>.
- (60) Kelemen, P. B.; Matter, J. In Situ Carbonation of Peridotite for CO₂ Storage. *Proc. Natl. Acad. Sci.* **2008**, *105* (45), 17295–17300.
- (61) Krevor, S. C. M.; Lackner, K. S. Enhancing Serpentine Dissolution Kinetics for Mineral Carbon Dioxide Sequestration. *Int. J. Greenh. Gas Control* **2011**, *5* (4), 1073–1080.
<https://doi.org/10.1016/J.IJGGC.2011.01.006>.
- (62) Zhao, H.; Park, Y.; Lee, D. H.; Park, A.-H. A. Tuning the Dissolution Kinetics of Wollastonite via Chelating Agents for CO₂ Sequestration with Integrated Synthesis of Precipitated Calcium Carbonates. *Phys. Chem. Chem. Phys.* **2013**, *15* (36), 15185.
<https://doi.org/10.1039/c3cp52459k>.
- (63) Bourg, I. C.; Beekingham, L. E.; DePaolo, D. J. The Nanoscale Basis of CO₂ Trapping for Geologic Storage. *Environ. Sci. Technol.* **2015**, *49* (17), 10265–10284.
<https://doi.org/10.1021/acs.est.5b03003>.
- (64) Fitts, J. P.; Peters, C. A. Caprock Fracture Dissolution and CO₂ Leakage. *Rev. Mineral.*

- Geochemistry* **2013**, 77 (1), 459–479.
- (65) Huang, X.-H.; Chang, J. Synthesis of Nanocrystalline Wollastonite Powders by Citrate–Nitrate Gel Combustion Method. *Mater. Chem. Phys.* **2009**, 115 (1), 1–4.
 - (66) Speakman, K. The Stability of Tobermorite in the System CaO–SiO₂–H₂O at Elevated Temperatures and Pressures. *Mineral. Mag.* **1968**, 36 (284), 1090–1103.
 - (67) Shaw, S.; Clark, S. M.; Henderson, C. M. B. Hydrothermal Formation of the Calcium Silicate Hydrates, Tobermorite (Ca₅Si₆O₁₆(OH)₂·4H₂O) and Xonotlite (Ca₆Si₆O₁₇(OH)₂): An in Situ Synchrotron Study. *Chem. Geol.* **2000**, 167 (1), 129–140.
 - (68) Han, F. X.; Banin, A. Selective Sequential Dissolution Techniques for Trace Metals in Arid-zone Soils: The Carbonate Dissolution Step. *Commun. Soil Sci. Plant Anal.* **1995**, 26 (3–4), 553–576. <https://doi.org/10.1080/00103629509369318>.
 - (69) Daval, D.; Martinez, I.; Guigner, J.-M.; Hellmann, R.; Corvisier, J.; Findling, N.; Dominici, C.; Goffe, B.; Guyot, F. Mechanism of Wollastonite Carbonation Deduced from Micro- to Nanometer Length Scale Observations. *Am. Mineral.* **2009**, 94 (11–12), 1707–1726. <https://doi.org/10.2138/am.2009.3294>.
 - (70) Given, R. K.; Wilkinson, B. H. Kinetic Control of Morphology, Composition, and Mineralogy of Abiotic Sedimentary Carbonates. *J. Sediment. Res.* **1985**, 55 (1).
 - (71) Cailleteau, C.; Angeli, F.; Devreux, F.; Gin, S.; Jestin, J.; Jollivet, P.; Spalla, O. Insight into Silicate-Glass Corrosion Mechanisms. *Nat. Mater.* **2008**, 7 (12), 978–983. <https://doi.org/10.1038/nmat2301>.
 - (72) Weissbart, E. J.; Rimstidt, J. D. Wollastonite: Incongruent Dissolution and Leached Layer Formation. *Geochim. Cosmochim. Acta* **2000**, 64 (23), 4007–4016. [https://doi.org/10.1016/S0016-7037\(00\)00475-0](https://doi.org/10.1016/S0016-7037(00)00475-0).
 - (73) Zakaznova-Herzog, V. P.; Nesbitt, H. W.; Bancroft, G. M.; Tse, J. S. Characterization of Leached Layers on Olivine and Pyroxenes Using High-Resolution XPS and Density Functional Calculations. *Geochim. Cosmochim. Acta* **2008**, 72 (1), 69–86.
 - (74) Wang, F.; Giammar, D. E. Forsterite Dissolution in Saline Water at Elevated Temperature and High CO₂ Pressure. *Environ. Sci. Technol.* **2012**, 47 (1), 168–173.
 - (75) Bruant, R. G.; Guswa, A. J.; Celia, M. A.; Peters, C. A. Safe Storage of CO₂ in Deep Saline Aquifers. *Environ. Sci. Technol.* **2002**. <https://doi.org/10.1021/es0223325>.
 - (76) Clarens, A. F.; Peters, C. A. Mitigating Climate Change at the Carbon Water Nexus: A Call to Action for the Environmental Engineering Community. *Environ. Eng. Sci.* **2016**, 33 (10), 719–724. <https://doi.org/10.1089/ees.2016.0455>.
 - (77) Atrens, A. D.; Gurgenci, H.; Rudolph, V. Economic Optimization of a CO₂-Based EGS Power Plant. *Energy & Fuels* **2011**, 25 (8), 3765–3775. <https://doi.org/10.1021/ef200537n>.
 - (78) Pruess, K. Enhanced Geothermal Systems (EGS) Using CO₂ as Working Fluid—A Novel Approach for Generating Renewable Energy with Simultaneous Sequestration of Carbon. *Geothermics* **2006**, 35 (4), 351–367. <https://doi.org/10.1016/j.geothermics.2006.08.002>.
 - (79) Succar, S.; Williams, R. H. *Compressed Air Energy Storage: Theory Resources and Applications for Wind Power*; Princeton Environmental Institute, 2008.
 - (80) Dobson, P.; Kneafsey, T. J.; Blankenship, D.; Valladao, C.; Morris, J.; Knox, H.; Schwering, P.; White, M.; Doe, T.; Roggenthen, W.; et al. An Introduction to the EGS Collab Project. In *Transactions - Geothermal Resources Council*; Geothermal Resources Council, 2017; Vol. 41, pp 837–849.
 - (81) Feng, R.; Liu, J.; Chen, S.; Bryant, S. Effect of Gas Compressibility on Permeability

- Measurement in Coalbed Methane Formations: Experimental Investigation and Flow Modeling. *Int. J. Coal Geol.* **2018**, *198*, 144–155. <https://doi.org/10.1016/J.COAL.2018.09.010>.
- (82) Jun, Y.-S.; Giammar, D. E.; Werth, C. J.; Dzombak, D. A. Environmental and Geochemical Aspects of Geologic Carbon Sequestration: A Special Issue. *Environ. Sci. Technol.* **2013**, *47* (1), 1–2. <https://doi.org/10.1021/es304681x>.
- (83) Peters, C. A.; Ellis, B.; Peters, C.; Fitts, J.; Bromhal, G.; McIntyre, D.; Warzinski, R.; Rosenbaum, E. Deterioration of a Fractured Carbonate Caprock Exposed to CO₂-Acidified Brine Flow. | *Greenh. Gas Sci Technol* **2011**, *1*, 248–260. <https://doi.org/10.1002/ghg>.
- (84) Jun, Y.-S.; Giammar, D. E.; Werth, C. J. Impacts of Geochemical Reactions on Geologic Carbon Sequestration. *Environ. Sci. Technol.* **2013**, *47* (1), 3–8. <https://doi.org/10.1021/es3027133>.
- (85) Liang, B.; Clarens, A. F. Interactions Between Stratigraphy and Interfacial Properties on Flow and Trapping in Geologic Carbon Storage. *Water Resour. Res.* **2018**, *54* (1), 72–87. <https://doi.org/10.1002/2017WR021643>.
- (86) Vengosh, A.; Jackson, R. B.; Warner, N.; Darrah, T. H.; Kondash, A. A Critical Review of the Risks to Water Resources from Unconventional Shale Gas Development and Hydraulic Fracturing in the United States. *Environ. Sci. Technol.* **2014**, *48* (15), 8334–8348. <https://doi.org/10.1021/es405118y>.
- (87) Kutchko, B. G.; Strazisar, B. R.; Dzombak, D. A.; Lowry, G. V.; Thuirow, N. Degradation of Well Cement by CO₂ under Geologic Sequestration Conditions. *Environ. Sci. Technol.* **2007**, *41* (13), 4787–4792. <https://doi.org/10.1021/es062828c>.
- (88) Bauer, S.; Beyer, C.; Dethlefsen, F.; Dietrich, P.; Duttmann, R.; Ebert, M.; Feeser, V.; Görke, U.; Köber, R.; Kolditz, O.; et al. Impacts of the Use of the Geological Subsurface for Energy Storage: An Investigation Concept. *Environ. Earth Sci.* **2013**, *70* (8), 3935–3943. <https://doi.org/10.1007/s12665-013-2883-0>.
- (89) Vidic, R. D.; Brantley, S. L.; Vandenbossche, J. M.; Yoxtheimer, D.; Abad, J. D. Impact of Shale Gas Development on Regional Water Quality. *Science* **2013**, *340* (6134), 1235009. <https://doi.org/10.1126/science.1235009>.
- (90) Abidin, A. Z.; Puspasari, T.; Nugroho, W. A. Polymers for Enhanced Oil Recovery Technology. *Procedia Chem.* **2012**, *4*, 11–16. <https://doi.org/10.1016/J.PROCHE.2012.06.002>.
- (91) Mangadlao, J. D.; Cao, P.; Advincula, R. C. Smart Cements and Cement Additives for Oil and Gas Operations. *J. Pet. Sci. Eng.* **2015**, *129*, 63–76. <https://doi.org/10.1016/J.PETROL.2015.02.009>.
- (92) Huang, Z.-Q.; Winterfeld, P. H.; Xiong, Y.; Wu, Y.-S.; Yao, J. Parallel Simulation of Fully-Coupled Thermal-Hydro-Mechanical Processes in CO₂ Leakage through Fluid-Driven Fracture Zones. *Int. J. Greenh. Gas Control* **2015**, *34*, 39–51. <https://doi.org/10.1016/J.IJGGC.2014.12.012>.
- (93) Gurevich, A. E.; Endres, B. L.; Robertson, J. O.; Chilingar, G. V. Gas Migration from Oil and Gas Fields and Associated Hazards. *J. Pet. Sci. Eng.* **1993**, *9* (3), 223–238. [https://doi.org/10.1016/0920-4105\(93\)90016-8](https://doi.org/10.1016/0920-4105(93)90016-8).
- (94) Gasda, S. E.; Bachu, S.; Celia, M. A. Spatial Characterization of the Location of Potentially Leaky Wells Penetrating a Deep Saline Aquifer in a Mature Sedimentary Basin. *Environ. Geol.* **2004**, *46* (6–7), 707–720. <https://doi.org/10.1007/s00254-004-1073->

- 5.
- (95) Mason, H. E.; Du Frane, W. L.; Walsh, S. D. C.; Dai, Z.; Charnvanichborikarn, S.; Carroll, S. A. Chemical and Mechanical Properties of Wellbore Cement Altered by CO₂ - Rich Brine Using a Multianalytical Approach. *Environ. Sci. Technol.* **2013**, *47* (3), 1745–1752. <https://doi.org/10.1021/es3039906>.
- (96) Newell, D. L.; Carey, J. W. Experimental Evaluation of Wellbore Integrity Along the Cement-Rock Boundary. *Environ. Sci. Technol.* **2013**, *47* (1), 276–282. <https://doi.org/10.1021/es3011404>.
- (97) Cheshire, M. C.; Stack, A. G.; Carey, J. W.; Anovitz, L. M.; Prisk, T. R.; Ilavsky, J. Wellbore Cement Porosity Evolution in Response to Mineral Alteration during CO₂ Flooding. *Environ. Sci. Technol.* **2017**, *51* (1), 692–698. <https://doi.org/10.1021/acs.est.6b03290>.
- (98) Li, Q.; Lim, Y. M.; Flores, K. M.; Kranjc, K.; Jun, Y.-S. Chemical Reactions of Portland Cement with Aqueous CO₂ and Their Impacts on Cement's Mechanical Properties under Geologic CO₂ Sequestration Conditions. *Environ. Sci. Technol.* **2015**, *49* (10), 6335–6343. <https://doi.org/10.1021/es5063488>.
- (99) Cunningham, A. B.; Lauchnor, E.; Eldring, J.; Esposito, R.; Mitchell, A. C.; Gerlach, R.; Phillips, A. J.; Ebigbo, A.; Spangler, L. H. Abandoned Well CO₂ Leakage Mitigation Using Biologically Induced Mineralization: Current Progress and Future Directions. *Greenh. Gases Sci. Technol.* **2013**, *3* (1), 40–49. <https://doi.org/10.1002/ghg.1331>.
- (100) Hommel, J.; Lauchnor, E.; Phillips, A.; Gerlach, R.; Cunningham, A. B.; Helmig, R.; Ebigbo, A.; Class, H. A Revised Model for Microbially Induced Calcite Precipitation: Improvements and New Insights Based on Recent Experiments. *Water Resour. Res.* **2015**, *51* (5), 3695–3715. <https://doi.org/10.1002/2014WR016503>.
- (101) Ashraf, W.; Olek, J.; Jain, J. Microscopic Features of Non-Hydraulic Calcium Silicate Cement Paste and Mortar. *Cem. Concr. Res.* **2017**, *100*, 361–372. <https://doi.org/10.1016/J.CEMCONRES.2017.07.001>.
- (102) Plattenberger, D. A.; Ling, F. T.; Tao, Z.; Peters, C. A.; Clarens, A. F. Calcium Silicate Crystal Structure Impacts Reactivity with CO₂ and Precipitate Chemistry. *Environ. Sci. Technol. Lett.* **2018**, *5* (9), 558–563. <https://doi.org/10.1021/acs.estlett.8b00386>.
- (103) Richardson, I. G. The Calcium Silicate Hydrates. *Cem. Concr. Res.* **2008**, *38* (2), 137–158. <https://doi.org/10.1016/J.CEMCONRES.2007.11.005>.
- (104) Kaprálik, I.; Števíla, L.; Petrovič, J.; Hanic, F. Study of the System CaO-SiO₂-CO₂-H₂O in Relation to Scawtite under Hydrothermal Conditions. *Cem. Concr. Res.* **1984**, *14* (6), 866–872. [https://doi.org/10.1016/0008-8846\(84\)90013-9](https://doi.org/10.1016/0008-8846(84)90013-9).
- (105) Gislason, S. R.; Wolff-Boenisch, D.; Stefansson, A.; Oelkers, E. H.; Gunnlaugsson, E.; Sigurdardottir, H.; Sigfusson, B.; Broecker, W. S.; Matter, J. M.; Stute, M.; et al. Mineral Sequestration of Carbon Dioxide in Basalt: A Pre-Injection Overview of the CarbFix Project. *Int. J. Greenh. Gas Control* **2010**, *4* (3), 537–545. <https://doi.org/10.1016/J.IJGGC.2009.11.013>.
- (106) Huet, B.; L'Hostis, V.; Miserque, F.; Idrissi, H. Electrochemical Behavior of Mild Steel in Concrete: Influence of PH and Carbonate Content of Concrete Pore Solution. *Electrochim. Acta* **2005**, *51* (1), 172–180. <https://doi.org/10.1016/J.ELECTACTA.2005.04.014>.
- (107) Lauchnor, E. G.; Schultz, L. N.; Bugni, S.; Mitchell, A. C.; Cunningham, A. B.; Gerlach, R. Bacterially Induced Calcium Carbonate Precipitation and Strontium Coprecipitation in a Porous Media Flow System. *Environ. Sci. Technol.* **2013**, *47* (3), 1557–1564.

- <https://doi.org/10.1021/es304240y>.
- (108) Tanikawa, W.; Shimamoto, T. Comparison of Klinkenberg-Corrected Gas Permeability and Water Permeability in Sedimentary Rocks. *Int. J. Rock Mech. Min. Sci.* **2009**, *46* (2), 229–238. <https://doi.org/10.1016/J.IJRMMS.2008.03.004>.
- (109) Lanzirotti, A.; Newville, M.; Manoukian, L.; Lange, K. High-Speed, Coupled Micro-Beam XRD/XRF/XAFS Mapping at GSECARS: APS Beamline 13-ID-E. *Clay Clay Miner.* **2016**, *21*, 53–64. <https://doi.org/10.1346/CMS-WLS-21.5>.
- (110) Newville, M. Larch: An Analysis Package for XAFS and Related Spectroscopies. *J. Phys. Conf. Ser.* **2013**, *430* (1), 012007. <https://doi.org/10.1088/1742-6596/430/1/012007>.
- (111) Zhang, C.; Dehoff, K.; Hess, N.; Oostrom, M.; Wietsma, T. W.; Valocchi, A. J.; Fouke, B. W.; Werth, C. J. Pore-Scale Study of Transverse Mixing Induced CaCO₃ Precipitation and Permeability Reduction in a Model Subsurface Sedimentary System. *Environ. Sci. Technol.* **2010**, *44* (20), 7833–7838. <https://doi.org/10.1021/es1019788>.
- (112) Min, Y.; Kim, D.; Jun, Y.-S. Effects of Na⁺ and K⁺ Exchange in Interlayers on Biotite Dissolution under High-Temperature and High-CO₂-Pressure Conditions. *Environ. Sci. Technol.* **2018**, *52* (22), 13638–13646. <https://doi.org/10.1021/acs.est.8b04623>.
- (113) O'Connor, W. K.; Dahlin, D. C.; Rush, G. E.; Gerdemann, S. J.; Penner, L. R.; Nilsen, D. N. *Aqueous Mineral Carbonation: Mineral Availability, Pretreatment, Reaction Parametrics, and Process Studies*; 2005. <https://doi.org/10.13140/RG.2.2.23658.31684>.
- (114) Davis, S. J.; Lewis, N. S.; Shaner, M.; Aggarwal, S.; Arent, D.; Azevedo, I. L.; Benson, S. M.; Bradley, T.; Brouwer, J.; Chiang, Y.-M.; et al. Net-Zero Emissions Energy Systems. *Science* (80-.). **2018**, *360* (6396), eaas9793. <https://doi.org/10.1126/science.aas9793>.
- (115) IPCC. *Climate Change 2014: Synthesis Report. Contribution of Working Groups I, II and III to the Fifth Assessment Report of the Intergovernmental Panel on Climate Change*; Geneva, Switzerland, 2014.
- (116) Bataille, C.; Åhman, M.; Neuhoff, K.; Nilsson, L. J.; Fishedick, M.; Lechtenböhmer, S.; Solano-Rodriguez, B.; Denis-Ryan, A.; Stiebert, S.; Waisman, H.; et al. A Review of Technology and Policy Deep Decarbonization Pathway Options for Making Energy-Intensive Industry Production Consistent with the Paris Agreement. *Journal of Cleaner Production*. Elsevier June 20, 2018, pp 960–973. <https://doi.org/10.1016/j.jclepro.2018.03.107>.
- (117) Worrell, E.; Price, L.; Martin, N.; Hendriks, C.; Meida, L. O. Carbon Dioxide Emissions From the Global Cement Industry. *Annu. Rev. Energy Environ.* **2001**, *26* (1), 303–329. <https://doi.org/10.1146/annurev.energy.26.1.303>.
- (118) Kajaste, R.; Hurme, M. Cement Industry Greenhouse Gas Emissions – Management Options and Abatement Cost. *J. Clean. Prod.* **2016**, *112*, 4041–4052. <https://doi.org/10.1016/J.JCLEPRO.2015.07.055>.
- (119) Marceau, M. L.; Nisbet, M. A.; Vangeem, M. G. *Life Cycle Inventory of Portland Cement Manufacture*; Skokie, Illinois, 2006.
- (120) IEA. *Energy Technology Perspectives 2012: Pathways to a Clean Energy System*; 2012.
- (121) Barcelo, L.; Kline, J.; Walenta, G.; Gartner, E. Cement and Carbon Emissions. *Mater. structures* **2014**, *47* (6), 1055–1065.
- (122) Abdolhosseini Qomi, M. J.; Krakowiak, K. J.; Bauchy, M.; Stewart, K. L.; Shahsavari, R.; Jagannathan, D.; Brommer, D. B.; Baronnet, A.; Buehler, M. J.; Yip, S.; et al. Combinatorial Molecular Optimization of Cement Hydrates. *Nat. Commun.* **2014**, *5*, 4960.
- (123) Müller, H. S.; Haist, M.; Vogel, M. Assessment of the Sustainability Potential of Concrete

- and Concrete Structures Considering Their Environmental Impact, Performance and Lifetime. *Constr. Build. Mater.* **2014**, *67*, 321–337.
<https://doi.org/10.1016/J.CONBUILDMAT.2014.01.039>.
- (124) Ben-Yair, M. The Durability of Cement and Concrete in Sea Water. *Desalination* **1967**, *3* (2), 147–154.
- (125) Glasser, F. P.; Marchand, J.; Samson, E. Durability of Concrete - Degradation Phenomena Involving Detrimental Chemical Reactions. *Cem. Concr. Res.* **2008**, *38* (2), 226–246.
<https://doi.org/10.1016/j.cemconres.2007.09.015>.
- (126) Naik, T. R.; Kumar, R. *Concrete Structures for 1000 Years of Lifespan-Part I*; 2003.
- (127) Ashraf, W.; Olek, J. Carbonation Behavior of Hydraulic and Non-Hydraulic Calcium Silicates: Potential of Utilizing Low-Lime Calcium Silicates in Cement-Based Materials. *J. Mater. Sci.* **2016**, *51* (13), 6173–6191. <https://doi.org/10.1007/s10853-016-9909-4>.
- (128) Plattenberger, D. A.; Ling, F. T.; Peters, C. A.; Clarens, A. F. Targeted Permeability Control in the Subsurface via Calcium Silicate Carbonation. *Environ. Sci. Technol.* **2019**, *53* (12), 7136–7144. <https://doi.org/10.1021/acs.est.9b00707>.
- (129) Panagiotopoulou, C.; Tsivilis, S.; Kakali, G. Application of the Taguchi Approach for the Composition Optimization of Alkali Activated Fly Ash Binders. *Constr. Build. Mater.* **2015**, *91*, 17–22. <https://doi.org/10.1016/J.CONBUILDMAT.2015.05.005>.
- (130) ASTM International. ASTM C109/C109M-16a Standard Test Method for Compressive Strength of Hydraulic Cement Mortars (Using 2-in. or [50-Mm] Cube Specimens). West Conshohocken, PA 2016.
- (131) ASTM International. ASTM C270-19a Standard Specification for Mortar for Unit Masonry. West Conshohocken, PA 2019.
- (132) Lu, X.; Li, C.; Zhang, H. Relationship between the Free and Total Chloride Diffusivity in Concrete. *Cem. Concr. Res.* **2002**, *32* (2), 323–326. [https://doi.org/10.1016/S0008-8846\(01\)00664-0](https://doi.org/10.1016/S0008-8846(01)00664-0).
- (133) U.S. Energy Information Administration (EIA). Carbon Dioxide Emissions Coefficients. 2016.
- (134) Taro, Y.; Fumiko, S. Method of Making Pseudowollastonite Clinker with the Rotary Kiln, November 30, 1966.
- (135) Nisbet, M. A.; Marceau, M. L.; Vangeem, M. G. *Environmental Life Cycle Inventory of Portland Cement Concrete*; 2002.
- (136) Iglauer, S.; Sarmadivaleh, M.; Al-Yaseri, A.; Lebedev, M. Permeability Evolution in Sandstone Due to Injection of CO₂-Saturated Brine or Supercritical CO₂ at Reservoir Conditions. *Energy Procedia* **2014**, *63*, 3051–3059.
<https://doi.org/10.1016/J.EGYPRO.2014.11.328>.
- (137) Huerta, N. J.; Hesse, M. A.; Bryant, S. L.; Strazisar, B. R.; Lopano, C. Reactive Transport of CO₂-Saturated Water in a Cement Fracture: Application to Wellbore Leakage during Geologic CO₂ Storage. *Int. J. Greenh. Gas Control* **2016**, *44*, 276–289.
<https://doi.org/10.1016/J.IJGGC.2015.02.006>.
- (138) Lisabeth, H.; Zhu, W.; Xing, T.; De Andrade, V. Dissolution-Assisted Pattern Formation During Olivine Carbonation. <https://doi.org/10.1002/2017GL074393>.
- (139) Cao, P.; Karpyn, Z. T.; Li, L. Self-Healing of Cement Fractures under Dynamic Flow of CO₂-Rich Brine. <https://doi.org/10.1002/2014WR016162>.
- (140) Sebag, D.; Verrecchia, E. ; Lee, S.-J.; Durand, A. The Natural Hydrous Sodium Silicates from the Northern Bank of Lake Chad: Occurrence, Petrology and Genesis. *Sediment.*

- Geol.* **2001**, *139* (1), 15–31. [https://doi.org/10.1016/S0037-0738\(00\)00152-4](https://doi.org/10.1016/S0037-0738(00)00152-4).
- (141) Zhang, Y.-Q.; Radha, A. V.; Navrotsky, A. Thermochemistry of Two Calcium Silicate Carbonate Minerals: Scawtite, $\text{Ca}_7(\text{Si}_6\text{O}_{18})(\text{CO}_3)\cdot 2\text{H}_2\text{O}$, and Spurrite, $\text{Ca}_5(\text{SiO}_4)_2(\text{CO}_3)$. *Geochim. Cosmochim. Acta* **2013**, *115*, 92–99. <https://doi.org/10.1016/J.GCA.2013.03.031>.
- (142) Mostafa, N. Y.; Shaltout, A. A.; Omar, H.; Abo-El-Enein, S. A. Hydrothermal Synthesis and Characterization of Aluminium and Sulfate Substituted 1.1 Nm Tobermorites. *J. Alloys Compd.* **2009**, *467* (1–2), 332–337. <https://doi.org/10.1016/J.JALLCOM.2007.11.130>.
- (143) ASTM International. ASTM C1329/C1329M-16a Standard Specification for Mortar Cement. West Conshohocken, PA 2016.

Appendix I: Supporting Information for Chapter 3 - Targeted Permeability Control in the Subsurface Via Calcium Silicate Carbonation

Dan Plattenberger,[†] Florence T. Ling,[‡] Catherine Peters,[‡] and Andres Clarens^{*†}

[†]Engineering Systems and Environment, University of Virginia, Charlottesville, Virginia 22904, United States

[‡]Civil and Environmental Engineering, Princeton University, Princeton, New Jersey 08544, United States

*Corresponding author: Andres Clarens (andres@virginia.edu)

A1.1. Column Setup and Pseudowollastonite Injection

Figure A1.1 illustrates how sand columns were injected with pseudowollastonite by (a) placing the stainless-steel columns in a custom press and passing a suspension of pseudowollastonite powder in water through the columns, which (b) were capped on each end with stainless-steel mesh. (c) After injection, pseudowollastonite appeared to be uniformly distributed throughout the columns upon visual inspection.

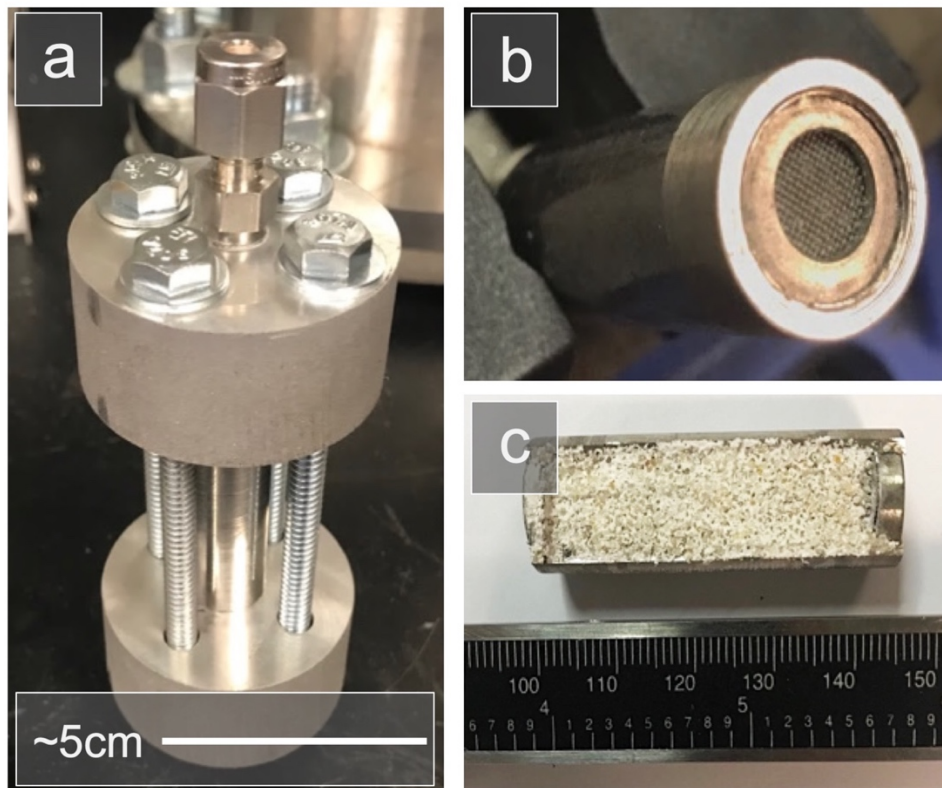


Figure A1.1. Column Setup and Injection (a) Pseudowollastonite powder, suspended in water, was injected at high pressure (10 MPa) into sand-packed columns in a custom-machined holder. (b) On each end of the columns are stainless-steel washers and mesh. (c) After injection, an even distribution of pseudowollastonite along the length of the columns was observed. The ruler in (c) shows mm.

We were interested in studying the behavior of diffusion-limited reactions because they differ from flow-through or stirred reactions in terms of solid:water ratios and geochemical gradients, which we believe are also representative and relevant to a variety of subsurface applications. In addition, flow-through reactions can present complex and confounding results that diffusion-limited reactions avoid. For example, work done by Iglauer et al.¹³⁶ showed that the injection of scCO₂ alone into Berea sandstone caused a permeability reduction of up to 35% due to structural changes in the sandstone matrix. Flow-through work involving CO₂-saturated water and wellbore fractures found that holding flow constant led to no decrease in permeability while holding pressure potential constant led to a progressive reduction in fluid flux and self-limiting flow.¹³⁷ Work by Lisabeth et al.¹³⁸ found a chemo-mechanical coupling in olivine and pyroxene-bearing rocks that decreased porosity of pores but maintained permeability of the rock due to channelized dissolution from the flowing CO₂-rich fluid and work done by Cao et al.¹³⁹ found that the residence time of CO₂-rich brine had a profound effect on mineral precipitation.

While changes in pressure, humidity, saturation of dissolved species, and temperature associated with ending the experiments could potentially induce precipitation of any of the phases seen in this work, it is also probable that the precipitation was induced via environmental changes during the reaction period, such as pH changes due to dissolution and carbonate diffusion. For example, Ma et al.⁵⁷ hydrothermally synthesized sheet-like sodium silicates and Sebag et al.¹⁴⁰ reviewed the literature and suggested that a change in pH is a known method for supersaturation and precipitation of such phases. Likewise, Zhang et al.¹⁴¹ hydrothermally synthesized scawtite, a calcium silicate carbonate, and many, including Mostafa et al.¹⁴² have hydrothermally synthesized calcium silicate hydrates like tobermorite and xonotlite, which we believe are similar to the CSH phases presented here.

A1.2. Permeability Measurements

An air mass flow meter [0 – 405 sccm (Concoa)] was coupled with pressure gauges [0-0.034 MPa (Dwyer), 0-0.21 MPa (Concoa), 0-1.38 MPa (Concoa), 0-3.45 MPa (Concoa)] and measurements were taken at five flow rates and pressures for each column. The flow rates were plotted against the pressure differentials to ensure that the measurements were within the laminar flow regime (linear relationship) and the average of five measurements was reported.

A1.3. Synchrotron μ XRF/ μ XRD Parameters

The 13IDE beamline is a hard X-ray microprobe incident with a focused spot size of $\sim 1 \times 2 \mu\text{m}$. A 4-element silicon drift diode detector (Vortex ME4) was used for collecting XRF spectra with an incident energy of 18 keV. For XRF mapping, scans were conducted at 20 μm steps with dwell times of 20 ms. XRD was collected on a Perkin Elmer XRD1621 digital flat panel detector, with scans conducted at 2 μm steps with dwell times of 100 ms.

A1.4. Diffusion Map for 96 hr CO₂ Column

The CO₂ (and the CO₂ + NaOH) columns that were reacted under 1.1 MPa CO₂ for 96 hr showed a significant Br concentration deep in the columns as shown in Figure A1.2, which was collected from the inlet to 16 mm of one column.

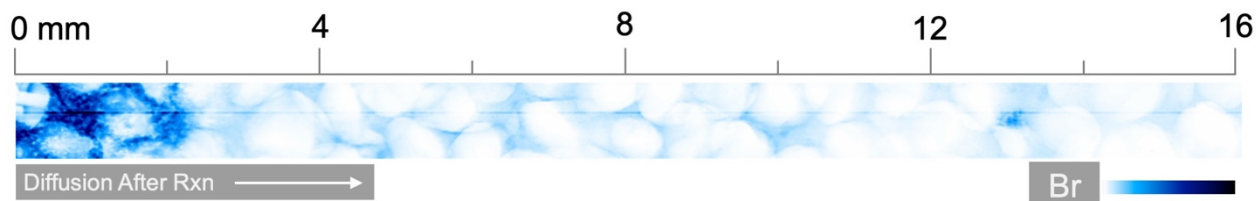


Figure A1.2. Br Diffusion of 96 hr Column. Bromine diffusion after a 96-hr CO_2 -only reaction period shows high diffusivity of water, likely due to the limited quantity of precipitates (CaCO_3 and SiO_2) in that reaction period.

A1.5. Dissolving Front

Synchrotron μXRF mapping of Sr in CO_2 only columns (Figure A1.3a) shows that CaCO_3 (here, Sr coprecipitates with Ca) precipitates uniformly orthogonal to the direction of diffusion at 96 hr of reaction time but low pH (from dissolved carbonate) causes the CaCO_3 to dissolve over time and progress deeper into the column, leaving behind relatively empty pore space. After reaction, injected epoxy filled that pore space and could be easily identified from low-magnification SEM (Figure A1.3b).

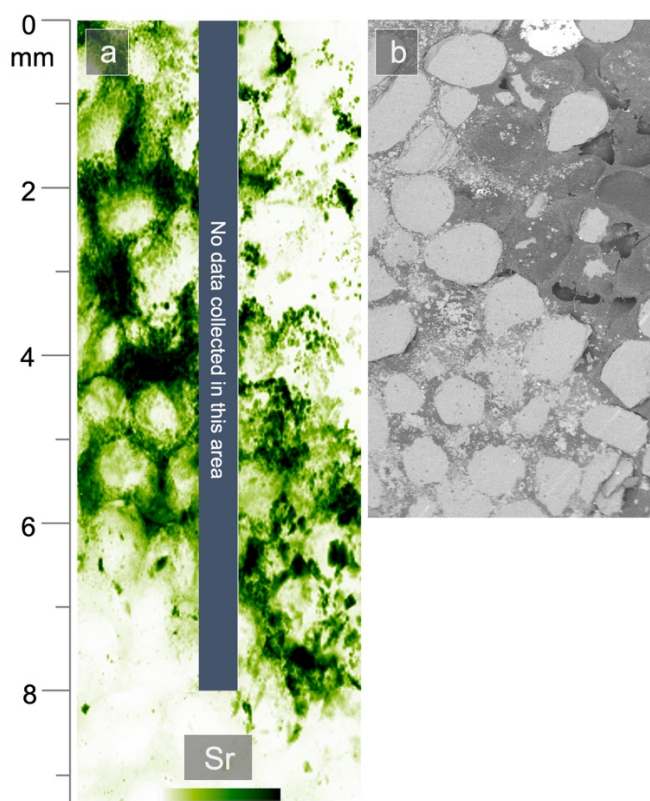


Figure A1.3. Dissolving Carbonate Front (a) Strontium μXRD mapping shows a non-uniform distribution of solid carbonates orthogonal to the direction of diffusion (which was from top to bottom). The upper righthand portion of the map showed little Sr (and Ca) compared to the rest of the map. (b) Comparing the same location in SEM, it is evident that the pores in the dissolved region filled with epoxy, which appears as darker gray in the micrograph. Both (a) and (b) share a common scale and are from the same location.

A1.6. Effect of CO₂ Pressure on CCSH Formation in CO₂ + NaOH Columns

When NaOH was present, increasing the pressure of CO₂ to 3.4 and 15.5 MPa increased the concentration of CCSH phases near the inlet of columns, as shown in Figure A1.4 and dramatically decreased air permeability, even in 24 hr of reaction.

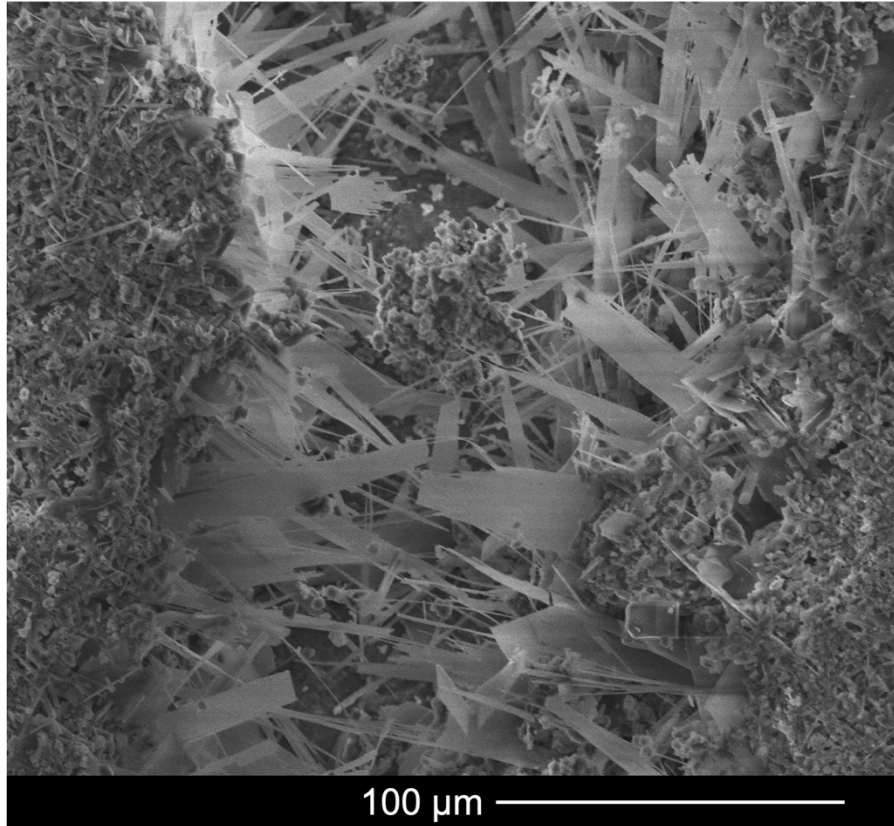


Figure A1.4. Impact of Pressure on CCSH Formation. SEM micrograph of the inlet of a column reacted for 24 hr in 0.1 M NaOH and 3.4 MPa CO₂, showing an abundance of CCSH phases.

A1.7. Impacts of Acid Washing on Carbonate and CCSH Precipitates

Acid washing both CO₂ and CO₂ + NaOH columns had observably different impacts on permeability, which we attribute to the differences in acid stability of carbonate and CCSH phases, which predominate in each, respectively. In Figure A1.5, SEM micrographs of column inlets are shown for CO₂ columns that were submerged in either (a) deionized water or (b) pH 4.5 sodium acetate/acetic acid solutions for 16 hr. The DI water column shows an abundance of Ca-carbonate and SiO₂ while the acid-washed column shows nearly all SiO₂ near the inlet. Micrographs (c) and (d) show the same conditions for CO₂ + NaOH columns but each shows an abundance of CCSH phases (based on visual impressions), indicating that the acid treatment did not significantly dissolve those phases.

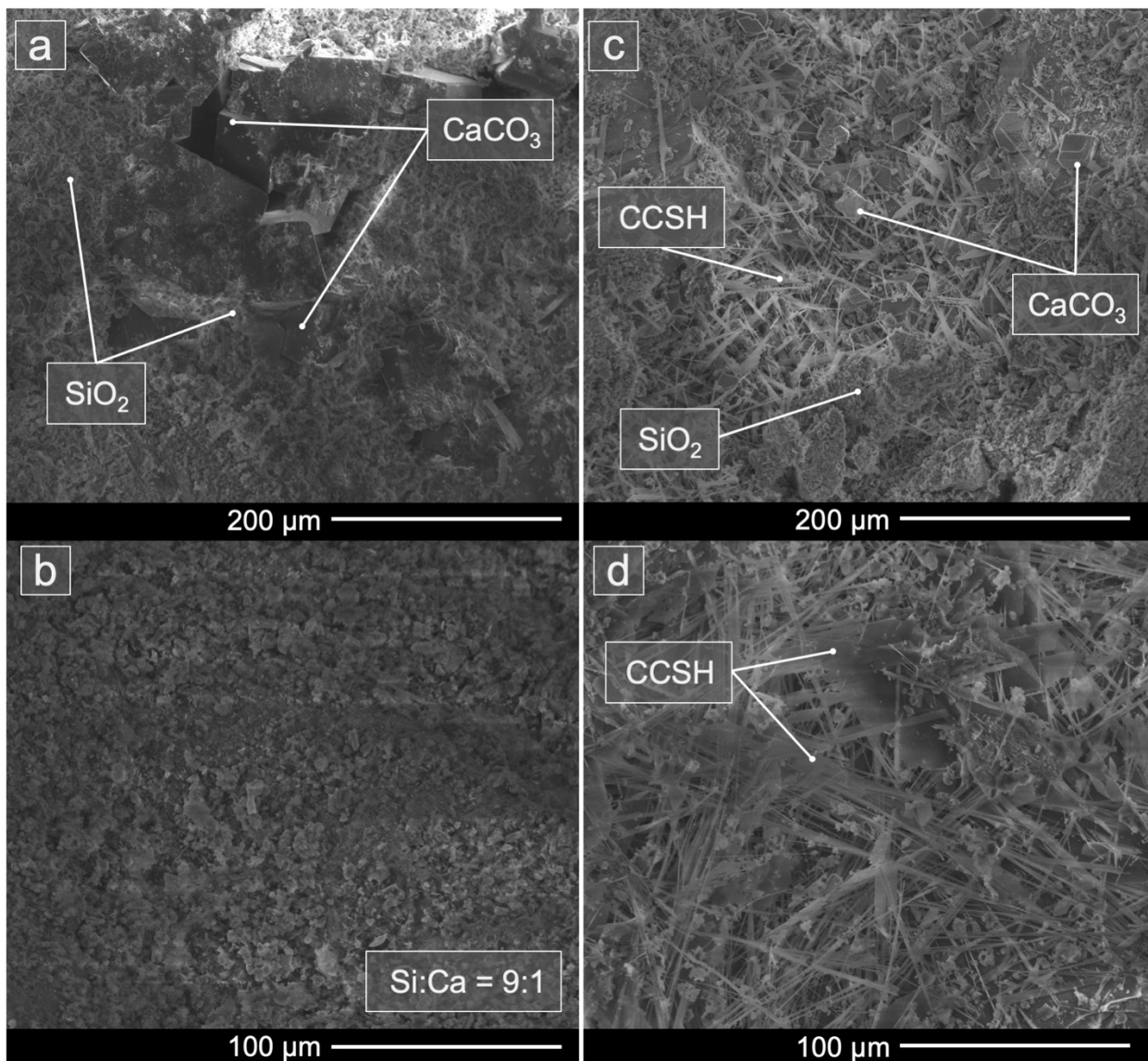


Figure A1.5. Impacts of Acid Treatment. (a) Ca-carbonate and SiO₂ were abundant near the inlet of a CO₂ column that was reacted for 72 hr in 3.4 MPa CO₂ and subsequently submerged in deionized water for 16 hr. (b) Conversely, a column reacted under the same conditions and submerged in pH 4.5 sodium acetate/acetic acid for 16 hr showed nearly no Ca-carbonate and a significant amount of SiO₂. (c,d) Columns that were reacted and treated under the same conditions but with 0.1 M NaOH yielded an abundance of CCSH phases that remained after acid treatment.

A1.8. Effect of Temperature on CCSH Formation

Small-scale powder batch experiments showed that CCSH phases could form, sometimes at smaller scales, at temperatures as low as 75 °C in 24 hr. Temperatures below 75 °C were not tested.

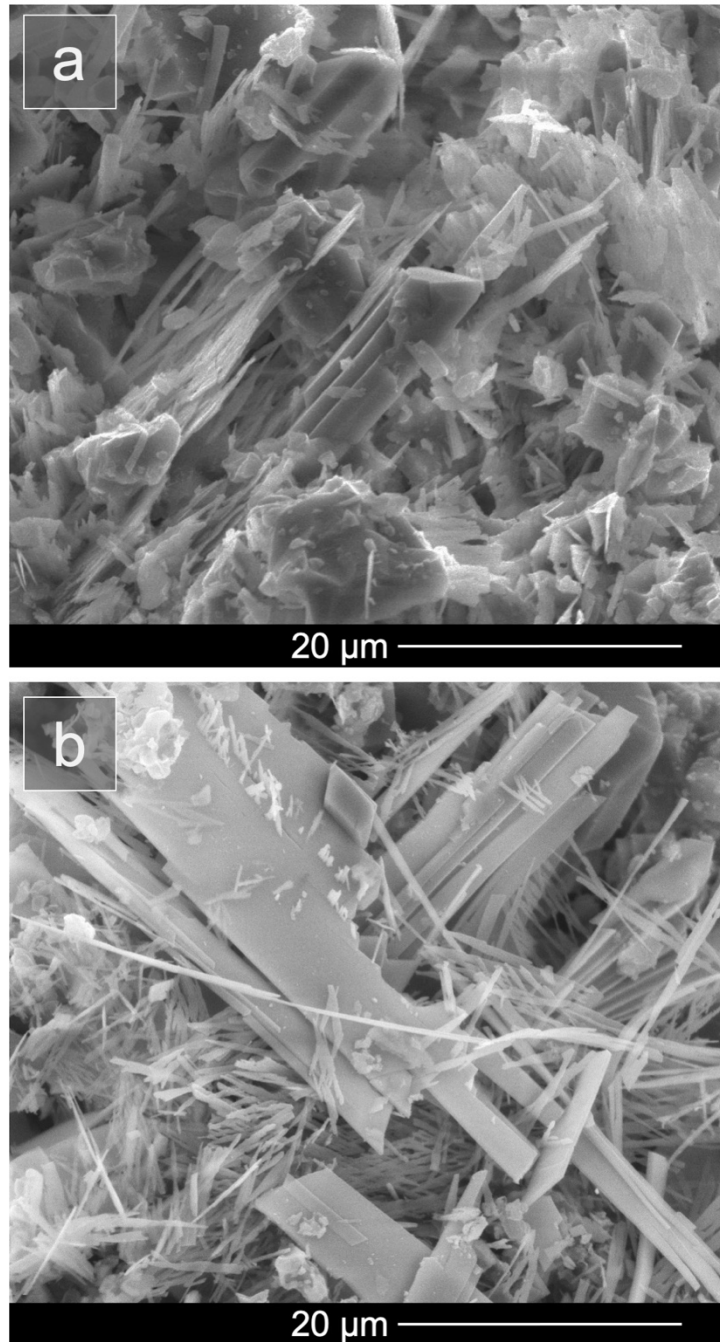


Figure A1.6. Impact of Temperature on CCSH Formation. (a) CCSH phases appeared smaller and Ca-carbonate predominated at 75 °C (in 24 hr), compared to CCSH phases that formed in (b) temperatures between 110 – 150 °C. There were no observed differences in elemental composition of CCSH phases formed at the various temperatures.

A1.9. TEM Analyses of CCSH Phases

TEM-SAED analyses of numerous CCSH phases (a representative selection is shown in Figure A1.7) showed that each was (highly) crystalline but had a distinctive diffraction pattern. Likewise, the Si:Ca ratio was highly variable, just as observed via SEM-EDS in Figure 3.8 in the main text.

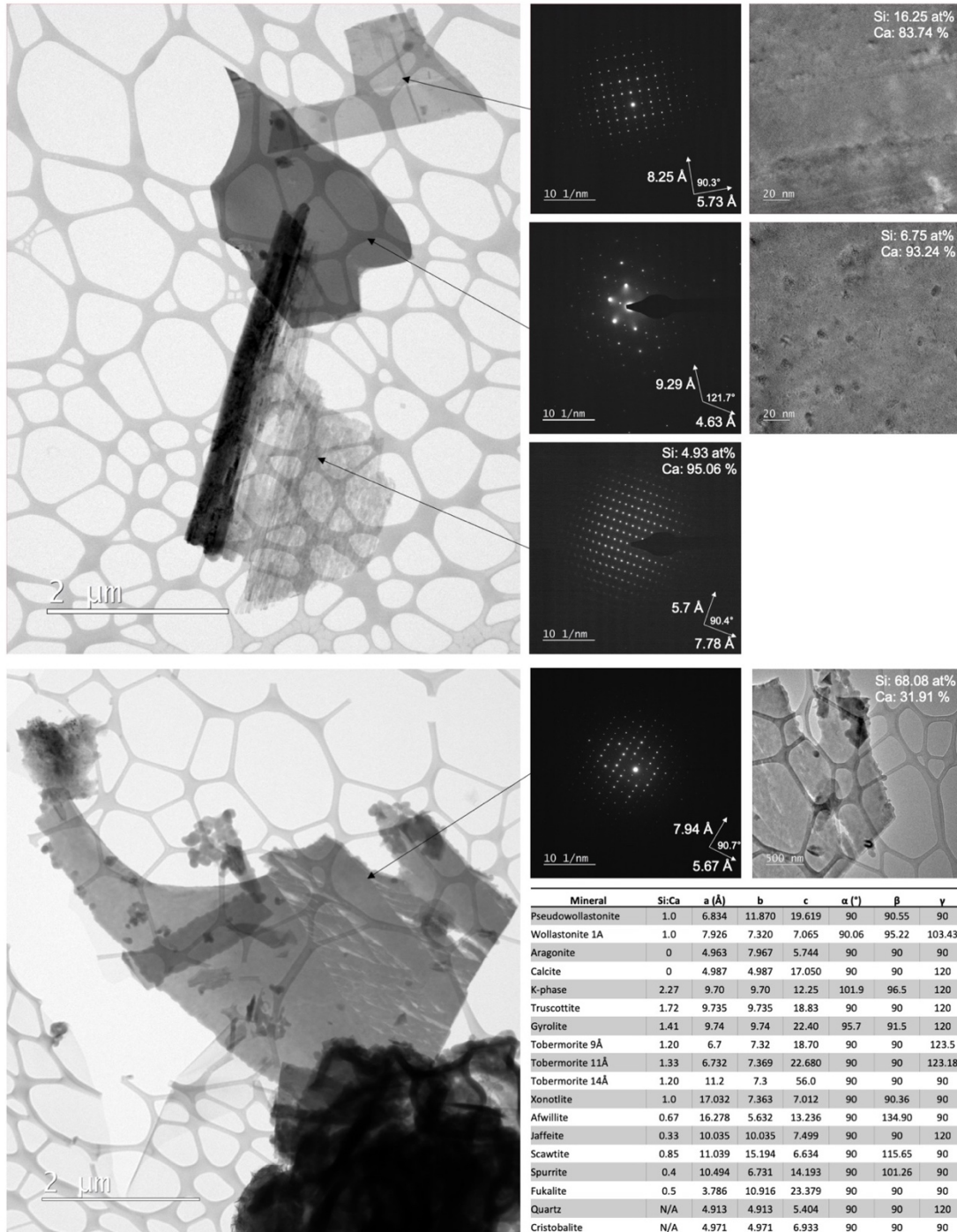


Figure A1.7. TEM Analyses of CCSH Phases. TEM micrographs show some of the high-resolution variability among various CCSH samples, all from the same experiment, reacted for 24 hr in 0.1 M NaOH and 1.1 MPa CO₂. Similarly, while a selection of SAED patterns show bright spots, indicative of crystallinity, each was quite dissimilar and none could be matched to known reference patterns, some of which are provided in the table.

A1.10. XRD Analysis of CCSH Batch Experiment

Bulk X-ray diffraction data was collected (PANalytical Empyrean diffractometer) on a batch powder sample that was reacted for seven days with 0.1 M NaOH and 1.1 MPa CO₂ at 150 °C as described in section 2.2. The diffraction pattern, shown in Figure A1.7 suggests aragonite and calcite may have formed and quartz may have also been present, although sand was present in the experiment and may not have been fully removed after the reaction period. As illustrated in Figure 3.8 of the main text and A1.7 of Appendix I, each CCSH plate appears to be unique, both in terms of its elemental composition as well as its crystal structure. Because the plates are heterogeneous, and therefore provide different diffraction patterns, bulk XRD analyses are unable to provide enough detail to identify the CCSH phases in this work.

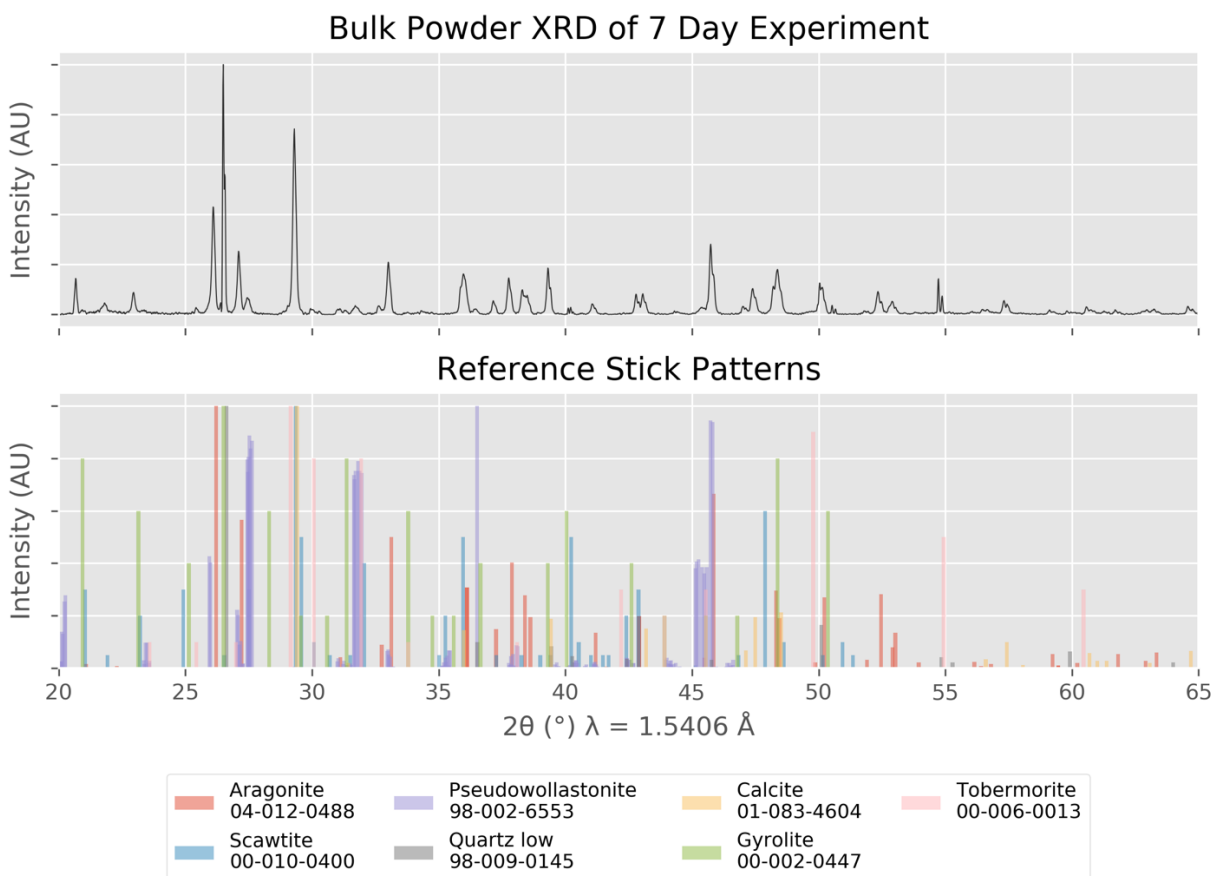


Figure A1.8. Bulk Powder XRD. Pseudowollastonite powders reacted for seven days at 150 °C with 0.1 M NaOH and 1.1 MPa CO₂ compared to select candidate stick patterns showing complexity of bulk XRD identification of CCSH phases.

Synchrotron μ XRD likewise presents similar issues in identification as it appears that aragonite is a predominate phase and others are much more difficult to identify, particularly because many calcium silicate (carbonate) hydrates share common peaks and share peaks with aragonite and quartz (in particular, Tobermorite). SEM, EDS, and TEM data, taken together, suggest that the plate-like phases shown in Figure A1.9 (and Figure 3.5 of the main text) are not simply aragonite or quartz.

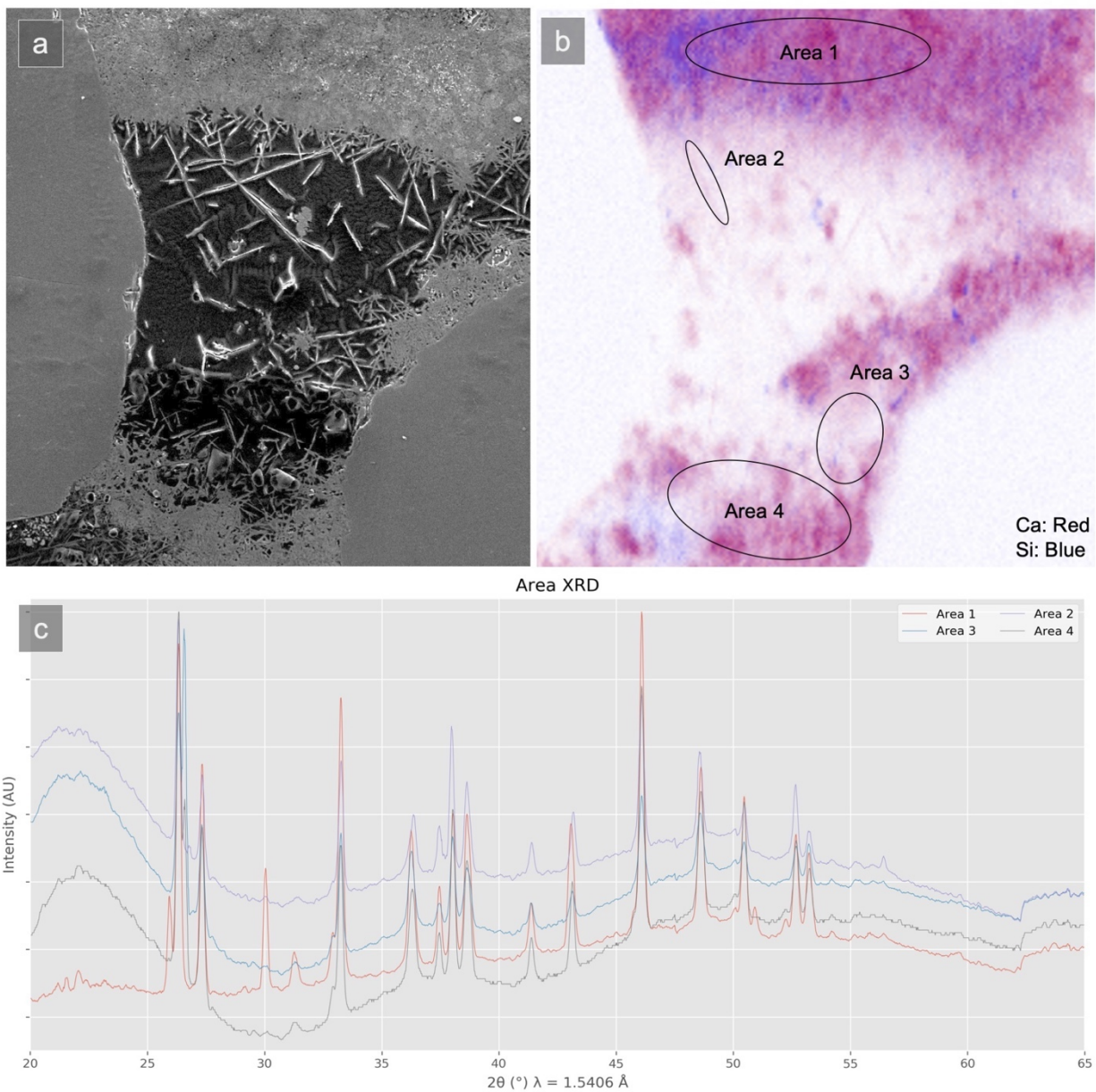


Figure A1.9. Selected Area Synchrotron XRD Patterns. (a) From the same location as Figure 3.5b (b) XRD patterns were collected from selected areas and (c) plotted to show the similarities and differences among the patterns. In particular 30° 2θ shows a different peak from Area 1 compared to the other areas.

Appendix II: Supporting Information for Chapter 4 - Formation of Low-Carbon Crystalline Cement via Calcium Silicate Carbonation

Dan A. Plattenberger,[†] Elizabeth J. Opila,[‡] Rouzbeh Shahsavari,[§] and Andres F. Clarens^{*†}

[†]Engineering Systems and Environment, University of Virginia, Charlottesville, Virginia 22904, United States

[‡]Materials Science and Engineering, University of Virginia, Charlottesville, Virginia 22904, United States

[§]C-Crete Technologies, Stafford, Texas 77477, United States

A2.1. X-ray Diffraction of Pseudowollastonite

The diffraction pattern for the pseudowollastonite used in this work is presented in Figure A2.1. The data were collected via a Panalytical X'pert Pro diffractometer with a copper source ($K\alpha = 1.5406 \text{ \AA}$) from $15 - 65^\circ 2\theta$ with a 0.004° step size and 117 ms per step. Analysis via Panalytical HighScore Plus with PDF-4+ 2019 database confirmed an excellent match for pseudowollastonite and is the source for the peak identifiers in Figure A2.1.

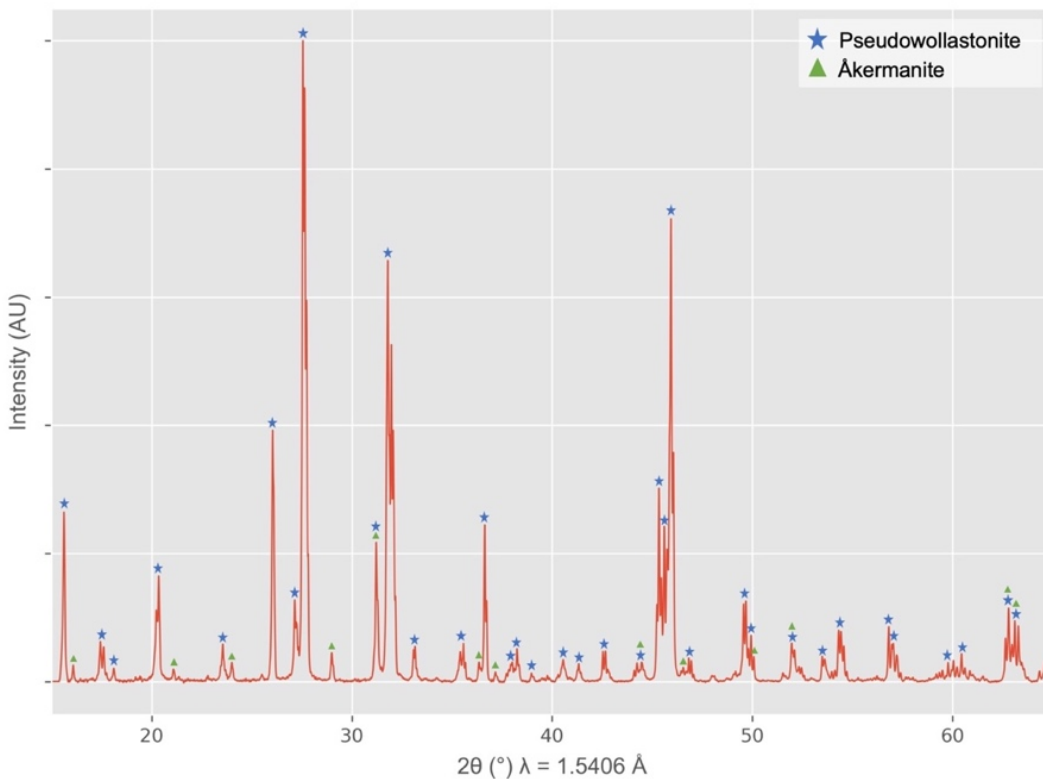


Figure A2.2. X-ray diffraction pattern for pseudowollastonite used in this work.

A2.2. Taguchi Designs

The Taguchi design of experiments is frequently used in cement research to determine mix proportions, additives, or curing conditions to optimize for some metric such as strength, ductility, or others. It differs from traditional factorial design of experiments in that it does not evaluate

every possible combination of factors. Rather, it utilizes orthogonal (balanced) arrays to determine the relative influence of the factors in the array. This design allows for robust testing of a wider range of variables with fewer samples than factorial designs. Coupled with Analysis of Variance (ANOVA), the relative contributions of the factors to the desired outcome (in this case, highest compressive strength) may be determined. Here, chose to test five factors at three different levels, as shown in the Taguchi matrix, Table A2.1.

Table A2.1. Experimental conditions for the five-factor, three-level Taguchi design of experiments, used to optimize mortar curing chemistry.

Factors	Levels		
	1	2	3
A. pH during dry curing	6	6.5	6.9
B. pCO ₂ during dry curing (MPa)	0.55	0.76	0.97
C. pH during wet curing	6	6.5	6.9
D. pCO ₂ during wet curing (MPa)	0.55	0.76	0.97
E. Temp. during wet curing (°C)	75	110	140

Table A2.2. The Taguchi design of experiments for curing parameters and average compressive strength results from three specimens for each run.

Run #	A	B	C	D	E	Compressive Strength (MPa)
1	1	1	1	1	1	8.1
2	1	2	2	2	2	6.6
3	1	3	3	3	3	7.7
4	2	1	1	2	2	8.4
5	2	2	2	3	3	10.2
6	2	3	3	1	1	5.8
7	3	1	2	1	3	8.0
8	3	2	3	2	1	7.8
9	3	3	1	3	2	6.7
10	1	1	3	3	2	6.2
11	1	2	1	1	3	8.5
12	1	3	2	2	1	6.2
13	2	1	2	3	1	9.0
14	2	2	3	1	2	8.4
15	2	3	1	2	3	8.3
16	3	1	3	2	3	7.3
17	3	2	1	3	1	4.9
18	3	3	2	1	2	5.6

Analysis of the data presented in Table A2.2 is performed first by averaging the compressive strengths for all specimens at each of the three levels for each of the five factors. For example, the average strength from Runs 1, 2, 3, 10, 11, 12 was compared to that from Runs 4, 5, 6, 13, 14, 15 and to that from Runs 7, 8, 9, 16, 17, 18 to establish the optimal curing conditions for factor A, pH during the dry curing phase. This analysis was repeated for each of the factors to determine the optimal conditions (of those tested here), which are highlighted with blue text in Table A2.2. After this analysis, which focused on the chemistry of curing, we performed another smaller Taguchi design to optimize for physical mix parameters, shown in Table A2.3. Standard ASTM graded testing sand ('graded') was compared to a 50-50 mix of graded sand with ASTM 20-30 sand ('20-30'), which is comprised exclusively of 841 – 595 μm sand. That mixture is often used to test mortars with sand that is likely more representative of field or industrial conditions, per ASTM C1329.¹⁴³ The cement-to-sand proportions and the water-to-cement proportions are also common factors to test for any mortar because they are known to have significant impacts on physical performance, like strength. Table A2.4 gives the design of the matrix as well as compressive strengths for 3 specimens for each run. The optimum parameters from this Taguchi design are shown in blue in Table A2.3. The carbonate specimen in Table A2.4 was done following run #2 parameters but without any NaOH to buffer pH.

Table A2.3. Experimental conditions for the three-factor, two-level Taguchi design of experiments, used to optimize mortar mix proportions.

Factors	Levels	
	1	2
A. Sand grading	Graded/20-30	Graded
B. Cement : Sand	1:3	1:2.75
C. Water : Cement	.45	.4

Table A2.4. The Taguchi design of experiments for physical parameters and average compressive strength results from three specimens for each run.

Run #	A	B	C	Compressive Strength (MPa)
1	1	1	1	8.3
2	1	2	2	13.6
3	2	1	2	8.6
4	2	2	1	6.3
Carbonate	1	2	2	8.4

A2.3. Lifecycle Analyses

This section serves to show the tabulation and references^{3,119,133,135} for the lifecycle analyses that were discussed in detail in the main text and methods section. Table A2.5 is for the analysis of OPC while Table A2.6 is for the analysis of CESH-cements, via a production method that would most similarly follow the procedures we outlined throughout this work.

Table A2.5. Tabulation of the ordinary Portland Cement lifecycle analysis.

Ordinary Portland Cement

		Process/Factor	Value	Refer notes	CO2 Emissions (kg/tonne cement)	Refer notes	
Cement Production	Define	Concrete Quantity (tonnes)	1	Functional Unit			
		Cement Content (%)	0.14	1 part cement : 3 parts sand : 3 parts aggregate : 0.5 part water (and half is consumed)			
	Raw Materials	Limestone to make 1 tonne cement (tonnes)	1.41				
		Sand to make 1 tonne cement (tonnes)	0.139				
		Clay to make 1 tonne cement (tonnes)	0.034		Huntzinger and Eatmon	4	Marceau et al.
		Iron Ore to make 1 tonne cement (tonnes)	0.015				
		Gypsum to make 1 tonne cement (tonnes) - only in final grinding process	0.05				
		Transportation (kg/tonne cement)				7	Marceau et al.
	Pyroprocess	Clinker Temperature (C)	1450		Huntzinger and Eatmon		
		Coal energy for 1 tonne cement heating (GJ)	3.56			314.5	
		Fuel oil energy for 1 tonne cement (GJ)	0.764		Huntzinger and Eatmon	52.9	EIA emission factors
		Nat gas energy for 1 tonne cement (GJ)	0.764			38.4	
		Ratio of CO2 emissions to CaCO3	0.44		CaCO3 mass * (44/100) : the ratio of CO2 to CaCO3	620.0	Theoretical based on decomp.
	Finish Grinding and Blending	Coal energy for 1 tonne cement grinding (GJ)	0.355			31.4	
		Fuel oil energy for 1 tonne cement grinding (GJ)	0.076		Huntzinger and Eatmon	5.3	EIA emission factors
		Nat gas energy for 1 tonne cement grinding (GJ)	0.076			3.8	
Carbon Uptake	Carbon Uptake (% C in cured cement)	0			0.0		
Concrete Production	Aggregate, mix, and curing	Cement and aggregate transport to Concrete Facility (kg CO2 /m3 concrete)	9.47			3.95	
		Aggregate production (kg/m3 concrete)	3.86		Nisbet et al. Table 5-7A for Precast Mix 1	1.61	Assume density of concrete is 2400 kg/m3
		Concrete plant operations - mixing and curing (kg/m3 concrete)	14.2			5.92	
		Total CO2/tonne cement (kg)	1077	Total CO2/tonne concrete (kg)	160		

Table A2.6. Tabulation of the CESH-cement lifecycle analysis based on 7-day curing.

CESSH Cement - Current Production Scenario

		Process/Factor	Value	Refor notes	CO2 Emissions (kg/tonne cement)	Refor notes		
Cement Production	Define	Concrete Quantity (tonnes)	1	Functional Unit				
		Cement Content (%)	0.14	Assume the same as OPC				
	Raw Materials	CO2 in 1 tonne of cured cement (tonnes)	0.169					
		Limestone to make 1 tonne cement (tonnes)	0.72	The CaO and Silica do not sum to 1 tonne because CO2 is a significant constituent in cured cement. Assumes Silica fume is 100% SiO2		1.74	Since only limestone is being mined, this number is adjusted relative to all mining activity in OPC	
		Silica Fume to make 1 tonne cement (tonnes)	0.43					
		Iron Ore to make 1 tonne cement (tonnes)	0					
		Gypsum to make 1 tonne cement (tonnes) - only in final grinding process	0					
		Transportation (kg/tonne cement)	-		-			7
	Pyroprocess	Clinker Temperature (C)	1175		Empirical			
		Coal energy for 1 tonne cement heating (GJ)	2.40	Assumed the energy reqs are exactly linear to temperature, compared to OPC. Also scaled due to need for less CaO per tonne cement.	211.8			
		Fuel oil energy for 1 tonne cement (GJ)	0.51		35.6	EIA emission factors (Ref 4)		
		Nat gas energy for 1 tonne cement (GJ)	0.51		25.9			
		Ratio of CO2 emissions to CaCO3	0.44	CaCO3 mass * (44/100) : the ratio of CO2 to CaCO3	314.8	Theoretical based on decomp.		
	Finish Grinding and Blending	Coal energy for 1 tonne cement grinding (GJ)	0.29		26.1			
		Fuel oil energy for 1 tonne cement grinding (GJ)	0.06	Huntzinger and Eatmon 2006	4.4	EIA emission factors		
		Nat gas energy for 1 tonne cement grinding (GJ)	0.06		3.2			
Carbon Uptake	Carbon Uptake (% C in cured cement)	4.613	Empirical	-169.1	Based on empirical data			
Concrete Production	Aggregate, mix, and curing	Cement and aggregate transport to Concrete Facility (kg CO2 /m3 concrete)	9.47		3.95			
		Aggregate production (kg/m3 concrete)	3.86	Assume the same as OPC	1.61	Assume the same as OPC		
		Concrete plant operations - mixing and curing (kg/m3 concrete)	14.2		5.92			
		Total CO2/tonne cement (kg)	461	Total CO2/tonne concrete (kg)	75			
		% Relative to OPC	43	% Relative to OPC	47			

Table A2.7. Tabulation of the CESH-cement lifecycle analysis based on 28-day curing.

CESSH Cement - Current Production Scenario

		Process/Factor	Value	Refor notes	CO2 Emissions (kg/tonne cement)	Refor notes	
Cement Production	Define	Concrete Quantity (tonnes)	1	Functional Unit			
		Cement Content (%)	0.14	Assume the same as OPC			
	Raw Materials	CO2 in 1 tonne of cured cement (tonnes)	0.338			1.38	Since only limestone is being mined, this number is adjusted relative to all mining activity in OPC
		Limestone to make 1 tonne cement (tonnes)	0.57	The CaO and Silica do not sum to 1 tonne because CO2 is a significant constituent in cured cement. Assumes Silica fume is 100% SiO2			
		Silica Fume to make 1 tonne cement (tonnes)	0.34				
		Iron Ore to make 1 tonne cement (tonnes)	0				
		Gypsum to make 1 tonne cement (tonnes) - only in final grinding process	0				
	Transportation (kg/tonne cement)	-	-		7	Assume the same as OPC	
	Pyroprocess	Clinker Temperature (C)	1175	Empirical			
		Coal energy for 1 tonne cement heating (GJ)	1.91	Assumed the energy reqs are exactly linear to temperature, compared to OPC. Also scaled due to need for less CaO per tonne cement.	168.7		
		Fuel oil energy for 1 tonne cement (GJ)	0.41		28.4	EIA emission factors (Ref 4)	
		Nat gas energy for 1 tonne cement (GJ)	0.41		20.6		
	Ratio of CO2 emissions to CaCO3	0.44	CaCO3 mass * (44/100) : the ratio of CO2 to CaCO3		250.7	Theoretical based on decomp.	
	Finish Grinding and Blending	Coal energy for 1 tonne cement grinding (GJ)	0.23		20.8		
		Fuel oil energy for 1 tonne cement grinding (GJ)	0.05	Huntzinger and Eatmon 2006	3.5	EIA emission factors	
Nat gas energy for 1 tonne cement grinding (GJ)		0.05		2.5			
Carbon Uptake	Carbon Uptake (% C in cured cement)	9.225	Empirical	-338.3	Based on empirical data		
Concrete Production	Aggregate, mix, and curing	Cement and aggregate transport to Concrete Facility (kg CO2 /m3 concrete)	9.47		3.95		
		Aggregate production (kg/m3 concrete)	3.86	Assume the same as OPC	1.61	Assume the same as OPC	
		Concrete plant operations - mixing and curing (kg/m3 concrete)	14.2		5.92		
Total CO2/tonne cement (kg)		165	Total CO2/tonne concrete (kg)	34			
% Relative to OPC		15	% Relative to OPC	21			